Analytical description of ferroelectric nanostructures and bulk systems with non-collinear magnetic order

Dissertation

zur Erlangung des akademischen Grades

Doctor rerum naturalium (Dr. rer. nat.)

vorgelegt der
Naturwissenschaftlichen Fakultät II - Chemie und Physik
der Martin-Luther-Universität Halle-Wittenberg

von Dipl.-Phys. Thomas Michael
geboren am 01.01.1980 in Merseburg

Tag der Verteidigung: 12.11.2010

Gutachter: Prof. Dr. Steffen Trimper

Prof. Dr. Jamal Berakdar

Prof. Dr. Wolfgang Nolting

Halle (Saale), den 09. Juli 2010

In den Wissenschaften ist viel Gewisses, sobald man sich von den Ausnahmen nicht irremachen läßt und die Probleme zu ehren weiß.

(Goethe)

Contents

List of abbreviations

BTO   barium titanate

STO   strontium titanate

KDP   potassium dihydrogen phosphate

PTO   lead titanate

PLZT lanthanum-doped lead zirconate titanate

BFO   bismuth ferrite

BST   barium strontium titanate

BSCT Ca-doped barium strontium titanate

BZT   barium zirconium titanate

PZT   lead zirconate titanate

SBT   strontium bismuth tantalate

BLSF bismuth layer-structured ferroelectrics

Fe   iron

Sr   strontium

TIM   Ising model in a transverse field

RPA   random phase approximation

MFA   mean-field approximation

DSC   differential scanning calorimetry

XRD   X-ray diffraction

DMI   Dzyaloshinskii-Moriya interaction

ME   magneto-electric

FE   ferroelectric

1. Introduction

Ferroelectricity and ferromagnetism are collective phenomena, involving the mutual interaction of large numbers of particles. In order to be ferroelectric with a switchable spontaneous electric polarization, the material must have a non-centrosymmetric arrangement of the constituent ions and their corresponding electrons, resulting from a balance between short-range and long-range Coulomb interactions. Whereas ferromagnets must have a net angular momentum arising from the alignment of spins of the electrons driven by the quantum-mechanical exchange interaction pointing out the differences in underlying fundamental physics. Beside the quite distinct microscopic properties due to the arrangement of charge for ferroelectrics and electronic spin for ferromagnets, many similarities arise in their behavior. Both classes of materials exhibit hysteresis loops under the application of an external electric or magnetic field. The spontaneous magnetization, as well as the spontaneous polarization decrease with increasing temperature and exhibit a phase transition to a paraelectric or paramagnetic state. Materials with a simultaneous presence of these two primary ferroic properties in the same phase in the sense of Gibbs' phase rule are called multiferroic [1]. Both, ferroelectricity and magnetism, tend to be mutually exclusive and interact weakly with each other when they coexist. More recently, the discovery of a novel class of multiferroics [2], where ferroelectricity is caused by a particular type of magnetic ordering has provided a new and fascinating area to search for magneto-electric materials and appropriate theoretical models.

The description of ferroelectric, magnetic and mutually coupled systems by many-body models and their quantum or classical statistical analysis are aimed at the understanding of macroscopic properties such as the temperature dependent order parameter and the underlying microscopic excitations. In combination, modern tools of statistical mechanics as the thermodynamic Green's function method enable the study of such complex interacting systems of solid state physics. The analytical properties of the Green's function in the complex energy plane account for physical effects characteristic for interacting systems and give access to both static and dynamic properties of condensed matter. This covers the above mentioned macroscopic as well as microscopic quantities, where the Green's function contains all information of the system. Thus, the powerful and unifying formalism found its application in many fields such as magnetism [3], ferroelectrics [4] and multiferroics [5], very recently.

The following chapter (Chapter 2) of this thesis, pertains to a rather general introduction to ferroelectric, magnetic and multiferroic systems and the method of double-time retarded Green's functions, which is applied to several systems discussed in this thesis. Hence, an introduction of this powerful technique is essential to follow the analytical calculations throughout the thesis. Afterwards a many-body Hamiltonian, the Ising model in a transverse field and preliminary investigations of ferroelectric bulk materials in the framework of Green's functions are presented as a basis for the subsequent chapters.

At its discovery, ferroelectricity has been almost attributed as a vagary of nature. The complex structure of the first material (Rochelle salt) [6], that was said to be ferroelectric, hindered to understand the basic mechanisms behind. Hence, ferroelectrics were more of academic interest, of little application and theoretical relevance. The recognition of the relationship between lattice dynamics and ferroelectricity [7], as well as the modeling of ferroelectric phase transitions have intensified the investigations of ferroelectrics.

Stimulated by the progress of a multiscale approach in magnetic materials the dynamics of the Ising model in a transverse field as a basic model for ferroelectric order-disorder phase transitions is reformulated in Chapter 3 in terms of a mesoscopic model and inherent microscopic parameters. The dynamics is governed by a reversible propagating part. Additionally, the life-time of the excitation energy is discussed, where the form of the damping terms is derived under the condition of breaking the time reversal symmetry due to dissipation. The temperature dependence of the excitation energy and its life-time are observed and the model is extended by including an additive noise term, which modifies the excitation spectrum.

The general focus in the field of ferroelectrics changed further, when thin film ferroelectrics were developed and applied in different devices. In confined structures, such as ferroelectric nanoparticles, the interactions are modified with respect to the bulk and it is commonly believed that ferroelectricity is altered and eventually totally suppressed when the system reaches a critical size. Since that time there is a renewed effort in the fabrication, application and theoretical understanding of ferroelectric materials scaled down up to nanometers. The broad variety of experimental activities in the field of ferroelectric nanostructures is accomplished by numerous theoretical studies, which cover the topic on different levels and scales. Chapter 4 of this thesis is devoted to the quantum statistical modeling of the collective behavior in ferroelectric thin films and nanoparticles on the basis of the Ising model in a transverse field. The approach covers the entire regime from the phase transition between the paraelectric and the ferroelectric phase up to the low temperature properties. The Hamiltonian is likewise the starting point to include further degrees of freedom such as impurities and doping. Based on this Hamiltonian, the influence of defects on damping effects in ferroelectric thin films is investigated. The

associated collective phenomena determine the macroscopic behavior of the system. In particular, the size dependence of the polarization, the hysteresis and the dynamics in spherical ferroelectric nanoparticles are discussed. These quantities are also regarded in the presence of defects. The lack of translational invariance in nanoparticles raises the discussion of excitations in real space instead of reciprocal space.

The considerable effort in understanding complex magnetic structures and the experimental detection of complicated magnetic patterns such as in a Mn monolayer on W(110) surfaces [8] and the recently observed asymmetric spin-wave dispersion relation on Fe(110) [9] have initiated the theoretical investigation of non-collinear magnetic structures by an extended Heisenberg model in Chapter 5. The aim of the chapter is to elucidate the relationship between the spin-wave excitation energy and the magnetic alignment of the spins. The progress can be reached by applying a representation of the underlying spin-operators with an arbitrary quantization axis [10]. This approach enables the inclusion of a broad class of spin spiral structures. The Hamiltonian consists of an isotropic Heisenberg coupling, an anisotropic interaction and the Dzyaloshinskii-Moriya interaction (DMI). The spin-wave energy is calculated by the temperature dependent retarded Green's function matrix.

The study of the broad diversity of spin arrangements is strongly raised by the search for new types of order in magneto-electric multiferroics, where both magnetic and ferroelectric order can coexist [11, 12]. Due to a symmetry allowed magneto-electric coupling such multiferroics exhibit the control of magnetic properties by electric fields and, vice versa, a ferroelectric order by magnetic fields. Multiferroics with well separated phase transition temperatures of the underlying ferroelectric and magnetic subsystem are investigated in Chapter 6. Representative examples offering such a behavior are the transition metal perovskite $BiFeO_3$ and hexagonal $RMnO_3$ compounds [13, 14]. Different origins are accounted to ferroelectricity and magnetism in these materials. Therefore, the approach within this chapter is based on a coupled model of the Ising model in a transverse field and an extended Heisenberg model with Dzyaloshinskii-Moriya interaction. The coupling is chosen as biquadratic in terms of the polarization and the magnetic moments. Ordering mechanisms such as the ordering of lone pairs of two outer electrons are characteristic for the occurrence of polarization in this class of materials. Furthermore, it seems reasonable that the coupling between the ferroelectric and the magnetic subsystem is assumed to be weak.

2. Basics

2.1. Ferroelectrics

Dielectric materials are grouped according to the reaction of the polar constituents on an external electric field. This electric field induces a displacement of electrons and ions with respect to the field free position. In case of induced polarization the center of charges coincide, whereas an external electric field shifts of the center of charge and induces a polarization. Contrary, permanent dipoles are aligned along the field lines in case of the orientation polarization. As an important subgroup of dielectric materials ferroelectrics are insulating polar substances of either solid (crystalline or polymeric) or liquid crystals with the appearance of multi-stable degenerated states with a spontaneous macroscopic polarization P_r below a critical temperature T_c. The switching between these states by an electric field, is the characteristic property of ferroelectricity. A comprehensive background of ferroelectric materials can be found in various textbooks [15–19]. The access to the polarized states by the application and variation of an external electric field E reveals a hysteresis curve (Fig. 2.1). In particular, the intrinsic polarization P_r is reversible through the application of an E-field. The coercive field E_c denotes the critical electric field, required to reduce the polarization to zero after the polarization of the sample has been driven to saturation.
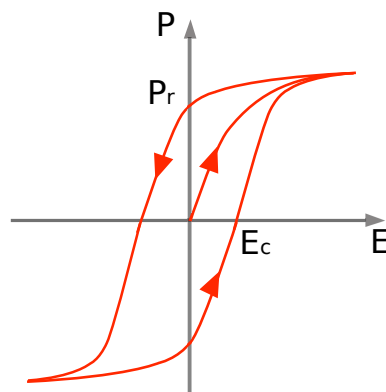

Fig. 2.1.: Schematic hystereses curve of the electric field dependent polarization.

The occurrence of the spontaneous polarization is related to lattice distortions in case of ferroelectric crystals with a polar space group. Many polar crystals with non-

centrosymmetric arrangement of the constituent ions and their corresponding electrons are not ferroelectric, since they can not be switched by external electric fields.

Ferroelectric transitions belong to the wide class of structural phase transitions. Above the phase transition temperature T_c the system is paraelectric (non-polar) and with decreasing temperature it undergoes a first or a second-order phase transition (Fig. 2.2). In case of a first-order transition the polarization, as the order parameter of the system, exhibits a discontinuous change from one to another structural phase. The second-order transition is characterized by a continuous change of the polarization. Both transitions are illustrated for barium titanate (BTO) in Fig. 2.2(a). Most ferroelectric materials reveal a first-order transition near to a second-order one which is characterized by a small jump in the polarization, as well as a drastic increase of the corresponding dielectric permittivity $\varepsilon(T)$ (Fig. 2.2(b)). These transitions are often masked by intrinsic fields, depolarization effects and defects.
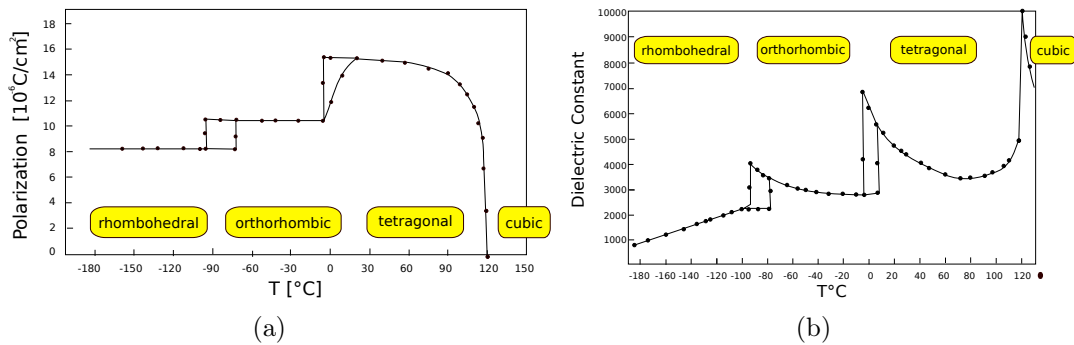

Fig. 2.2.: Temperature dependence of polarization (a) and dielectric constant (b) of BTO; adapted from [20]

The main process in phase transitions in ferroelectrics consists of the reordering of polar groups, usually a few atoms in the unit cell. The positions of all others remain unchanged. Hence, the rest of the crystal lattice is treated as heat bath. Examples are the displacements of the Ti ions with respect to the oxygen octahedra in BTO, the rotations of the oxygen octahedra in strontium titanate (STO) or the rearrangement of the protons in the O–H—O hydrogen bonds in hydrogen bonded ferroelectrics such as potassium dihydrogen phosphate (KDP).

Usually a distinction into displacive and order-disorder ferroelectrics is made. Both labels refer to limiting cases, but are still convenient. This classification is based on a more microscopic picture, than on the previous macroscopic characterization. The search for a microscopical approach can be traced back to the calculations made by Cochran [7] and Anderson [21]. A phase transition in ferroelectrics arises from an instability of a low frequency mode. The schematic drawing in Fig. 2.3 illustrates the factors which influence
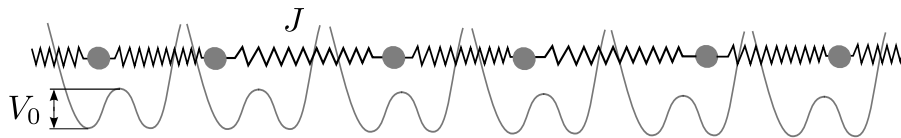
Fig. 2.3.: Simple model for the basic mechanisms of displacive and order-disorder ferroelectrics, adapted from [22, 23].

the nature of the transition. Each atom in the one dimensional model interacts with neighboring atoms by a harmonic force constant J and is influenced by a double-well potential of depth V_0. The two limiting cases can be distinguished referring to the domination of the depth of the potential well or the harmonic force.

The order parameter dynamics of the displacive ferroelectrics ($V_0 \ll J$) are assigned to a phonon-dominated process, which is related to the shift of some atoms or atomic groups within an elementary cell of the corresponding material, see Fig. 2.4. A typical example is lead titanate (PTO) with a crystal structure of perovskite type. Ions are mutually shifted compared to the non-polar, centrosymmetric prototype phase below the phase transition temperature. As a result, the centers of the positive and negative charges are separated and give rise to electric dipole moments. Its average is related to the macroscopic polarization. This polar phase is stabilized by an energy-lowering chemical-bond formation, which is referred as second order Jahn-Teller [24] or pseudo Jahn-Teller effect [25]. Through the Lyddane-Sachs-Teller relation, the divergence of the dielectric susceptibility is connected to the vanishing frequency of a polar phonon.
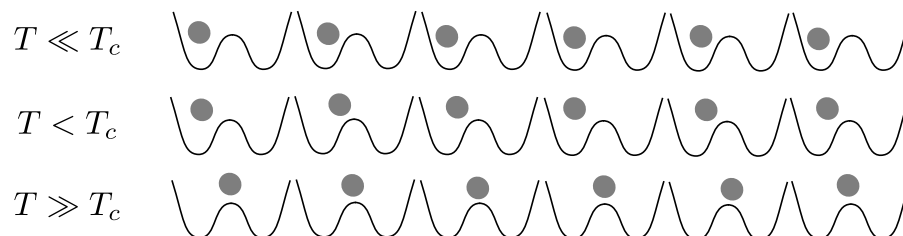
Fig. 2.4.: Ordering sequence in the displacive limit ($V_0 \ll J$).

Order-disorder ferroelectrics ($V_0 \gg J$) exhibit excitations in form of pseudo-spin waves, whereas the order parameter dynamics of displacive ferroelectrics are phonon-like. The harmonic contribution to the potential is negative. The potential $V(Q)$ itself is strongly anharmonic with a maximum at $Q = 0$ making this position unstable (Fig. 2.5). Hence, order-disorder ferroelectrics are characterized by the presence of ions moving in a multiple well. It is the stabilizing effect of the cooperative electrostatic field set up by the ions when displaced into wells all in the same direction, which is responsible for the ferroelectric transition. In these compounds the probability of occupation of each side of the well,

which is equal in the paraelectric state, would become different in the ferroelectric state, as suggested by Slater [26]. Hence, these excitations cannot be described simply as phonons. As the forces are not harmonic the study of the vibration modes turns out to become a more difficult problem. However, this is remarkably simplified in the case of a double-well potential when the separation of the levels inside the well is so large that practically only the ground state doublet can be occupied. If the wells are sufficiently steep, the
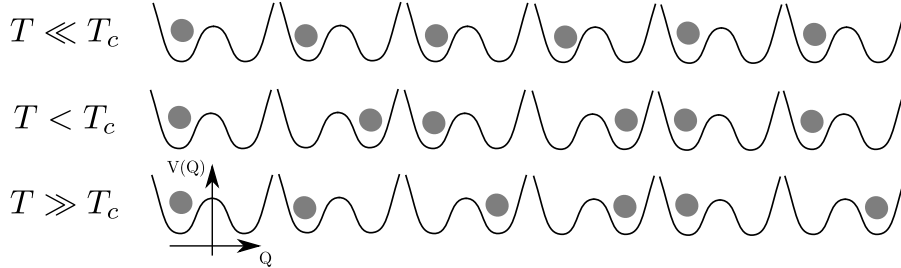

Fig. 2.5.: Ordering sequence in the order-disorder limit $(V_0 \gg J)$.

motion within a given well can be neglected. The ground state in each double-well is degenerated. Higher vibrational states are usually neglected, as the frequency separation between the ground state and the higher vibrational states is much larger than the splitting of the ground state doublet caused by the tunneling through the potential barrier. The prototype of that class is KDP. Each proton in a hydrogen bond can adopt two positions within a double-well potential, which is created by the other ions. Protons are uniformly distributed above the phase transition temperature. In contrast, in the low temperature phase the protons favor a certain position within the double-well, whose structure is evaluated convincingly by ab-initio studies [27, 28] and is supported by neutron diffraction experiments [29]. The averaged number of protons within that well is assumed to be a measure of the spontaneous polarization. Recently, the coupling of the position of the protons to the polarization of the PO_4 groups [30, 31] was shown. In terms of a generalization, one can think of whole groups of atoms or molecules which offer flip-dynamics between two or more equilibrium positions. Lattice distortions should be included in a more refined approach within this class.

However, the ions or protons in the double-well can move from one side to another by tunnel effect [32]. The quantum mechanical tunneling of the proton through the potential barrier between the two wells lifts the degeneracy and significantly influences the dynamics of such systems. Classical theories are therefore unable to explain the isotopic effects observed in KDP and isomorphous ferro- and antiferroelectric compounds with short hydrogen bonds. Through deuteration the Curie point is raised, the increase of the spontaneous polarization with falling temperature becomes much sharper and the value of spontaneous polarization at absolute zero is nearly doubled. Instead of one there

are two bands in the infrared as well as in the Raman spectrum. Moreover, a square well model does not explain the appearance of two OH stretching bands instead of one.

The underlying model is the Ising model in a transverse field (TIM), see Section 2.5. This model is a promising candidate to figure out ferroelectric properties from a microscopic point of view and to apply all the well known quantum statistical techniques used for magnetic materials. Similarly as the magnetic properties are determined by the excitation energy of the spin waves, the macroscopic ferroelectric properties can be derived from the pseudo-spin wave modes in order-disorder ferroelectrics.

Both limiting (displacive/order-disorder) cases are characterized by the occurrence of a soft mode behavior. A low lying elementary excitation with energy $\omega(\vec{q}, T)$ exists, which depends on the wave vector $\vec{q}$ and the temperature T. This mode becomes soft at a particular wave vector $\vec{q}_c$ when the temperature is reaching the critical one:

$$\lim_{T \to T_c} \omega(\vec{q}_c, T) = 0\,. \tag{2.1}$$

This critical wave vector for the ferrodistorsive (including ferroelectric) phase transitions is located in the center of the Brillouin zone $\vec{q}_c = 0$. Antiferrodistorsive systems exhibit a critical wave vector at the boundary of the Brillouin zone $\vec{q}_c = \pi/a$. In ferroelectrics of displacive type such an unstable mode is realized by one normal lattice vibration mode. The nuclei move in slightly anharmonic potentials. In this approach the frequency of the relevant soft phonon decreases on reaching the critical temperature. The restoring force for the mode displacements tends to zero until the phonon has condensed out at the stability limit. The static atomic displacements ongoing from the paraelectric to the ferroelectric phase thus represent the frozen-in mode displacements of the unstable phonon. The order parameter of such a transition is the static component of the eigenvector of the unstable phonon. As the ferroelectric state is characterized by a macroscopic spontaneous polarization, the soft phonon must be both polar and of long wavelength. In order-disorder ferroelectrics the soft collective excitations are rather unstable pseudo-spin waves, than phonons. In terms of limiting cases, all ferroelectric materials, exhibit both kinds of behavior with a material dependent ratio.

2.2. Non-collinear magnetism

Solids are grouped into weak magnetic (paramagnetic, diamagnetic) and strong magnetic (ferromagnetic, antiferromagnetic and ferrimagnetic) materials with respect to their magnetic properties. A characteristic feature of strong magnetic materials is the magnetic order occurring under certain circumstances, which leads to a macroscopic magnetic moment. This moment is of the order of $N\mu_B$ with N atoms and the Bohr magneton μ_B. Typical materials are transition metals with ferromagnetic ordering (iron, cobalt) and transition metal oxides with antiferromagnetic ordering (iron oxide). Ferrimagnetic ordering occurs in complex salts of the transition elements (MnO, Fe_2O_3). Magnetism in solids is originated through electrons of not fully occupied inner shells of atoms, such as iron (3d-shell) or rare earths (4f-shell). The magnetic properties depend on the density distribution of the electrons in unoccupied inner shells and the density of conduction electrons in the crystal lattice. The magnetic moment of a sample results from the magnetic spin moment of the electrons and their orbital angular momentum.
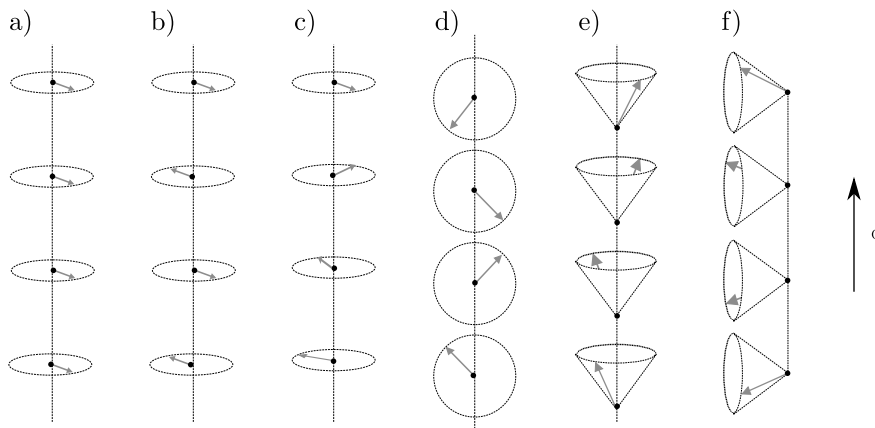
Fig. 2.6.: Types of magnetic ordering a) ferromagnetic b) antiferromagnetic c) screw/ antiferromagnetic spiral d) cycloidal spiral structure e) longitudinal conical/ ferromagnetic spiral f) transverse conical spiral. The propagation direction is indicated by the wave vector Q.

The observed macroscopic magnetic moment is a result of the alignment of the spins by an interaction between the electrons. In the absence of a magnetic field, ferromagnets possess a non-zero spontaneous magnetization (magnetic moment per volume) below a critical temperature. A ferromagnetic order established by magnetostatic dipole interaction would be destroyed by temperatures of the order of one Kelvin. Hence, the stabilization of the parallel orientation of neighboring moments has a quantum-mechanical origin. The spontaneous magnetization is created and stabilized by strong interactions known as exchange interaction [33, 34].

This exchange coupling can be motivated by electrostatic arguments. The Pauli exclusion principle forbids the double occupancy of a quantum state by fermions with the same quantum numbers, which results an antiparallel alignment of two electrons in the same orbital. The electrostatic Coulomb repulsion between electrons is spin independent but larger for two electrons in the same quantum state, than in two different orbitals. Hence, the parallel alignment is favored by coulomb interaction, which competes the antiparallel occupancies of one-electron orbitals.

The theory of localized moments successfully explains many properties of ferromagnetic materials. Here, local magnetic moments exist for the ions at each lattice site in the solid at all temperatures. The corresponding magnetic models enable the understanding of magnetic ordering and have influence to other branches of science, such as quantum mechanics and statistical mechanics. Furthermore, they provide a basis and motivation for several magnetic structures, such as ferromagnetic alignment, cycloids or helical spin structures. Detailed information about magnetism and other theories, such as the band theory, where up- and down-spin bands are unequally occupied by electrons in the low temperature phase, leading to a net magnetic moment, can be found in the literature [10, 35–38].

Mapping electronic quantities such as hopping and Coulomb interaction, onto spin variables yields the Heisenberg Hamiltonian. This model possesses a spontaneous magnetization, which can be reoriented by an external magnetic field. This switching is associated with a hysteresis of the magnetization. The moments align to a ferromagnetic state below the phase transition temperature. The competition between interatomic exchange and thermal disorder decreases the magnetic polarization with increasing temperature. At a well-defined Curie temperature T_c the spontaneous magnetization vanishes with a second-order phase transition to an unpolarized state. Above the Curie temperature the magnetic moments are thermally disordered and there is no net magnetization. The symmetry of the high temperature phase becomes broken when an ordered state arises. Here, the ferromagnetic ordering breaks the time reversal symmetry $(t \rightarrow -t)$, because the magnetization changes sign under time reversal. The Hamiltonian for a magnetic system consists of three parts:

$$H = H_1 + H_2 + H_3 \tag{2.2}$$

$$H_1 = -\frac{1}{2} \sum_{ij} J_{ij} \vec{S}_i \vec{S}_j - g\mu_B \sum_i \left(\vec{H}_i + \vec{H}^A \right) \vec{S}_i \,, \tag{2.3}$$

$$H_2 = -\frac{1}{2} \sum_{ij} \tilde{J}_{ij} S_i^\tau S_j^\tau - \sum_i K_i (\vec{S}_i)^2 \,, \tag{2.4}$$

$$H_3 = -\frac{1}{2} \sum_{ij} \vec{D}_{ij} (\vec{S}_i \times \vec{S}_j) \, . \tag{2.5}$$

The first term H_1 describes the interaction between the magnetic moments at different lattice sites and is invariant under time reversal. In case of a two electron system, the exchange constant J is defined as half of the energy difference between antiparallel and parallel states. A parallel alignment is favored in case of a positive interaction ($J_{ij} > 0$). Otherwise ($J_{ij} < 0$), an antiparallel alignment leading to an antiferromagnetic spin ordering is preferred. The corresponding spontaneous breaking of the symmetry by the ordered state gives rise to Goldstone excitations. They have zero energy and their wavelength diverges. These excitations try to recover the lost symmetry of the system. The magnon with zero wave vector corresponds to the rotation of all spins in the system and costs no energy. The Zeeman term describes the coupling of an external magnetic field $\vec{H}$ to the magnetic moments. The summation includes all atomic spins and the local magnetic field acts on the i-th spin.

Real magnets exhibit no full rotational invariance in spin space. The coupling of magnetism onto the crystal lattice results in a magneto-crystalline anisotropy, which is originated by electrostatic crystal-field interaction and relativistic spin-orbit coupling. Here the magnetic properties depend on the orientation within the crystal. The degenerated order of the spins is partially lifted by spin-orbit-coupling and results in preferred directions within the crystal. Thus, the spontaneous magnetization tends to lie along certain crystallographic axes (easy-axis).

Several kinds of anisotropies H_2, determined by the symmetry group of the magnetic lattice, are known, such as uniaxial, cubic, single-ion or pair anisotropy. A further approximation to uniaxial anisotropy is frequently considered in terms of an effective anisotropy field $\vec{H}^A$. This ansatz is applied in particular for uniaxial antiferromagnets.

Beside single-site uniaxial anisotropies, the exchange interaction could contain an antisymmetric term H_3. Symmetry considerations in magnetic crystals with low symmetry [39] and a microscopic mechanism [40] leads to the so called DMI. Owing to spin-orbit interaction an indirect coupling between spins arises. The Hamiltonian is no longer rotational invariant with an unidirectional anisotropy, which depends on the direction of the spins.

$$J_{ij} = J_{ji} \, , \quad \vec{D}_{ij} = -\vec{D}_{ji} \tag{2.6}$$

Here, $\vec{D}_{ij}$ is the Dzyaloshinskii-Moriya (DM) vector in spin space. The interaction tries to force spins at different sites to be at right angle in a plane perpendicular to the DM vector. So, the spins cant or rotate by a small angle. Collinear uniaxial ferro- or antiferromagnetic

structures become unstable. Instead, directional non-collinear magnetic structures of specific chirality or a small ferromagnetic component of the moments perpendicular to the antiferromagnetic spin orientation (weak ferromagnetism) arise. In spin-$\frac{1}{2}$ systems the DMI seems to be the relativistic leading-order anisotropy term [41] with the role of an effective two-ion easy-plane anisotropy [42] with the easy-plane normal to the vector $\vec{D}_{ij}$.
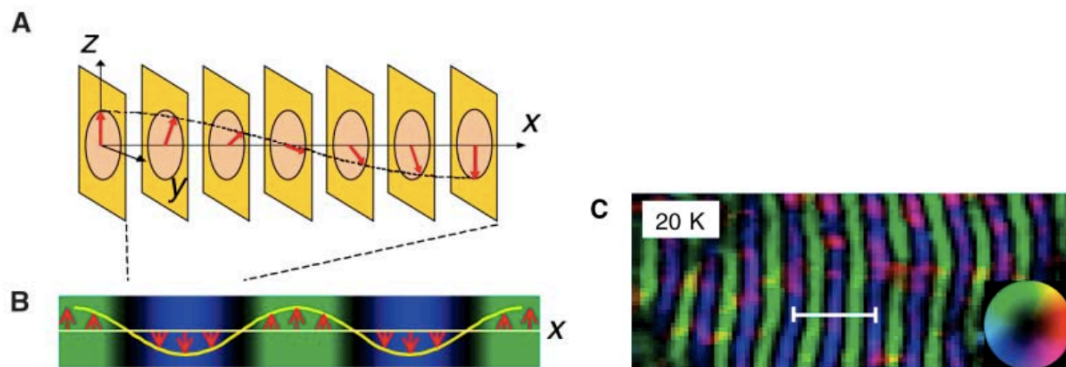

Fig. 2.7.: Illustration of helical spin order. (A) Helical spin order with the helical axis along the x axis in an orthogonal xyz system. Spins are all parallel at a yz plane, and their direction rotates by a constant angle from one plane to a neighboring plane along the helical axis. (B) Magnetization distribution projected on the xy plane for this helical spin order, which changes as a sinusoidal wave. (C) A color representation of magnetization distribution [projected onto the (001) plane] obtained by the transport of intensity equation (TIE) analysis method; the direction and amplitude of the magnetization are represented by changes in color and brightness with respect to the color wheel; all adapted from [43].

Anisotropies and relativistic spin-orbit interactions couple spins to the lattice, which gives rise to complex magnetic structures (Fig. 2.7). Such spiral or screw spin structures gave been found in rare-earth metals, as well as members of the metal silicide family, such as $Fe_{1-x}Co_xSi$. The components of the spins vary periodically along one crystallographic axis.

In these compounds it is appropriate to change to a representation in terms of creation and annihilation operators of the second quantization, such as Pauli-operators b, $b^{\dagger}$, which are defined by their commutator relations:

$$\left[b_i, b_j^{\dagger}\right]_- = \underbrace{\left(1 - 2b_i^{\dagger}b_i\right)}_{2\sigma_i} \delta_{i,j}, \quad \left[b_i, b_j\right]_- = \left[b_i^{\dagger}, b_j^{\dagger}\right]_- = 0, \quad (b_i)^2 = (b_i^{\dagger})^2 = 0. \tag{2.7}$$

An additional transformation [10] of the spin operators into an eigen-representation of the quantization axis $\boldsymbol{\gamma}_f = (\gamma_f^x, \gamma_f^y, \gamma_f^z)$ is adequate. Here, the axis is not fixed and can locally point to an certain direction characterized by the real unit vector $\boldsymbol{\gamma}_f$. The corresponding

transformation of the spin operators for spin-$\frac{1}{2}$ particles with $\sigma_f = \frac{1}{2} - b_f^\dagger b_f$ reads:

$$(S_f)^\alpha = \gamma_f^\alpha \sigma_f + A_f^\alpha b_f + (A_f^*)^\alpha b_f^\dagger . \tag{2.8}$$

The quantization axis has to be chosen in an adequate form, regarding the investigated system. The components of the prefactors A_f^α and $(A_f^*)^\alpha$, preserving the commutator relations, are defined as:

$$A_f^x = -\left(e^{\mathrm{i}\varphi_f} \frac{1 + \gamma_f^z}{4} - e^{-\mathrm{i}\varphi_f} \frac{1 - \gamma_f^z}{4}\right) = -\frac{1}{2}\{\gamma^z \cos\varphi_f + \mathrm{i}\sin\varphi_f\}, \tag{2.9a}$$

$$A_f^y = \mathrm{i}\left(e^{\mathrm{i}\varphi_f} \frac{1 + \gamma_f^z}{4} + e^{-\mathrm{i}\varphi_f} \frac{1 - \gamma_f^z}{4}\right) = -\frac{1}{2}\{\gamma^z \sin\varphi_f - \mathrm{i}\cos\varphi_f\}, \tag{2.9b}$$

$$A_f^z = \frac{1}{2}\sqrt{1 - (\gamma^z)^2} \quad \text{with} \quad \tan\varphi_f = \frac{\gamma_f^y}{\gamma_f^x} . \tag{2.9c}$$

The length of the quantization axis in the $x - y$ plane is defined as $\rho = \sqrt{1 - (\gamma^z)^2}$.

Furthermore, the helical structure can be modified by applying an external field. The angle of the cone is modified until a complete ferromagnetic is achieved at a certain critical field H_c. One theory for magnetic spin spiral structures [44–49] is based on the change of sign and strength of the exchange integral for nearest J_1 and next-nearest neighbors J_2. The minimum of the energy of the ground state corresponds to the maximum of the exchange interaction $J(Q)$

$$E = -NS^2 J(Q) = -NS^2(2J_1 \cos(aQ) + 2J_2 \cos 2aQ) . \tag{2.10}$$

The system will show ferromagnetic or antiferromagnetic ordering, if $J(Q)$ is maximum at $Q = 0$ or π. In case of a minimum of the ground state energy for $0 \leq Q \leq \pi$ the magnetic ordering is of a spiral type with a spiral wave vector being incommensurate with the underlying lattice. Here adjacent spins are rotated by a constant angle. The propagation direction is perpendicular to the plane where the spins are rotating in the proper screw structure. If the plane contains the axis of propagation, the structure is called cycloidal. Anisotropies or applied fields can stabilize both (screw/cycloidal) magnetic structures.

2.3. Multiferroic bulk systems

The combination of electricity and magnetism was discovered by Maxwell in the 19th century. In solids both effects seem to be mutually exclusive due to their different origin, see Section 2.1 and Section 2.2. The real starting point is a short remark by Landau and Lifshitz in 1959. Short time later, the linear magneto-electric effect was theoretically predicted [39, 50] and experimentally observed [51] in Cr_2O_3. The new idea was, not only to have across-coupling of responses, but also systems with two types of ordering, that coexist in the same phase. Magnetism exhibits a spontaneous ordering of spin and orbital magnetic moments whereas ferroelectricity shows a spontaneous ordering of electric dipole moments, even without an external electric or magnetic field. These materials are called multiferroics [1].
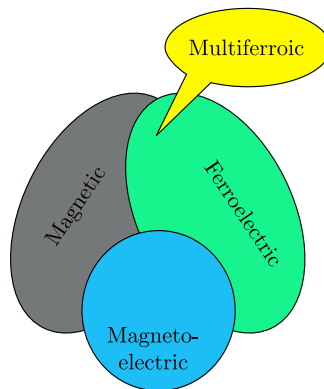

Fig. 2.8.: Schematic grouping of magnetic, ferroelectric and multiferroic systems.

The microscopic origin of magnetism is the presence of localized electrons in partially filled d or f shells. The exchange interaction between the localized moments leads to magnetic ordering, whereas for ferroelectricity the electric charge of electrons and ions and the accompanied relative collective shift of positive and negative ions are responsible. Due to several microscopic sources for ferroelectricity one expects different types of multiferroics. The great enhancement of multiferroic properties in bismuth ferrite (BFO) thin films [52] and the discovery of a new class of multiferroics, where magnetism causes ferroelectricity [2, 53] revived the studies and are reviewed in several papers on the topic of multiferroics [11–14, 54–57].

For the description of multiferroics and the magneto-electric coupling the free energy F is expanded in terms of the electric field E and the magnetic field H:

$$\begin{aligned} F(E, H) =& F_0 + P_i E_i + M_i H_i + \frac{1}{2}\varepsilon_{ij} E_i E_j + \frac{1}{2}\mu_{ij} H_i H_j \\ &+ \alpha_{ij} E_i H_j + \frac{1}{2}\beta_{ijk} E_i H_j H_k + \frac{1}{2}\gamma_{ijk} H_i E_j E_k + \dots \end{aligned} \tag{2.11}$$

with the dielectric permittivity ε_{ij} and the magnetic permeability μ_{ij}. The linear magneto-electric susceptibility tensor α_{ij}, which corresponds to the induction of polarization by a magnetic field or of magnetization by an electric field, is designated to the linear magneto-electric (ME) effect. Therefore, a linear ME effect requires breaking of inversion and time reversal symmetry. Higher order ME effects, β_{ijk} and γ_{ijk} are the bilinear ME susceptibility tensors. The corresponding polarization P_i and the magnetization M_i are obtained by minimizing the free energy.

In general, there are two groups of multiferroics. Type-I multiferroics own different sources for ferroelectricity and magnetism. They appear largely independent with a small coupling between them. Here, ferroelectricity appears up to higher temperatures than magnetism and the polarization is relatively large. In the second group, type-II multiferroics, the magnetic ordering causes ferroelectricity with a polarization smaller compared to type-I multiferroics.

2.3.1. Type-I multiferroics

One of the most studied multiferroics is BFO [58, 59], where ferroelectricity is due to lone pairs. It shows a long range modulated antiferromagnetic spin configuration and ferroelectricity at room temperature. Bismuth ferrite belongs to type-I multiferroics, where a large separation between the magnetic [60] ($T_N = 640\,\text{K}$) and the ferroelectric transition [61] ($T_c = 1100\,\text{K}$) is observed. The ferroelectricity reduces the symmetry from cubic to a rhombohedral distorted perovskite structure with space group R3c [62, 63]. Cations are displaced along the [111] direction relative to the anions and the oxygen octahedra rotate with alternating sense around the [111] axis. The polarization pointing in [111] direction of the perovskite structure has eight possible orientations along the four cube diagonals. The Bi^{3+} ion plays the major role for ferroelectricity. Here stereochemically active lone pairs, or dangling bonds, are formed by two outer $6s$ electrons, which do not participate in the chemical bonds and move away from the centrosymmetric positions in their oxygen surrounding. They possess a high polarizability and order with a certain orbital mixture of p orbitals in one direction. These lone pairs cause a displacement of the bismuth and oxygen ions along the [111] direction [64].

The domains can be switched of the direction by 180°, 109°, 71°. The switching of 109° and 71° changes the rhombohedral axis. This leads to a change of the ferroelastic domain state. The iron (Fe) moments show an antiferromagnetic ordering between adjacent planes of G-type, i.e an antiparallel alignment relative to each other in all three directions and are ferromagnetically aligned in the (111) pseudo-cubic planes. In bulk the antiferromagnetic vector follows a long wavelength spiral with an incommensurate wavelength [65]. This leads to a cancelation of the macroscopic magnetization and inhibits

the linear ME effect. A suppression of the spin spiral can be achieved by doping [66], the application of high magnetic fields [67] or in case of reduced dimensionality, e.g. thin films [68].

Ferroelectricity due to charge ordering [12] is in particular observed in transition metals with ions of different valencies. The localization of charge carriers at low temperatures forms periodic superstructures. A non-symmetric ordering can induce ferroelectricity. In particular, in case of an inequivalence of sites and bonds after charge ordering. This can originate from the existence of ions with different charge and the dimerization or inequivalent bonds due to the structure of the material and a site-centered charge on top.

Geometric ferroelectricity can be found in hexagonal manganites $RMnO_3$ (R=Ho-Lu,Y) [69] showing a lattice transition with an enlarged unit cell, where a non-linear coupling to a non-polar lattice distortion induces an electric dipole moment. The origin of ferroelectricity is the tilting of the rigid MnO_5 block in $YMnO_3$, which provides a closer packing. Subsequently, the oxygen ions move closer to the yttrium ions.

2.3.2. Type-II multiferroics

In magnetic multiferroics ferroelectricity exists only in a particular magnetically ordered state. Complex magnetic structures and phase diagrams are observed in frustrated magnets. The spiral magnetic ordering breaks inversion symmetry, being a necessary condition for the existence of electric polarization. Competing interactions between the spins preclude a simple magnetic ordering, so that a sequence of magnetic transitions can be found. In $TbMnO_3$ the magnetic ordering appears at $T_{N_1} = 41 \, \text{K}$ with a sinusoidal spin-density wave. All spins are pointing in one direction but the size of the local moments varies periodically in space. This lead to a sort of antiferromagnetic phase with zero total moment. The change to another spin structure occurs around $T_{N_2} = 28 \, \text{K}$, where spins form a cycloid. Only in the low temperature phase a non-zero electric polarization appears. Symmetry considerations to the polarization and the magnetization, the two order parameters, with respect to an inversion of all coordinates $\vec{r} \rightarrow -\vec{r}$ and time reversal $t \rightarrow -t$ yield the allowed form of the magnetically induced electric polarization $\vec{P}$, if the magnetic ordering $\vec{M}$ is inhomogeneous:

$$\vec{P} \propto \left[(\vec{M} \cdot \partial)\vec{M} - \vec{M}(\partial \cdot \vec{M}) \right]. \tag{2.12}$$

The spatial variation of magnetization is induced by competing interactions, which often leads to an incommensurate magnetic state. A microscopic [5] and a phenomenological

approach [70] showed, that a cycloidal spiral generates a polarization in the form:

$$\vec{P} \propto \vec{r}_{ij} \times [\vec{S}_i \times \vec{S}_j] \propto [\vec{Q} \times \vec{e}]\,. \tag{2.13}$$

Here $\vec{r}_{ij}$ is connecting neighboring spins, the wave vector $\vec{Q}$ describes the spiral and $\vec{e}$ is the spin rotation axis. The microscopic mechanism for induced ferroelectricity in spiral magnets involves the inverse effect of the DMI, presented in Section 2.2,

$$\lambda \sum_l (\vec{u}_l \times \vec{e})(\vec{S}_l \times \vec{S}_{l+1}) \tag{2.14}$$

which favors non-collinear spin ordering. The strength of the relativistic correction to the usual superexchange is proportional to the spin-orbit coupling constant. Here a lattice relaxation occurs in a magnetic ordered state, which is named as inverse DM-effect. An illustrative example is the mediation of the exchange between spins often by oxygen ions, to form bonds between pairs of transition metals. The DM vector $\vec{D}$ is proportional to $\vec{u} \times \vec{e}$, where $\vec{u}$ is the shift from the connecting vector between magnetic ions. In the spiral state, the vector product has the same sign for all pairs of neighboring spins. Hence, all oxygen ions are pushed in the same direction and induce an electric polarization.

Another approach describes type-II multiferroics with collinear magnetic structures such as Ising chain magnets ($Ca_3CoMn_2O_6$) [71] or the high temperature ferroelectric phase of rare earth metal oxids (RMn_2O_5) [72, 73], where no spin-orbit interaction is involved. Magnetic moments are aligned along a particular axis and the polarization is a consequence of exchange striction. A simple example is the frustrated spin chain with a competition between ferromagnetic nearest-neighbor interaction and antiferromagnetic next-nearest-neighbor interaction. Exchange striction associated with symmetric superexchange leads to a bond stretching and shortening between different spin alignments. Thus, the possible alternation of charges of magnetic ions along the chain breaks the inversion symmetry and induces a polarization.

2.4. The Green's function method

In many-particle physics, especially solid state physics, Green's functions are connected to a variety of measurable quantities, such as thermodynamic expectation values $\langle A \rangle$, $\langle B \rangle$ or correlation functions of the type $\langle AB \rangle$ of the observables A, B. One of the main advantages of the Green's functions method is the ability to calculate these observables in a certain approximation without knowledge of the wave functions [74]. Equilibrium quantities such as thermodynamic potentials (internal energy), particle densities, magnetization, polarization and the energy of the elementary excitations are determined by the corresponding Green's functions. Response functions such as the electric and magnetic susceptibility, electric conductivity, transition probabilities and cross sections are directly related to the Green's functions. The evolution in time of the quantum mechanical operators can be reduced to a set of coupled equations — the equations of motion — of complex functions with the help of Green's functions. Several possible definitions of Green's functions and more detailed derivations are given in the literature [10, 36, 75–80].

The connection between Green's functions and the reaction of a physical system to an external perturbation is given in a quite general formalism, known as linear response theory or Kubo formula [81]. The response of measurable quantities on an external perturbation can be related directly to the Green's functions with a physical meaning or as an auxiliary quantity for the calculation of relevant correlation functions.

The investigated system is described by the Hamilton operator of the following form:

$$H = H_0 + W_t \tag{2.15}$$

An interacting particle system without an external field is described by H_0. An external time dependent perturbation has the form:

$$W_t = -\sum_j A_j F_j(t) \quad \text{with} \quad \lim_{t \to -\infty} W_t = 0 \,. \tag{2.16}$$

The scalar time dependent field $F(t)$, a c-number, couples to the observable represented by a set of operators A_j of the quantum mechanical system. The external perturbation is switched off for $t \to -\infty$. Hence the system is in the thermodynamic equilibrium at this time and can be described by the statistical operator

$$\lim_{t \to -\infty} \rho_t = \rho_0 = \frac{e^{-\beta \mathcal{H}_0}}{Tr(e^{-\beta \mathcal{H}_0})} = \frac{1}{\Xi_0} e^{-\beta(H_0 - \mu N)} \quad \text{with} \quad \beta = \frac{1}{k_b T} \,. \tag{2.17}$$

The averaging is carried out in the grand canonical ensemble with the chemical potential

μ and the operator of the total number of particles N. In the unpertubated case, the time evolution is described by the time independent Hamilton operator H_0. The observable is not explicitly time dependent and the associated thermodynamic expectation value $\langle A \rangle$ is a measurable quantity. In a pure ensemble it reads:

$$\langle A \rangle = Tr(\rho A) = (\Psi, A\Psi) = \int\int dx dx' \Psi^* A \Psi \quad \text{with} \quad \rho(x, x') = \Psi(x)\Psi^*(x'). \quad (2.18)$$

The system is described by one wave function Ψ. The statistical operator ρ of a set of variables x is also called density matrix or density operator.

In case that the wave functions $\Psi_1, \Psi_2, \ldots$ are realized with the probability $w_1, w_2, \ldots$ the ensemble is mixed. The positive probabilities have to fulfill $\sum_i w_i = 1$ and

$$\langle A \rangle = Tr(\rho A) = \frac{1}{\Xi}Tr(e^{-\beta\mathcal{H}}A) = \sum_i w_i(\Psi_i, A\Psi_i) = \sum_i w_i \int\int dx dx' \Psi_i^* A\Psi_i. \quad (2.19)$$

The statistical operator is modified and the time evolution is determined by the time dependence of the wave functions.

$$\rho(x, x', t) = \sum_i w_i \Psi_i(x, t)\Psi_i^*(x', t) \quad (2.20)$$

The doubled probability character of quantum statistics is evident. First the quantum mechanical average given in Eq. (2.19) and second the consideration of a statistical ensemble.

In the presence of the external perturbation W_t a measure of the response of the system to the perturbation is the change $\Delta A_t = \langle A \rangle_t - \langle A \rangle_0$. The observables has to be calculated with the trace of the statistical operator ρ_t and A_i.

$$\langle A_i \rangle_t = Tr(\rho_t A_i) \quad (2.21)$$

For the calculation of the density matrix ρ_t it is appropriate to switch to the Dirac picture with

$$\rho_t(t) = e^{\frac{i\mathcal{H}_0 t}{\hbar}} \rho_t e^{-\frac{i\mathcal{H}_0 t}{\hbar}}. \quad (2.22)$$

The lower index denotes the explicit time dependence caused by the field and the argument the dynamic time dependence. Within the Dirac pictures, the equation of motion of the statistical operator is solely determined by the perturbation. The integration with the initial condition $\lim_{t\to-\infty} \rho_t(t) = \rho_0$ could be solved iteratively. While the perturbation of

the system is assumed to be small the consideration of the first order $\rho_t^{(0)} = \rho$ is sufficient and is termed as linear response. The invariance of a product of operators for cyclic permutation of the operators yields the time dependence of the averaged value

$$
\begin{aligned}
\langle A_i \rangle_t &= \langle A_i \rangle_0 + \frac{1}{i\hbar} \int\limits_{-\infty}^{t} \left\langle \left[A_i, W_{t'}(t') \right]_- \right\rangle dt' \\
&= \langle A_i \rangle_0 - \sum_j \int\limits_{-\infty}^{\infty} \langle\langle A_i(t);\ A_j(t') \rangle\rangle F_j(t') dt' \ .
\end{aligned}
\tag{2.23}
$$

Here a completely general formulation of the physics of the measurement of the quantity $\langle A_i \rangle_t$, e.g. a transport coefficient, is given. This is often referred to as the Kubo formula and is the analog in non-equilibrium statistical mechanics of the Gibbs formula in equilibrium statistical mechanics. In this way, the calculation of a non-equilibrium quantity is reduced to the mathematical problem of evaluating a response function. The function defined in Eq. (2.23) is called two-time retarded Green's function. This expression was introduced in the field of quantum statistics [75]. The term "retarded" points out only perturbations at times $t' < t$ contribute to the mean values of A_i due to the nature of the Θ-function. This Green's function contains only quantities of the unperturbated system and defines the generalized susceptibility.

$$
\langle\langle A_i(t);\ A_j(t') \rangle\rangle = -\frac{i}{\hbar} \Theta(t - t') \left[A_i(t), A_j(t') \right]_- = -\chi_{ij}
\tag{2.24}
$$

Both depend only on the difference between time t and t' due to the invariance of the trace with cyclic permutation.

2.4.1. Equation-of-motion method

The time dependence of the retarded Green's function arising in the Kubo theory enables to write down differential equations, which are fulfilled by this function. Aside the retarded Green's function, the advanced and the causal one arise. They have different boundary conditions. It is necessary to introduce these functions due to their important properties in the complex plane. The fundamental spectral theorem will justify the introduction of these three types of Green's functions. The retarded Green's functions

$$
G_{AB}^{(r)}(t - t') =: \langle\langle A(t); B(t') \rangle\rangle =: -\frac{i}{\hbar} \Theta(t - t') \left\langle \left[A(t), B(t') \right]_\eta \right\rangle ,
\tag{2.25}
$$

the advanced Green's functions

$$G_{AB}^{(a)}(t - t') =: \langle\langle A(t); B(t')\rangle\rangle^a =: +\frac{i}{\hbar}\Theta(t' - t)\left\langle\left[A(t), B(t')\right]_\eta\right\rangle , \qquad (2.26)$$

and the causal one

$$G_{AB}^{(c)}(t - t') =: \langle\langle A(t); B(t')\rangle\rangle^c =: -\frac{i}{\hbar}\left\langle T_\eta\left[A(t), B(t')\right]_\eta\right\rangle . \qquad (2.27)$$

The temperature dependence enters through the thermal averaging (Eq. (2.19)) and the time dependence of the operators $A(t)$ and $B(t')$ is given in the Heisenberg picture.

$$A(t) = e^{\frac{i}{\hbar}\mathcal{H}_0 t}Ae^{-\frac{i}{\hbar}\mathcal{H}_0 t} \qquad (2.28)$$

The dedicated equation of motion reads:

$$i\hbar\frac{\partial}{\partial t}A(t) = \left[A(t), \mathcal{H}_0\right]_- \qquad (2.29)$$

The choice of commutator or anticommutator within the Green's functions is based on the convenience of the regarded system.

$$[A, B]_\eta = AB - \eta BA \qquad (2.30)$$

The expectation value is defined with the grand canonical ensemble $\mathcal{H} = H - \mu N$, see Eq. (2.19). A further important quantity is the spectral density.

$$S_{AB}(t, t') = \frac{1}{2\pi}\left\langle [A(t), B(t')]_\eta\right\rangle \qquad (2.31)$$

The Hamilton operator $\mathcal{H}$ is not explicitly time dependent. Hence, the correlation functions $\langle A(t)B(t')\rangle$ as well as the Green's functions and the spectral density are homogeneous in time

$$\langle A(t)B(t')\rangle = \langle A(t - t')B(0)\rangle . \qquad (2.32)$$

The Green's functions are determined by their equation of motion.

$$i\hbar\frac{\partial}{\partial t}G_{AB}^{(\alpha)}(t - t') = \delta(t - t')\left\langle [A(t), B(t')]_\eta\right\rangle + \langle\langle [A(t), \mathcal{H}]_-; B(t')\rangle\rangle^{(\alpha)} \qquad (2.33)$$

The difference originates from the boundary conditions. The energy representation by Fourier transformation is carried out by:

$$G_{AB}^{(\alpha)}(\omega) = \int_{-\infty}^{\infty} e^{+i\omega(t-t')} G_{AB}^{(\alpha)}(t-t') d(t-t') \tag{2.34}$$

$$G_{AB}^{(\alpha)}(t-t') = \frac{1}{2\pi} \int_{-\infty}^{\infty} e^{-i\omega(t-t')} G_{AB}^{(\alpha)}(\omega) d\omega \tag{2.35}$$

Using this transformation, Eq. (2.33) is an exact equation of motion in an algebraic form.

$$\hbar\omega G_{AB}^{(\alpha)}(\omega) = \left\langle [A, B]_\eta \right\rangle + \left\langle\left\langle [A, H]_-; B \right\rangle\right\rangle_\omega^{(\alpha)} \tag{2.36}$$

The higher Green's function on the right hand side satisfies its own equation of motion still including a higher Green's function. This results in an infinite hierarchy of equations and has to be decoupled physically meaningful. Through the appropriate decoupling the Green's functions of higher order are approximated by a linear combination of Green's function of lower order and the system of equations is closed.

2.4.2. The spectral theorem and spectral representation

Green's functions and thermodynamic correlations, such as $\langle A(t)B(t')\rangle$, are related by the spectral theorem. The whole macroscopic thermodynamics can be determined using adequate defined Green's functions and spectral densities by this fundamental theorem:

$$\langle B(t')A(t) \rangle = \frac{1}{2\pi} \int_{-\infty}^{\infty} e^{-i\omega(t-t')} J_{BA}(\omega) d\omega \tag{2.37}$$

$$= \lim_{\delta \to 0^+} \frac{i\hbar}{2\pi} \int_{-\infty}^{\infty} e^{-i\omega(t-t')} \frac{G(\omega + i\delta) - G(\omega - i\delta)}{e^{\beta\hbar\omega} - \eta} d\omega + \frac{1+\eta}{4\pi\hbar} C_{BA}. \tag{2.38}$$

The relation of the spectral representation of the spectral density function and the Green's function is shown by considering correlation functions $\langle A(t)B(t')\rangle$ and $\langle B(t')A(t)\rangle$.

Starting with the eigenstates $|E_n\rangle$ with eigenenergies E_n, which form a complete and orthonormal system

$$\mathcal{H}|E_n\rangle = E_n|E_n\rangle \text{ with } \langle E_n|E_m\rangle = \delta_{n,m} \text{ and } \sum_n |E_n\rangle\langle E_n| = 1, \tag{2.39}$$

the expectation value $\langle A(t)B(t')\rangle$ can be rewritten in the following form:

$$\langle A(t)B(t')\rangle = \frac{1}{\Xi}Tr(e^{-\beta\mathcal{H}}A(t)B(t')) \tag{2.40}$$

$$= \frac{1}{\Xi}\sum_n \langle E_n|\, e^{-\beta\mathcal{H}}A(t)B(t')\,|E_n\rangle \tag{2.41}$$

$$= \frac{1}{\Xi}\sum_{n,m} \langle E_n|\, B\,|E_m\rangle \langle E_m|\, A\,|E_n\rangle\, e^{-\beta E_n}e^{\beta(E_n-E_m)}e^{-\frac{i}{\hbar}(E_n-E_m)(t-t')} \tag{2.42}$$

In the same way $\langle B(t')A(t)\rangle$ is

$$\langle B(t')A(t)\rangle = \frac{1}{\Xi}Tr(e^{-\beta\mathcal{H}}B(t')A(t)) \tag{2.43}$$

$$= \frac{1}{\Xi}\sum_{n,m} \langle E_n|\, B\,|E_m\rangle \langle E_m|\, A\,|E_n\rangle\, e^{-\beta E_n}e^{-\frac{i}{\hbar}(E_n-E_m)(t-t')} \tag{2.44}$$

The Fourier transformation of both correlation functions reads:

$$\langle A(t)B(t')\rangle = \frac{1}{2\pi}\int_{-\infty}^{\infty} J_{BA}(\omega)e^{\hbar\beta\omega}e^{-i\omega(t-t')}d\omega \tag{2.45}$$

$$\langle B(t')A(t)\rangle = \frac{1}{2\pi}\int_{-\infty}^{\infty} J_{BA}(\omega)e^{-i\omega(t-t')}d\omega \tag{2.46}$$

Here, the spectral density function $J_{BA}(\omega)$ in spectral representation [78] is associated with the time correlation function $\langle A(t)B(t')\rangle$.

$$J_{BA}(\omega) = \frac{2\pi\hbar}{\Xi}\sum_{n,m} \langle E_n|\, B\,|E_m\rangle \langle E_m|\, A\,|E_n\rangle\, e^{-\beta E_n}\delta(E_n-E_m-\hbar\omega) \tag{2.47}$$

An important relation between the two spectral functions is $J_{BA}(\omega) = e^{-\hbar\beta\omega}J_{AB}(-\omega)$.

In a next step the commutator and anticommutator are calculated.

$$\langle [A(t-t'),B]_-\rangle = \frac{1}{\Xi}\sum_{n,m} \langle E_n|\, B\,|E_m\rangle \langle E_m|\, A\,|E_n\rangle\, (e^{-\beta E_m}-e^{-\beta E_n})e^{-\frac{i}{\hbar}(E_n-E_m)(t-t')} \tag{2.48}$$

$$= \frac{1}{2\pi}\int_{-\infty}^{\infty} e^{-i\omega(t-t')}J'_{BA}(\omega)(e^{\hbar\beta\omega}-1)d\omega \tag{2.49}$$

$$\langle [A(t-t'),B]_+\rangle = \frac{1}{2\pi}\int_{-\infty}^{\infty} e^{-i\omega(t-t')}J_{BA}(\omega)(e^{\hbar\beta\omega}+1)d\omega \tag{2.50}$$

In J'_{BA} the condition $E_n \neq E_m$ is made. Now it is possible to express the Green's functions in the Lehmann representation. With the help of the Fourier transformation of

the Heavyside function,

$$-\mathrm{i} \int_{-\infty}^{\infty} e^{\mathrm{i}(\omega-\bar{\omega})(t-t')} \Theta(t-t') d(t-t') = \lim_{\delta\to 0^+} \frac{1}{\omega - \bar{\omega} + \mathrm{i}\delta} \,, \tag{2.51}$$

the spectral representation for the retarded and the advanced Green's function reads:

$$G_{AB}^{(r)} = \lim_{\delta\to 0^+} \frac{1}{2\pi\hbar} \int_{-\infty}^{\infty} J_{BA}^{\eta}(\bar{\omega}) \frac{e^{\hbar\beta\bar{\omega}} - \eta}{\omega - \bar{\omega} + \mathrm{i}\delta} d\bar{\omega} \tag{2.52}$$

$$G_{AB}^{(a)} = \lim_{\delta\to 0^+} \frac{1}{2\pi\hbar} \int_{-\infty}^{\infty} J_{BA}^{\eta}(\bar{\omega}) \frac{e^{\hbar\beta\bar{\omega}} - \eta}{\omega - \bar{\omega} - \mathrm{i}\delta} d\bar{\omega} \tag{2.53}$$

with

$$J_{BA}^{\eta}(\omega) = \begin{cases} J_{BA}'(\omega) & \text{for} \quad \eta = +1 \\ J_{BA}(\omega) & \text{for} \quad \eta = -1 \,. \end{cases} \tag{2.54}$$

Due to the opposite sign in the denominator of the integral, the retarded and advanced functions have poles in the lower and upper half-planes, respectively. Hence they can be analytically continued in different complex half-planes. Via the spectral density function, the Green's functions have simple poles at the excitation energies of the interacting system. The variable ω can be seen as complex. Hence, there is a united expression. For $\mathrm{Im}\,\omega > 0$ it is the retarded Green's function, for $\mathrm{Im}\,\omega < 0$ it is the advanced one.

$$G_{AB}(\omega) = \langle\langle A; B \rangle\rangle = \frac{1}{2\pi\hbar} \int_{-\infty}^{\infty} J_{BA}^{\eta}(\bar{\omega}) \frac{e^{\hbar\beta\bar{\omega}} - \eta}{\omega - \bar{\omega}} d\bar{\omega} = \begin{cases} G_{AB}^{(r)}(\omega) & \text{for} \quad \mathrm{Im}\,\omega > 0 \\ G_{AB}^{(a)}(\omega) & \text{for} \quad \mathrm{Im}\,\omega < 0 \end{cases} \tag{2.55}$$

With the Dirac identity, the difference between the retarded and advanced Green's function yields an expression for the spectral function.

$$J_{BA}(\omega) = \lim_{\delta\to 0^+} \mathrm{i}\hbar \frac{G(\omega + \mathrm{i}\delta) - G(\omega - \mathrm{i}\delta)}{e^{\beta\hbar\omega} - \eta} + \frac{1}{2}(1+\eta) C_{BA} \delta(\hbar\omega) \tag{2.56}$$

with

$$C_{BA} = \lim_{\omega\to 0} \pi\hbar^2 \omega \langle\langle A; B \rangle\rangle^{\eta=-1} \tag{2.57}$$

With this expression the fundamental spectral theorem Eq. (2.38) allows to calculate correlation functions with the help of the Green's functions.

2.5. Microscopical description of ferroelectric materials - The Ising model in a transverse field

Many-particle approaches using quantum statistics cover the entire regime from the phase transition between the paraelectric and the ferroelectric phase up to the low temperature properties. The starting point is an appropriate Hamilton operator which includes the relevant degrees of freedom. Based on this Hamiltonian the elementary excitations and their damping can be calculated. These collective phenomena determine the macroscopic behavior of the system such as the order-parameter, the susceptibility, the dielectric function and other quantities.

Originally the Ising model in a transverse field had been proposed by Blinc and Žekš [19, 82] and de Gennes [83] for the description of ferroelectrics of the KDP-type. In this hydrogen bonded ferroelectrics a transverse field represents the proton tunneling between the two equilibrium positions of the protons within the O–H—O bonds. The approximative applicability of the TIM to ferroelectrics of perovskite structure such as BTO [84, 85] has been demonstrated. Following the rules of the order-disorder model, the paraelectric phase in BTO is associated with the position of the Ti ions. Instead of occupying the body center positions as in an ideal cubic perovskite structure, the Ti ions are randomly displaced off the center of symmetry along the cube diagonals [86], due to a pseudo Jahn-Teller effect [87]. This causes the appearance of the disordered phase.

Therefore the TIM seems to be a rather universal model which allows a microscopical description of ferroelectrics including thin films and nanoparticles, at least approximatively for a broad class of ferroelectric materials. A further application of the Ising model in a transverse field in solid state physics is a magnetic system with a singlet crystal field ground state [88], where the tunneling field plays the role of the crystal field.

The TIM assumes the existence of polar groups with two alignments, such as a proton in one minimum of a double-well potential. The tunneling between these two states lifts the degeneracy and the dynamics of the systems is significantly influenced (Fig. 2.9). The corresponding operators of such a two-level particle system can be expressed in terms of spin-$\frac{1}{2}$ Pauli matrices. Advantages are the analogy to magnetic systems, which are well advanced and the avoidance of the complicated mathematics for anharmonic phonon treatment.

The ordering of functional groups is assigned to the two eigenvalues of the z-component of a spin operator. The description in terms of spins is given in a form analogous to permanent dipole behavior and is called pseudo-spin description. Mapping the relevant mechanism onto a virtual spin operator is one of the key ideas for this model. Both eigenvalues of $S^z = \pm 1/2$ represent the two allowed positions. In so far the spin components
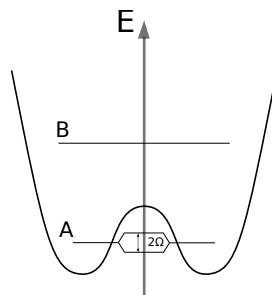
Fig. 2.9.: Energy of the ground state A and first excited state B in the double-well potential. The ground state is split by the tunneling effect.

play the role of 'dipolar' coordinates. The entire system is arranged on a lattice, so the two possible orientations of the microscopic coordinate dipole moment operator S_i^z are used as the dynamical variable. The crystals energy is determined by the method of distribution of particles over equilibrium positions. There is only one disordered particle in each unit cell of the crystal and the disorder is characteristic for the motion along a single direction.

In real space the Hamilton operator of the Ising model in a transverse field [19, 82, 83, 89]:

$$H = -\frac{1}{2}\sum_{ij} J_{ij} S_i^z S_j^z - 2\Omega \sum_i S_i^x - 2\mu E \sum_i S_i^z \,, \tag{2.58}$$

consists of an Ising-like coupling, which is influenced by a tunneling term. The z-component of a spin-$\frac{1}{2}$ operator S_i^z at a certain lattice site i interact via the interaction parameter $J_{ij} \equiv J(r_i - r_j)$, which describes the coupling of two pseudo-spins, equivalent to the interaction of functional groups at different sites. In other words two particles, each in a strong anharmonic double-well potentials, are coupled by the strength J_{ij}. It has to be noted that the interaction strength depends on the distance between the pseudo-spins. Consequently the interaction strength is determined by the lattice parameters, the lattice symmetry and the number of nearest neighbors. The sum is performed over all lattice points of the regarded system. As pointed out by [19] one should take into account a tunneling between the two positions signalized by the eigenvalues of S^z. The tunneling frequency between the two wells is Ω. The x-component of the spin operator S^x — the tunneling operator — symbolizes the operation of a proton jump into the other well of the bond. The tunneling proton has a split ground state with a separation of 2Ω and higher levels are ignored, if the wells are not too deep. Corresponding excitations across 2Ω are wave vector independent only, if there is no proton-proton interaction. The tunneling through the potential barrier influences the form of the potential relief and the

mass of the particles. This effect competes with the process of random jumps associated with thermal fluctuations of the energy. The tunneling implies an overlap of the wave functions of the right- and left-hand states and a change in the probability of the particle being at one of the positions. The external electric field E influences the system by a linear coupling to the dipole moment. The expectation value $\langle S^z \rangle$ measures the difference between the occupation of the left and right equilibrium site and the difference in the occupation between the symmetric and antisymmetric energy state is given by $\langle S^x \rangle$.

The determination of the interaction energy and the strength of the tunneling integral are beyond the scope of the presented theory. Hence, these energies have to be included from experimental results or ab-initio calculations [90].

The Hamiltonian in Eq. (2.58) describes systems undergoing a second-order phase transition. Taking into account four-spin interactions, it can be applied to first-order phase transitions [91, 92]. For $J_{ij} < 0$ the maximum of $J_\mathbf{q}$ occurs at a non-zero point in the Brillouin zone, for example at the zone boundary. The mode gets soft for a finite $\mathbf{q}_0$ and the order parameter is not macroscopic. The frozen-in normal coordinate of the soft mode has a periodicity of $\mathbf{q}_0$. The low temperature phase is antiferroelectric, the unit cell is doubled and the order parameter is the sublattice polarization.

2.6. Microscopical description of ferroelectric bulk materials

The TIM had been extensively studied with different methods [93–95]. Properties of the Hamiltonian have only been obtained exactly in the one dimensional case [96–98], otherwise various approximations must be made. This system shows a phase transition, somewhat different from the pure Ising case [94]. The molecular field treatment gives a straightforward account of the transitions with explicit expressions for T_c, $\langle S^z \rangle$ and $\langle S^x \rangle$ as a function of J and Ω [83]. Starting from (2.58) one finds immediately that the ordered phase is characterized by $\langle S^x \rangle \neq 0$ and $\langle S^z \rangle \neq 0$, whereas in the disordered phase one finds $\langle S^z \rangle = 0$. The ordering arises because of the interactions J, and is impeded by the transverse field Ω. The molecular field forms a vector $\vec{h}_i^{eff} = (2\Omega, 0, \sum_j J_{ij} \langle S_j^z \rangle)$ in pseudo-spin space pointing along a general direction in the $x - z$ plane.

$$
\begin{aligned}
|h^{eff}| &= \frac{J(0)}{2} \tanh(\frac{\beta|h^{eff}|}{2}), \quad \langle S^x \rangle = \frac{2\Omega}{J(0)} \quad \text{for} \quad T < T_c \\
\langle S^x \rangle &= \frac{1}{2} \tanh(\frac{\beta 2\Omega}{2}) \quad \text{for} \quad T > T_c
\end{aligned}
\tag{2.59}
$$

Thus as Ω increases from zero, T_c decreases from its value in the Ising model and reaches zero at a critical value Ω_c. For $\Omega > \Omega_c$ no transition occurs. Thus a ferroelectric transition occurs only when the electrostatic interactions are not too small in comparison with the zero-level splitting.
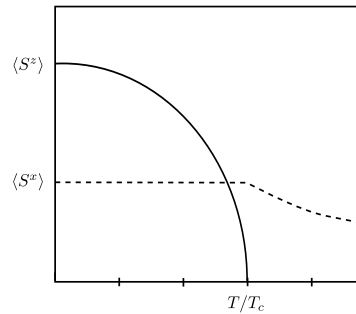

Fig. 2.10.: Qualitative temperature dependence of the pseudo-spin components $\langle S^z \rangle$ (solid) and $\langle S^x \rangle$ (dashed); adapted from [17].

Spin wave like excitations are found by random phase approximation (RPA) [99] both above and below T_c. The transverse Ising susceptibility has been studied in [100]. A Green's function technique [101, 102] offers a finite excitation energy and a phase transition.

In a more refined study, the TIM had been successfully adopted for ferroelectric bulk material using special decoupling procedures for the Green's function [103–107]. This second-order decoupling allows also to calculate the damping of the transverse and

longitudinal excitations [108]. Within this approach a new coordinate system is introduced by rotating the original one by the angle θ in the $x - z$ plane [103]. This rotation angle is determined by the requirement $\left\langle S^{x'} \right\rangle = 0$ in the new coordinate system. Instead of $S^{x'}$, $S^{y'}$ and $S^{z'}$ a new set including Pauli operators b and $b^\dagger$ is used in the rotated system. The quasi particle number is not conserved in the unrotated system, so the creation or annihilation of a pseudo-spin wave is allowed resulting in non-zero averaged values of $\langle b \rangle$ and $\langle b^\dagger \rangle$. These expressions are omitted by the rotation of the spin operators equivalent to the form presented in Section 2.2. The quantization axis is rotated by a site independent angle in the $x - z$ plane

$$\vec{\gamma}_f = \left(\sin\theta, 0, \cos\theta \right), \quad \text{with} \quad \vec{A}_f = \frac{1}{2}\left(\cos\theta, -\mathrm{i}, -\sin\theta \right). \tag{2.60}$$

The corresponding transformation of the spin operators for spin-$\frac{1}{2}$ particles with $\sigma_f = \frac{1}{2} - b_f^\dagger b_f = \frac{1}{2} - \rho_f$ reads:

$$S_f^x = \frac{1}{2}\left\{ (1 - 2\rho_f)\sin\theta + (b_f^+ + b_f)\cos\theta \right\}, \tag{2.61}$$

$$S_f^y = \frac{\mathrm{i}}{2}\left\{ (b_f^+ - b_f) \right\}, \tag{2.62}$$

$$S_f^z = \frac{1}{2}\left\{ (1 - 2\rho_f)\cos\theta - (b_f^+ + b_f)\sin\theta \right\}. \tag{2.63}$$

The rotated and Fourier transformed Hamiltonian, due to the translational invariance of the bulk material, reads:

$$\mathcal{H} = \mathcal{E}_0 + \mathcal{H}_0 + \mathcal{H}_1 \tag{2.64}$$

$$\mathcal{E}_0 = -\Omega N \sin\theta - \frac{N}{8}\cos^2\theta J_0 - \mu N E \cos\theta \tag{2.65}$$

$$\mathcal{H}_0 = +\sqrt{N}(2\Omega\sin\theta + \frac{1}{2}J_0\cos^2\theta + 2\mu E\cos\theta)\rho_0 - \frac{1}{4}\sin^2\theta\sum_{\mathbf{q}} J_{\mathbf{q}} b_{\mathbf{q}}^\dagger b_{\mathbf{q}} \tag{2.66}$$

$$\mathcal{H}_1 = \sqrt{N}(-\Omega\cos\theta + \frac{1}{4}J_0\sin\theta\cos\theta + \mu E\sin\theta)(b_0^\dagger + b_0) - \frac{1}{2}\cos^2\theta\sum_{\mathbf{q}} J_{\mathbf{q}}\rho_{\mathbf{q}}\rho_{-\mathbf{q}} \tag{2.67}$$

$$- \frac{1}{8}\sin^2\theta\sum_{\mathbf{q}} J_{\mathbf{q}}(b_{\mathbf{q}}^\dagger b_{-\mathbf{q}}^\dagger + b_{\mathbf{q}} b_{-\mathbf{q}}) - \frac{1}{2}\sin\theta\cos\theta\sum_{\mathbf{q}}(b_{\mathbf{q}}^\dagger + b_{-\mathbf{q}})\rho_{\mathbf{q}}$$

with

$$\rho_{\mathbf{k}} = \frac{1}{\sqrt{N}}\sum_{\mathbf{q}} b_{\mathbf{q}}^\dagger b_{\mathbf{k}+\mathbf{q}}. \tag{2.68}$$

The time dependence is described in the Heisenberg picture. The evolution in time depends on the system described by the equation of motion. The Fourier transformed commutator relations read

$$\left[b_{\mathbf{k}}, b_{\mathbf{q}}^{\dagger}\right]_{-} = \delta_{\mathbf{k},\mathbf{q}} - \frac{2}{\sqrt{N}}\rho_{\mathbf{k}-\mathbf{q}}, \quad \left[b_{\mathbf{k}}, \rho_{\mathbf{q}}\right]_{-} = \frac{1}{\sqrt{N}}b_{\mathbf{k}+\mathbf{q}}, \quad \left[b_{\mathbf{k}}^{\dagger}, \rho_{\mathbf{q}}\right]_{-} = -\frac{1}{\sqrt{N}}b_{\mathbf{k}-\mathbf{q}}^{\dagger}. \qquad (2.69)$$

The definition of the Fourier transformation is given in Section A.

2.6.1. Calculation of the Green's function - The equation of motion

The retarded Green's function in matrix form is defined as:

$$G_{\mathbf{k}}(t) = -\mathrm{i}\Theta(t)\left\langle\left[B_{\mathbf{k}}(t), B_{\mathbf{k}}^{\dagger}\right]_{-}\right\rangle = \begin{pmatrix} \langle\langle b_{\mathbf{k}}(t);\ b_{\mathbf{k}}^{\dagger}\rangle\rangle & \langle\langle b_{\mathbf{k}}(t);\ b_{-\mathbf{k}}\rangle\rangle & \langle\langle b_{\mathbf{k}}(t);\ \rho_{-\mathbf{k}}\rangle\rangle \\ \langle\langle b_{-\mathbf{k}}^{\dagger}(t);\ b_{\mathbf{k}}^{\dagger}\rangle\rangle & \langle\langle b_{-\mathbf{k}}^{\dagger}(t);\ b_{-\mathbf{k}}\rangle\rangle & \langle\langle b_{-\mathbf{k}}^{\dagger}(t);\ \rho_{-\mathbf{k}}\rangle\rangle \\ \langle\langle \rho_{\mathbf{k}}(t);\ b_{\mathbf{k}}^{\dagger}\rangle\rangle & \langle\langle \rho_{\mathbf{k}}(t);\ b_{-\mathbf{k}}\rangle\rangle & \langle\langle \rho_{\mathbf{k}}(t);\ \rho_{-\mathbf{k}}\rangle\rangle \end{pmatrix}$$
$$(2.70)$$

The two operators are formal defined as:

$$B_{\mathbf{k}}(t) = (b_{\mathbf{k}}(t),\ b_{-\mathbf{k}}^{\dagger}(t),\ \rho_{\mathbf{k}}(t))^{T}, \quad B_{\mathbf{k}}^{\dagger} = (b_{\mathbf{k}}^{\dagger},\ b_{-\mathbf{k}},\ \rho_{-\mathbf{k}}). \qquad (2.71)$$

Following the method of the equation of motion of the Green's functions, see Section 2.4.1, the resulting infinite system of Green's functions can not be solved exactly. Hence, a scheme to decouple and close these equation has to be used. The quality of the results depends on the quality of the approximations. Corresponding unphysical properties are due to the chosen decoupling. Aside mean-field approximation (MFA), where fluctuations are completely ignored, there are several other decoupling methods, such as RPA/ Hartree-Fock-approximation and more refined decoupling schemes [3, 109–111]. The Hamiltonian of the observed system $H = H_0 + H_1$ consists of the non-interacting H_0 and the interacting part H_1. The dynamics of the operator is determined by

$$i\frac{\partial}{\partial t}b_{\mathbf{k}} = \left[b_{\mathbf{k}}, H_0\right]_{-} + \left[b_{\mathbf{k}}, H_1\right]_{-} = \omega_{\mathbf{k}}b_{\mathbf{k}} + j_{b_k} \qquad (2.72)$$

In comparison to the Bloch picture [112], where the interactions of the collective modes (e.g. magnons) are completely ignored in the dispersion relation, the applied Pauli operators have more complicated kinematic properties than second quantized operators of Bose or Fermi type. Excitations in solids have a certain energy, which is accessible by first-order decoupling methods within the Green's function technique. The life-time of these excitations is unlimited without a damping. The determination of the damping is carried out by a second-order decoupling [113]. The method of the equation of motion

(Section 2.4.1) for the Green's function has the following form:

$$i\frac{\partial}{\partial t}G_{\mathbf{k}}(t) = \delta(t)\left\langle\left[b_{\mathbf{k}}, b_{\mathbf{k}}^{\dagger}\right]_{-}\right\rangle + \left(\omega_{\mathbf{k}} + R_{\mathbf{k}}(t)\right)G_{\mathbf{k}}(t) \tag{2.73}$$

with

$$\omega_{\mathbf{k}} = \frac{\left\langle\left[\left[b_{\mathbf{k}}, H_0\right]_{-}, b_{\mathbf{k}}^{\dagger}\right]_{-}\right\rangle}{\left\langle\left[b_{\mathbf{k}}, b_{\mathbf{k}}^{\dagger}\right]_{-}\right\rangle}, \quad R_{\mathbf{k}}(t) = \frac{\left\langle\left[j_{b_k}(t), b_{\mathbf{k}}^{\dagger}\right]_{-}\right\rangle}{\left\langle\left[b_{\mathbf{k}}(t), b_{\mathbf{k}}^{\dagger}\right]_{-}\right\rangle} \tag{2.74}$$

A formal integration of the equation of motion of the Green's function yields:

$$G_{\mathbf{k}}(t) = -i\Theta(t)\left\langle\left[b_{\mathbf{k}}, b_{\mathbf{k}}^{\dagger}\right]_{-}\right\rangle\exp\left\{-iE_{\mathbf{k}}(t)t\right\} \tag{2.75}$$

with the corresponding complex energy

$$E_{\mathbf{k}}(t) = \frac{\left\langle\left[\left[b_{\mathbf{k}}, H\right]_{-}, b_{\mathbf{k}}^{\dagger}\right]_{-}\right\rangle}{\left\langle\left[b_{\mathbf{k}}, b_{\mathbf{k}}^{\dagger}\right]_{-}\right\rangle} - \frac{i}{t}\int\limits_0^t\tau\left(\frac{\left\langle\left[j_{b_k}(t), j_{b_k^{\dagger}}(\tau)\right]_{-}\right\rangle}{\left\langle\left[b_{\mathbf{k}}(t), b_{\mathbf{k}}^{\dagger}(\tau)\right]_{-}\right\rangle}\right)d\tau \tag{2.76}$$

Here, the first term determines the energy of the excitations and the second term the associated damping, which is connected to the life-time of the modes within the crystal.

Within the generalized Hartree-Fock approximation the rotation angle θ is determined by the condition $\left\langle\left[b_{\mathbf{k}}, H\right]_{-}\right\rangle = 0$. This ensures a minimization of the free energy [103, 114] for the field free case

$$\begin{aligned}&1. \ \cos\theta = 0, \quad \theta = \frac{\pi}{2}, \qquad \text{if} \ \ T \geq T_c,\\&2. \ \sin\theta = \frac{4\Omega}{\langle\sigma\rangle J_0} = \frac{\langle\sigma\rangle_c}{\langle\sigma\rangle}, \quad \text{if} \ \ T \leq T_c.\end{aligned} \tag{2.77}$$

Here, the pseudo-spins precess around a mean field. There are three excitations, two transverse $\varepsilon_{1,2}(k)$ and one longitudinal $\varepsilon_3(k)$. The longitudinal mode describes the motion in the direction of the molecular field. The two other modes describe the precession of the pseudo-spins around the molecular field.

The pseudo-spin wave energies in this approximation without an external electric field in the paraelectric phase $(T > T_c)$ read

$$\varepsilon_{1,2} = \pm 2\Omega\sqrt{1 - \left(\frac{\langle\sigma\rangle}{\langle\sigma\rangle_c}\right)\frac{J_{\mathbf{k}}}{J_0}}, \tag{2.78}$$

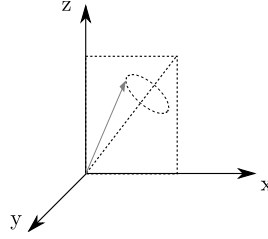$$\varepsilon_3 = 0 \tag{2.79}$$

Fig. 2.11.: Precession of the pseudo-spin around the mean field.

and for temperatures below the critical temperature $(T < T_c)$:

$$\varepsilon_{1,2} = \pm\sqrt{(\varepsilon_{\mathbf{k}}^{11})^2 - (\varepsilon_{\mathbf{k}}^{12})^2} = \pm\frac{\langle\sigma\rangle\, J_0}{2}\sqrt{1 - \left(\frac{\langle\sigma\rangle_c}{\langle\sigma\rangle}\right)^2 \frac{J_{\mathbf{k}}}{J_0}}, \qquad (2.80)$$

$$\varepsilon_3 = 0. \qquad (2.81)$$

with $\langle\sigma\rangle_c = \frac{4\Omega}{J_0}$. The full energies can be found in [103]. Pseudo-spin waves represent a propagating mode even in the paraelectric phase. Above the critical temperature the pseudo-spins precess around the molecular field directed along S^x. At very high temperatures the pseudo-spins behave like free particles. Approaching T_c the energy is reduced due to interaction between the pseudo-spins. At the critical temperature the excitation energy vanishes for $k = 0$. In the ferroelectric phase the interaction between the pseudo-spins results in a propagating mode, the soft mode of the pseudo-spin wave. The relative polarization $\langle\sigma\rangle$ is larger than the critical one $\langle\sigma\rangle_c$. Here the molecular field points along a general direction in the $x - z$ plane, i.e. it is no longer perpendicular to $\langle S^z\rangle$. Both mean values $\langle S^z\rangle$ and $\langle S^x\rangle$ are different from zero, hence longitudinal as well as the transverse modes contribute to the polarization fluctuations. The spin wave mode is critical only for $\mathbf{k} \to 0$, thus the phase transition is connected to a condensation of the quasi spin wave. For $J_{ij} > 0$ the mode becomes soft at the Brillouin zone center ($\mathbf{k} = 0$). The order parameter, the homogeneous spontaneous polarization represents the frozen-in soft normal mode coordinate.

Below T_c a soft pseudo-spin wave condenses. In contrast to magnons, pseudo-spin waves exhibit a propagating mode in the ferroelectric and the paraelectric phase. In ferromagnets magnons only exist in the low temperature phase. These pseudo-spin waves become soft for $k = 0$ in the vicinity of the critical temperature $T \to T_c$. The longitudinal mode with the energy $\varepsilon_3 = 0$ in both phases corresponds to a relaxation of the pseudo-spin components parallel to the mean field. The relative polarization in the direction of the

mean field is determined by:

$$\langle\sigma\rangle = \left(\frac{1}{N}\sum_{\mathbf{k}}(\frac{\varepsilon_{\mathbf{k}}^{11}(\langle\sigma\rangle)}{\varepsilon_{\mathbf{k}}(\langle\sigma\rangle)}\coth\frac{\varepsilon_{\mathbf{k}}(\langle\sigma\rangle)}{2T}\right)^{-1} \tag{2.82}$$

with

$$\varepsilon_{\mathbf{k}}^{11} = 2\Omega\sin\theta + \frac{1}{2}\langle\sigma\rangle J_0\cos^2\theta - \frac{1}{4}\sin^2\theta J_{\mathbf{k}}\langle\sigma\rangle - \frac{1}{N\langle\sigma\rangle}\sum_{\mathbf{q}}\left(\cos^2\theta J_{\mathbf{k-q}} - \frac{1}{2}\sin^2\theta J_{\mathbf{q}}\right)\bar{n}_{\mathbf{q}} \tag{2.83}$$

In case of damping, resulting from the scattering of quasi particles, the energy becomes complex and belongs to a damped motion of the pseudo-spins around the mean field. The transverse damping of pseudo-spin waves is very small at low temperatures. For moderate tunneling fields Ω the soft mode is underdamped almost in the whole temperature region [103]. Only in the vicinity of the critical point the damping increases strongly. Hence, the soft mode becomes overdamped approaching T_c. In the subsequent calculations approximations to the dynamics of the operators as $b_{\mathbf{k}}(t) \approx b_{\mathbf{k}}e^{-i\varepsilon_{\mathbf{k}}t}$ and the commutator relation $[b_{\mathbf{k}}, b_{\mathbf{k'}}^{\dagger}]_- = \langle\sigma\rangle\delta_{\mathbf{k,k'}}$ are made. The transverse damping is given by:

$$\gamma_{\mathbf{k}}^{11} = \frac{\pi}{2N^2}\sum_{\mathbf{pq}}[V_{\mathbf{q,k-q}} + V_{\mathbf{p+q-k,p+q}}]^2\left[\bar{n}_{\mathbf{p}}\left(\langle\sigma\rangle + \bar{n}_{\mathbf{p+q}} + \bar{n}_{\mathbf{k-q}}\right) - \bar{n}_{\mathbf{p+q}}\bar{n}_{\mathbf{k-q}}\right]*$$
$$* \delta\left(\varepsilon_{\mathbf{p+q}} + \varepsilon_{\mathbf{k-q}} - \varepsilon_{\mathbf{p}} - \varepsilon_{\mathbf{k}}\right) \tag{2.84}$$

The relaxational motion of the pseudo-spins along the mean field is determined by the longitudinal damping. For long wavelengths the damping $\gamma_{\mathbf{k}}^{33}$ decreases in the ordered phase and is equal to zero in the high temperature phase. The longitudinal damping reads:

$$\gamma_{\mathbf{k}}^{33} = \frac{\pi}{8N^2}\sin^2\theta\cos^2\theta\sum_{\mathbf{pq}}[J_{\mathbf{k-q}} + J_{\mathbf{q-p}}]^2\Big\{$$
$$\left[\bar{n}_{\mathbf{p}}\left(\langle\sigma\rangle + \bar{n}_{\mathbf{p+k-q}} + \bar{n}_{\mathbf{q}}\right) - \bar{n}_{p+k-q}\bar{n}_q\right]\delta\left(\varepsilon_{\mathbf{q}} + \varepsilon_{\mathbf{p+k-q}} - \varepsilon_{\mathbf{p}} - \varepsilon_{\mathbf{k}}\right)$$
$$+ \left[\bar{n}_{\mathbf{p+k-q}}\left(\langle\sigma\rangle + \bar{n}_{\mathbf{p}} + \bar{n}_{\mathbf{q}}\right) - \bar{n}_{\mathbf{p}}\bar{n}_{\mathbf{q}}\right]\delta\left(\varepsilon_{\mathbf{p}} + \varepsilon_{\mathbf{q}} - \varepsilon_{\mathbf{p+k-q}} - \varepsilon_{\mathbf{k}}\right)$$
$$+ \left[\bar{n}_{\mathbf{q}}\left(\langle\sigma\rangle + \bar{n}_{\mathbf{p+k-q}} + \bar{n}_{\mathbf{p}}\right) - \bar{n}_{\mathbf{p}}\bar{n}_{\mathbf{p+k-q}}\right]\delta\left(\varepsilon_{\mathbf{p}} + \varepsilon_{\mathbf{p+k-q}} - \varepsilon_{\mathbf{q}} - \varepsilon_{\mathbf{k}}\right)\Big\}$$
$$+ \frac{\pi}{16N}\sin^4\theta\sum_{\mathbf{q}}\Big\{[J_{\mathbf{q}} + J_{\mathbf{k-q}}]^2\left[\left(\langle\sigma\rangle + \bar{n}_{\mathbf{q}} + \bar{n}_{\mathbf{k-q}}\right)\right]\delta\left(\varepsilon_{\mathbf{q}} + \varepsilon_{\mathbf{k-q}} - \varepsilon_{\mathbf{k}}\right)$$
$$+ [J_{\mathbf{q}} - J_{\mathbf{k-q}}]^2\left[\left(\bar{n}_{\mathbf{q}} - \bar{n}_{\mathbf{k-q}}\right)\right]\left[\delta\left(\varepsilon_{\mathbf{k-q}} - \varepsilon_{\mathbf{q}} - \varepsilon_{\mathbf{k}}\right) - \delta\left(\varepsilon_{\mathbf{q}} - \varepsilon_{\mathbf{k-q}} - \varepsilon_{\mathbf{k}}\right)\right]\Big\} \tag{2.85}$$

with the abbreviations

$$
\begin{aligned}
V_{\mathbf{q},\mathbf{k}-\mathbf{q}} &= \cos^2\theta\, J_{\mathbf{q}} - \frac{1}{2}\sin^2\theta\, J_{\mathbf{k}-\mathbf{q}} \\
\bar{n}_{\mathbf{q}} = \left\langle b^\dagger b \right\rangle_{\mathbf{q}} &= \frac{1}{2}\left\langle \sigma \right\rangle \left[\frac{\varepsilon_{\mathbf{q}}^{11}}{\varepsilon_{\mathbf{q}}} \coth\frac{\beta\varepsilon_{\mathbf{q}}}{2} - 1 \right]
\end{aligned}
\tag{2.86}
$$

Here only contributions from spin wave scattering are considered, while terms responsible for the decay of one pseudo-spin wave into two or more and the inverse process are neglected.

3. Multiscale approach to ferroelectric bulk materials

3.1. Soft mode within the classical approach

Despite the great progress in explaining ferroelectric properties based on the microscopic model in Eq. (2.58), the system is studied in this chapter by using classical spin vectors as in the corresponding magnetic case [115]. The TIM is analyzed in its classical version capturing all the inherent quantum properties of the spin operators. Additionally, damping effects are investigated. Such an interest is also stimulated by the recent progress in studying ferromagnets, where the classical magnetic moments are assumed to obey the Landau-Lifshitz equation [115] and damping effects are included by the so called Gilbert-damping, see [116].

The results presented in this section are published in [117] The spin operators obey the equation of motion

$$i\hbar \frac{\partial S_r^\alpha}{\partial t} = [H,\, S_r^\alpha]\,. \tag{3.1}$$

Using the Hamiltonian Eq. (2.58) and Eq. (3.1) one gets

$$\frac{\partial S_r^x}{\partial t} = -\sum_{j(r)} J_{rj} S_j^z\, S_r^y \tag{3.2}$$

$$\frac{\partial S_r^y}{\partial t} = -\Omega S_r^z + \sum_{j(r)} J_{rj} S_j^z\, S_r^x \tag{3.3}$$

$$\frac{\partial S_r^z}{\partial t} = +\Omega\, S_r^y\,. \tag{3.4}$$

The effective field is defined by

$$h_r^\alpha = -\frac{\delta H}{\delta S_r^\alpha}\,. \tag{3.5}$$

The change-over to the classical limit $\vec{S}_r \to \vec{S}_r\, \hbar S(S+1)$ is carried out by $\hbar \to 0$ and $S \to \infty$. The discrete equation of motion for the corresponding vector field $\vec{S}_r(t)$ reads

$$\frac{\partial \vec{S}_r}{\partial t} = \vec{h}_r \times \vec{S}_r \quad \text{with} \quad \vec{h}_r = (\Omega, 0, \sum_{j(r)} J_{rj} S_j^z)\,. \tag{3.6}$$

Within the classical limit the spin vector has a spatially fixed length $\vec{S}^{\,2}$ reflecting the

conservation of the spin-operator $\vec{S}^2$ by $[H, \vec{S}^2] = 0$. In general the length can be a function of the temperature. Further the equation of motion can be written in a continuous description which should be adequate especially nearby to the phase transition in the form

$$\frac{\partial \vec{S}(\vec{x}, t)}{\partial t} = \vec{h}(\vec{x}, t) \times \vec{S}(\vec{x}, t) \,. \tag{3.7}$$

The effective field is also expressed in a continuous approximation as

$$\vec{h}(\vec{x}, t) = (\,\Omega,\, 0,\, J\kappa S^z(\vec{x}, t)\,) \,, \quad \text{with} \quad \kappa = a^2 \nabla^2 + z \tag{3.8}$$

where J is the coupling strength between the z nearest neighbors and a is the lattice spacing in a simple cubic lattice. This relation follows from

$$\sum_{j(r)} J_{rj} S_j^z \equiv \sum_{j(r)} J_{rj}(S_j^z - S_j^z + S_j^z) \simeq J(a^2 \nabla^2 + z) S^z(\vec{x}) \,. \tag{3.9}$$

Due to the TIM, Eq. (2.58), the effective field $\vec{h}$ is an anisotropic one, while in the Heisenberg model the effective field is isotropic [116]. In order to solve the evolution equation Eq. (3.7) the ansatz $\vec{S}(\vec{x}, t) = \vec{m}(\vec{x}) + \vec{\varphi}(\vec{x}, t)$ is made, where $\vec{m}(\vec{x}) = m_x \vec{e}_x + m_z \vec{e}_z$ is a time-independent but temperature dependent vector in the $x - z$ plane as suggested by Eq. (2.58). In case that $\vec{m}$ is spatial independent it describes the homogeneous polarization. In first order the fluctuating field $\vec{\varphi}$ obeys

$$\dot{\vec{\varphi}} = \vec{h}_1 \times \vec{m} + \vec{h}_0 \times \vec{\varphi}, \tag{3.10}$$

with $\vec{h}_0 = (\,\Omega, 0, Jzm_z\,)$, and $\vec{h}_1 = (\,0,\, 0,\, J\kappa\varphi_z\,)$. In deriving the last result the relation $\vec{m} \times \vec{h}_0 = 0$ is used, which defines the direction of the homogeneous polarization. The last relation gives rise to two solutions

$$\begin{aligned} m_z(T) \neq 0\,, \qquad m_x &= \frac{\Omega}{Jz} \quad \text{if} \quad T < T_c \\ m_z = 0\,, \quad m_x(T) &\neq \frac{\Omega}{Jz} \quad \text{if} \quad T > T_c\,. \end{aligned} \tag{3.11}$$

In the low temperature regime the x-component of the polarization is temperature independent. At T_c it results $m_x(T_c) = \Omega/Jz$. In the high temperature regime m_x decreases with increasing temperature. In terms of a multiscale approach the temperature dependence of m_x and m_z is calculated using the microscopic model Eq. (2.58). In mean-field approximation one gets $m_x(T) = \tanh \frac{\Omega}{T}$. The results are shown in Fig. 3.1. Notice that a finite phase temperature is only realized, if $\Omega < Jz$.
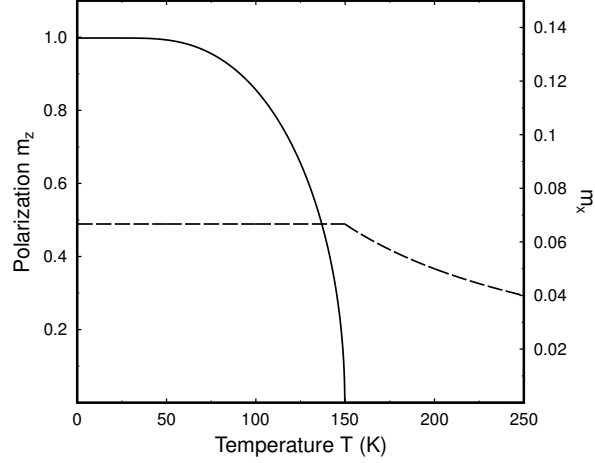
Fig. 3.1.: Temperature dependence of $m_z(T)$ (solid line) and $m_x(T)$ (dashed line) based on the microscopic model with $\Omega = 10\,\mathrm{K}$, $J = 25\,\mathrm{K}$.

The low temperature phase $T < T_c$ is discussed in the following part. The fluctuating field satisfies for finite $m_z \neq 0$ the coupled equations:

$$
\dot{\varphi}_x(\vec{q}, t) = -Jzm_z\varphi_y(\vec{q}, t)\,, \quad \dot{\varphi}_z(\vec{q}, t) = \Omega\varphi_y(\vec{q}, t)\,,
$$
$$
\dot{\varphi}_y(\vec{q}, t) = Jzm_z\varphi_x(\vec{q}, t) - [\,\Omega - m_xJ\kappa(\vec{q})\,]\varphi_z(\vec{q}, t)\,. \tag{3.12}
$$

Here the Fourier transformed $\kappa(\vec{q}) = z - (a\vec{q})^2$ is used, whereas the approach is only valid in the long wavelength limit $aq \ll 1$. The set of Eq. (3.12) allows a non-trivial solution $\varphi \propto \exp[i\varepsilon(\vec{q})t]$, if the excitation energy $\varepsilon_l(\vec{q})$ obeys

$$
\varepsilon_l(\vec{q}, T) = \sqrt{A_l^2 + B_l\vec{q}^2} \quad \text{with} \quad A_l(T) = Jzm_z\,, \quad B_l = \frac{a^2\Omega^2}{z}\,. \tag{3.13}
$$

The excitation energy below the critical temperature is dominated by the coupling J:

$$
\varepsilon_l(\vec{q}) = Jz\sqrt{m_z^2 + m_x^2\frac{a^2\vec{q}^2}{z}}\,, \tag{3.14}
$$

and the dispersion relation Eq. (3.13) reveals the typical soft mode behavior

$$
\lim_{T \to T_c} \varepsilon(\vec{q} = 0) = 0 \tag{3.15}
$$

in accordance to the microscopic behavior [101, 102, 118]. In a scaling form the dispersion

reads

$$\varepsilon_l(\vec{q}, \xi_c) = \xi_c^{-1} f_l(q\xi_c),$$ (3.16)

where ξ_c is the correlation length, $f_l(x) \propto \sqrt{1 + x^2}$ is the scaling function and the critical exponents fulfill $\nu = \beta$. The evolution equations for the fluctuating field can be solved leading to

$$\vec{\varphi}(\vec{q}, t) = R_l(\vec{q}) \left(\frac{Jzm_z e^{i\pi/2}}{\varepsilon_l(\vec{q})}, 1, \frac{\Omega e^{-i\pi/2}}{\varepsilon_l(\vec{q})} \right) \exp[i\varepsilon_l(\vec{q})t],$$ (3.17)

where $R_l(\vec{q})$ is the amplitude of the excitation mode determined by the initial condition. A phase shift appears between the different components. Making the same approach for the high temperature phase with $m_z = 0$, the dispersion relation offers the same structure as below T_c however with different coefficients

$$\varepsilon_h(\vec{q}) = \sqrt{A_h^2 + B_h \vec{q}^2}$$ (3.18)

$$A_h^2 = \Omega(\Omega - m_x(T)Jz), \; B_h = m_x(T)Ja^2\Omega.$$

Above the critical temperature, the excitation energy is dominated by the tunneling energy Ω and reads:

$$\varepsilon_h(\vec{q}) = \Omega \sqrt{\frac{m_x(T)}{m_x(T_c)} \frac{a^2 \vec{q}^2}{z} + \frac{m_x(T_c) - m_x(T)}{m_x(T_c)}}$$ (3.19)

In the high temperature phase the relation $m_x(T)/m_x(T_c) < 1$ is fulfilled as one can observe in Fig. 3.1. The fluctuation field $\vec{\varphi}(\vec{q})$ exhibits a similar form as for $T < T_c$, but setting $m_z = 0$ and replacing ε_l by ε_h. Thus the field $\vec{\varphi}$ is continuous at the phase transition. The dispersion relations, given by Eq. (3.18), shows likewise a soft-mode behavior, because the critical temperature T_c is defined by $m_x(T = T_c) = \frac{\Omega}{Jz}$ in accordance with Eq. (3.11). In the vicinity of T_c it results

$$A_h^2 = Jz\Omega[m_x(T_c) - m_x(T)] \simeq -Jz\Omega\frac{dm_x(T_c)}{dT}(T - T_c).$$ (3.20)

Combined with the mean-field result $m_x = \tanh\left(\frac{\Omega}{T}\right)$, the mode at $\vec{q} = 0$ satisfies

$$\varepsilon_h(\vec{q} = 0) = \sqrt{\frac{Jz\Omega^2}{T_c^2} \left[1 - \left(\frac{\Omega}{zJ}\right)^2 \right]} (T - T_c)^{1/2}.$$ (3.21)

This relation is only valid in case of $\Omega < Jz$. In the opposite case there is no phase transition at finite temperatures. Furthermore the stiffness constant B_h depends on the

temperature via $m_x(T)$ and remains finite at T_c with $B(T_c) = \frac{\Omega^2 a^2}{z}$.

3.2. Damping effect

The generalization the equation of motion Eq. (3.7) to include damping effects is given in the following part. Microscopically there is a great diversity of the origin of damping effects. An intrinsic reason for damping effects might be the mutual interaction between the excitation modes for different wave-vectors, which has been demonstrated in Section 2.6. Likewise the damping effects of the excitation modes can be originated by a coupling to phonons. Due to the interaction of the pseudo-spin excitations with the phonon modes there results a damping of the excitation modes which was shown recently in [119]. The intention of the present section is to discuss the general form of the evolution equation Eq. (3.7) with an additional damping part. As mentioned above, this can be achieved by taking into account the intrinsic interaction of the modes or by a coupling to additional degrees of freedom such as defects or phonons. As the result Eq. (3.7) has to be supplemented by a damping term $\vec{D}$ resulting in

$$\frac{\partial \vec{S}(\vec{x}, t)}{\partial t} = \vec{h}(\vec{x}, t) \times \vec{S}(\vec{x}, t) + \vec{D}(\vec{S}) \,. \tag{3.22}$$

The damping term $\vec{D}$ has a pure dynamical origin, so that possible static parts in the final equation, see Eq. (3.28), should be subtracted. Although due to the spin wave damping the length of $\vec{S}$ is not conserved one concludes that the non-trivial damping part is oriented into the direction of the effective field $\vec{h}$. Obviously the damping fulfills $\vec{D} < 0$, i.e.

$$\frac{\partial \vec{S}^2}{\partial t} = \vec{D} \cdot \vec{S} < 0 \,. \tag{3.23}$$

By the general concept of phase transitions [120] the following ansatz is made

$$D_\alpha = -\Lambda_{\alpha\beta}(\vec{S}) h_\beta \,. \tag{3.24}$$

In case of a positive definite matrix $\Lambda_{\alpha\beta}$, independent on $\vec{S}$, the last relation corresponds to the conventional relaxation dynamics for a non-conserved quantity. To get higher order terms one can expand the matrix $\Lambda_{\alpha\beta}$ in powers of $\vec{S}$ leading to

$$\Lambda_{\alpha\beta} = \Lambda_{\alpha\beta}^{(0)} + \Lambda_{\alpha\beta\gamma}^{(1)} S_\gamma + \Lambda_{\alpha\beta\gamma\delta}^{(2)} S_\gamma S_\delta + O(\vec{S}^3) \,. \tag{3.25}$$

The expansion parameters, denoted by Λ, will be determined in accordance with the behavior under time reversal and the underlying Lie group properties of the spin vectors

$\vec{S}$. Whereas the propagating part of the equation of motion, Eq. (3.7), is invariant under the instantaneous change $t \to -t$, $\vec{S} \to -\vec{S}$ and $\vec{h} \to -\vec{h}$, the damping part $\vec{D}$ should break the time reversal invariance. Due to this requirement and the fact $\vec{D} \propto \vec{h}$ one gets

$$\Lambda^{(0)}_{\alpha\beta} = \frac{1}{\tau_1}\delta_{\alpha\beta}\,, \tag{3.26}$$

where τ_1 plays the role of a relaxation time. The breaking of time reversal symmetry is only realized if the linear term in Eq. (3.25) disappears. The structure constants of the symmetry group of $\vec{S}$ are essentially given by the complete antisymmetric tensor $\varepsilon_{\alpha\beta\gamma}$. Furthermore, the damping should be pointed to the direction of the effective field and consequently the vector $\vec{D}$ is perpendicular to the propagating part $\vec{S} \times \vec{h}$. Summarizing these conditions the ansatz

$$\Lambda^{(1)}_{\alpha\beta\gamma} = b\,\varepsilon_{\alpha\beta\gamma}\,,$$
$$\Lambda^{(2)}_{\alpha\beta\gamma\delta} = \frac{1}{2\tau_2}\left[\,\varepsilon_{\alpha\beta\rho}\,\varepsilon_{\rho\gamma\delta} + \varepsilon_{\alpha\gamma\rho}\,\varepsilon_{\rho\beta\delta} + \varepsilon_{\alpha\delta\rho}\,\varepsilon_{\rho\beta\gamma}\,\right] \tag{3.27}$$

is made. The form of $\Lambda^{(1)}_{\alpha\beta\gamma}$ with an arbitrary parameter b guarantees that a linear term does not occur. In the conventional vector notation the complete equation of motion reads now

$$\frac{\partial \vec{S}}{\partial t} = \vec{h} \times \vec{S} - \frac{1}{\tau_1}\vec{h} - \frac{1}{\tau_2}\vec{S} \times (\vec{S} \times \vec{h})\,. \tag{3.28}$$

Two damping terms arise with the prefactors τ_1 and τ_2. Although the determination of both parameters is beyond the scope of the mesoscopic approach they should be of the order of a microscopic flip process and become of the same order $\tau_1 \simeq \tau_2$. They reflect the influence of the interaction between the excitations or the coupling to other degrees of freedom as discussed before. The last equation is similar to the Landau-Lifshitz equation with Gilbert-damping. In contrast to the isotropic ferromagnetic case the effective field $\vec{h}$ is anisotropic and directed in the $x-z$-plane. As the consequence the dispersion relation for the excitation energy, Eqs. (3.13, 3.18), are likewise different in comparison to the magnetic case. While isotropic magnetic systems offers a gapless Goldstone mode here due to the transverse field the dispersion relation becomes soft only for $T \to T_c$.

Making the same procedure as before, the dispersion relation in the high temperature phase is found in the form

$$\omega_h(\vec{q}) = \varepsilon_h(\vec{q}) + i\frac{\Gamma_{1h}(\vec{q})}{2\tau_1} + i\frac{\Gamma_{2h}(\vec{q})}{2\tau_2} \quad \text{with}$$
$$\Gamma_{1h}(\vec{q}) = J\kappa(\vec{q})\,, \quad \Gamma_{2h}(\vec{q},T) = m_x(T)\left[\,2\Omega - J\kappa(\vec{q})m_x(T)\,\right]\,. \tag{3.29}$$

The result is valid in the long wavelength limit and in first order in τ^{-1}. The propagating part $\varepsilon_h(\vec{q})$, written in Eq. (3.29), remains unchanged in first order in τ^{-1}. Higher order terms give rise to a slightly changed behavior. The appearance of the imaginary parts is related to damping effects, and the fluctuating field offers a behavior such as

$$\vec{\varphi}(\vec{q}, t) = R(\vec{q}) \exp\left[i\varepsilon(\vec{q}) - \frac{\Gamma_1(\vec{q}, T)}{2\tau_1} - \frac{\Gamma_2(\vec{q}, T)}{2\tau_2}\right] t \,. \tag{3.30}$$

The inverse functions Γ^{-1} plays the role of the life-time of the excitation energy. In the high temperature phase Γ_{1h} is temperature independent however it is dominated by the exchange coupling $\Gamma_{1h} \simeq Jz$. The damping function Γ_{2h} offers a weak temperature dependence and it is dominated by the tunneling energy Ω with $\Omega < Jz$. One gets

$$\Gamma_{2h}(\vec{q}, T = T_c) > \Gamma_{2h}(\vec{q} = 0, T = T_c) = \frac{\Omega^2}{Jz} \,. \tag{3.31}$$

The situation is drastically changed for $T \leq T_c$. Likewise the dispersion relation $\omega_l(\vec{q}, T)$ offers a real and an imaginary part according to Eq. (3.29). The real part $\varepsilon_l(\vec{q}, T)$ remains unchanged in lowest order of τ^{-1} and is given by Eq. (3.13). It characterizes the excitation energy. The finite life-time of the excitation is related to the temperature and wave vector dependent damping terms.

$$\Gamma_{1l}(\vec{q}, T) = J\kappa(\vec{q})\left[1 - \frac{A_l^2}{\varepsilon_l^2(\vec{q})}\right] \equiv \frac{J\kappa(\vec{q})B_l}{\varepsilon_l^2(\vec{q})}q^2,$$
$$\Gamma_{2l}(\vec{q}, T) = \frac{\varepsilon_l^2(\vec{q}) + A_l^2 + \Omega^2}{Jz} \quad \text{with} \quad \kappa(\vec{q}) = z - (a\vec{q})^2 \,. \tag{3.32}$$

At the critical point the damping is continuous, i.e for instance $\Gamma_{1l}(\vec{q}, T_c) = \Gamma_{1h}(\vec{q}, T_c)$. While the life-time in the high temperature phase is only weakly temperature dependent, it depends on T in the low temperature regime via m_z which disappears at T_c with a critical exponent $\beta \leq 1/2$. The temperature dependence of the excitation energy and the relevant life-time $(\Gamma_{2l})^{-1}$ of the soft mode at $\vec{q} = 0$ are depicted in Fig. 3.2 .

Whereas the excitation energy ε_l disappears for $T \to T_c$ at $\vec{q} = 0$, the inverse life-time Γ_{2l} increases strongly at the phase transition but remains fixed at T_c. Apparently one finds

$$\Gamma_{1l}^{-1}(\vec{q}, T_c) < \Gamma_{1l}^{-1}(\vec{q}, T) \,, \tag{3.33}$$

i.e. the life of the excitation is shorter at the critical temperature as in the the low temperature regime. When the system is approaching to the phase transition temperature, the elementary excitation decays more rapidly for wave vector $\vec{q} \neq 0$.
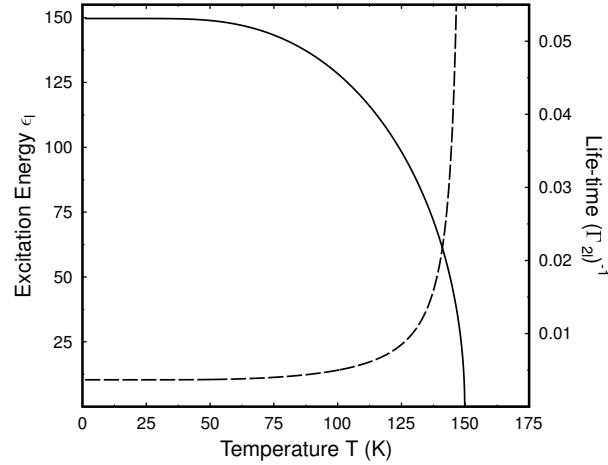
Fig. 3.2.: Excitation energy $\varepsilon(\vec{q} = 0)$ (solid curve) and the life-time $(\Gamma_{2l})^{-1}$ (dashed curve) at $\vec{q} = 0$ as function of the temperature, $\Omega = 10\,\text{K}, J = 25\,\text{K}$.

3.3. Stochastic equation

To refine the model further, all the residual degrees of freedom, not taken into account so far, are included in a stochastic force $\vec{\xi}(\vec{x}, t)$. Then Eq. (3.28) is supplemented by a noise term [120] leading to the final form

$$\frac{\partial \vec{S}}{\partial t} = \vec{h} \times \vec{S} - \frac{1}{\tau_1}\vec{h} - \frac{1}{\tau_2}\vec{S} \times (\vec{S} \times \vec{h}) + \vec{\xi}(\vec{x}, t)$$

$$< \xi_\alpha(\vec{x}, t)\xi_\beta(\vec{x}', t') > = 2T\delta_{\alpha\beta}\delta(\vec{x} - \vec{x}')\delta(t - t') \tag{3.34}$$

Even such an additive noise term should influence the damping part apparently. Alternatively one could also discuss a stochastic field which leads to a multiplicative noise. That situation has been considered in [121] studying ferromagnetic resonance. The influence of a rotating magnetic field is analyzed in [122]. In the framework of the TIM the situation is more complicated and should be considered separately. Making the same ansatz as before $\vec{S} = \vec{m} + \vec{\varphi}$, Eq. (3.34) reads in the low temperature phase

$$\frac{\partial \varphi_\alpha(\vec{q}, t)}{\partial t} = Y_{\alpha\beta}(\vec{q})\,\varphi_\beta(\vec{q}, t) + \xi_\alpha(\vec{q}, t) \tag{3.35}$$

Here **Y** is a 3×3 matrix

$$
Y_{\alpha\beta} = \begin{pmatrix} -\frac{m_z A_l}{\tau_2} & -A_l & \frac{m_z B_l q^2}{\Omega \tau_2} \\ A_l & -\frac{\Omega^2 + A_l^2}{Jz\tau_2} & -\frac{B_l q^2}{\Omega} \\ \frac{m_z \Omega}{\tau_2} & \Omega & -\frac{J\kappa(\vec{q})}{\tau_1} - \frac{B_l q^2}{Jz\tau_2} \end{pmatrix}
$$

where the coefficients A_l and B_l are defined in Eq. (3.13). From here the Green's function is obtained via

$$
G_{\alpha\beta}(t, t') = \left\langle \frac{\delta\varphi_\alpha(t)}{\delta\xi_\beta(t')} \right\rangle \quad t > t' \,. \tag{3.36}
$$

After performing Fourier transformation the Green's function is simply

$$
\mathbf{G}(\vec{q}, \omega) = -[\,i\omega\mathbf{I} + \mathbf{Y}(\vec{q})]^{-1} \,.
$$

As the result the Green's function is written in lowest order in τ as

$$
G_{\alpha\beta} = \frac{g_{\alpha\beta}(\vec{q}, \omega)}{[\omega + \omega_l(\vec{q})][\omega - \omega_l^*(\vec{q})][i\omega - \omega_d(\vec{q})]} \quad \text{with}
$$

$$
\omega_l(\vec{q}) = \varepsilon_l(\vec{q}) + i\frac{\Gamma_{1l}(\vec{q})}{2\tau_1} + i\frac{\Gamma_{2l}(\vec{q})}{2\tau_2}; \quad \omega_d(\vec{q}) = \frac{\Gamma_1(\vec{q})A_l^2}{\tau_1\left[\varepsilon_l^2(\vec{q}) - A_l^2\right]} \,. \tag{3.37}
$$

The influence of the noise is twofold. Once the dispersion relation of the low temperature phase, obtained already in Eqs. (3.13, 3.32), are reconfirmed as the complex poles $\omega_l(\vec{q})$ and $\omega_l^*(\vec{q})$ of the Green's function. Otherwise there appears an additional pure imaginary pole $\omega_d(\vec{q})$. This mode is a dissipative one, which is originated by the stochastic force. In lowest order in τ^{-1} the mode is only influence by τ_1. The matrix elements are given by

$$
g_{11} = -\omega^2 - i\omega\left[\frac{\Omega + \varepsilon_l^2}{Jz\tau_2} + \frac{J\kappa(\vec{q})}{\tau_1}\right] + B_l q^2 \,,
$$

$$
g_{22} = \omega^2 - i\omega\left[\frac{\varepsilon_l^2}{Jz\tau_2} + \frac{J\kappa(\vec{q})}{\tau_1}\right] \,, \quad g_{33} = -\omega^2 - i\omega\frac{2A_l^2 + \Omega^2}{Jz\tau_2} + A_l^2 \,,
$$

$$
g_{12} = A_l[i\omega - \frac{J\kappa}{\tau_1}] = -g_{21} \,, \quad g_{23} = \frac{i\omega B_l q^2}{\Omega} = -\frac{B_l q^2 g_{32}}{\Omega^2} \,,
$$

$$
g_{13} = \frac{B_l q^2}{\Omega}\left[A_l - \frac{i\omega m_z}{\tau_2}\right] = \frac{B_l q^2 g_{31}}{\Omega^2} \,. \tag{3.38}
$$

To illustrate the influence of the noise term the special case $m_z = 0$ and the inclusion of damping proportional to τ_1^{-1} in Eq. (3.28) is considered. The coupled set of equations

for the time-dependent part $\vec{\varphi}(\vec{q}, t)$ reads

$$
\begin{aligned}
\dot{\varphi}_x &= \xi_x \\
\dot{\varphi}_y &= (m_x J \kappa(\vec{q}) - \Omega) \varphi_z + \xi_y \\
\dot{\varphi}_z &= \Omega \varphi_y - \frac{1}{\tau_1} J \kappa(\vec{q}) \varphi_z + \xi_z
\end{aligned}
\tag{3.39}
$$

The first equation can be immediately solved. It results

$$
\langle \varphi_x^2(\vec{x}, t) \rangle = \varphi_x^2(\vec{x}, 0) + 2Tt \, .
\tag{3.40}
$$

Due to the stochastic force the x-component of the fluctuating field offers a diffusive behavior. The remaining Green's function is then a 2×2 matrix

$$
\mathbf{G}(\omega, \vec{q}) = \frac{1}{[\omega - \omega_h^*(\vec{q})][\omega + \omega_h(\vec{q})]}
\begin{pmatrix}
i\omega - \frac{\Gamma_1(\vec{q})}{\tau_1} & \Omega - m_x J \kappa(\vec{q}) \\
-\Omega & i\omega
\end{pmatrix}
\tag{3.41}
$$

The poles of this function are already given in Eq. (3.29). The Ising model in a transverse field shows cross-correlation which is also visible in the correlation function defined by

$$
C_{\alpha\beta}(\vec{q}, \omega) = <\varphi_\alpha(\vec{q}, \omega) \varphi_\beta^\dagger(\vec{q}, \omega)> \, ,
\tag{3.42}
$$

The fluctuation-dissipation theorem is fulfilled

$$
C_{\alpha\beta}(\vec{q}, \omega) = \frac{2T}{\omega} \Im \, G_{\alpha\beta}(\vec{q}, \omega) \, .
\tag{3.43}
$$

The correlation function follows

$$
\mathbf{C} = \frac{2T}{(\omega^2 - \varepsilon_h^2(\vec{q}))^2 + \left(\frac{(\Gamma_{1h}(\vec{q}))}{\tau_1}\right)^2}
\begin{pmatrix}
\omega^2 - \varepsilon_h^2(\vec{q}) + \left(\frac{\Gamma_{1h}(\vec{q})}{\tau_1}\right)^2 & -\frac{\Gamma_{1h}(\vec{q})}{\tau_1} [\Omega - m_x J \kappa(\vec{q})] \\
-\frac{\Gamma_{1h}(\vec{q})}{\tau_1} \Omega & \omega^2 - \varepsilon_h^2(\vec{q})
\end{pmatrix}
\tag{3.44}
$$

In the context presented here, the stochastic equations with an additive noise term does not give more information as the conventional equations. The situation is different for a multiplicative noise, where for instance the effective field $\vec{h}$ is supplemented by a stochastic force.

4. Many-particle approach to ferroelectric nanostructure

4.1. The model

The approach for the investigation of ferroelectric nanostructures is based on the TIM, where the ordering of functional groups are assigned to the two eigenvalues of the z-component of a spin operator (Section 2.5). Due to this inherent basic mechanism the applicability of the model was extended to thin films, recently [4, 119, 123–131].

Occurring surface and size effects in ferroelectric nanoparticles and thin films modify the interaction parameter between nearest neighbors for bulk and surface constituents. In the same manner Ω_b and Ω_s represent transverse fields in the bulk and surface shell. The Hamiltonian of the TIM including both, bulk and surface properties reads

$$H = -\frac{1}{2} \sum_{ij} J_{ij} S_i^z S_j^z - \Omega_b \sum_{i \varepsilon b} S_i^x - \Omega_s \sum_{i \varepsilon s} S_i^x - 2\mu E \sum_i S_i^z \,, \qquad (4.1)$$

where S_i^x and S_i^z are components of spin-$\frac{1}{2}$ operators and the sums are performed over the internal and surface lattice points, respectively. The interaction between the pseudo-spins at the surface shell is denoted as $J_{ij} = J_s$, whereas the bulk interaction strength is J_b.

The influence of defects is considered by the approximation of a coupling parameter J_d indicating the interaction of defect spins, which is different to the non-defect case J_b. In the same manner Ω_d represents the transverse fields within the defect shell or layer. The variation of the interaction strength is reasonable because the interaction parameter $J_{ij} \equiv J(r_i - r_j)$ depends on the distance between the spins. Consequently the interaction strength should vary with the lattice symmetry and the number of nearest neighbors.

The three dimensional ferroelectric layer system (Fig. 4.1) on a simple cubic lattice is composed of N layers in z-direction. The layers are numbered by $n = 1, ...N$, where the layers $n = 1$ and $n = N$ represent the two surfaces of the system with the modified coupling parameters J_s and Ω_s. The bulk is established by the remaining $(N - 2)$ layers.

Defects in the ferroelectric thin film are incorporated by defect layers with the interaction energy J_d and the transverse field Ω_d. The size of the defect is governed by the number of defect layers within the film. As in the pure bulk case, a new coordinate system is introduced by rotating the original one, used in Eq. (4.1), by the angle θ in the $x - z$ plane.
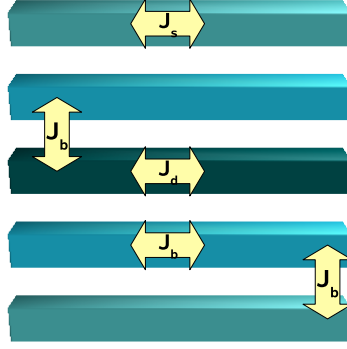
Fig. 4.1.: Scheme for a ferroelectric thin film with five layers. The middle one is defect.

The rotation angle θ is determined by the requirement $\langle S^{x'} \rangle = 0$ in the new coordinate system. The conditions of the low and high temperature case are given in Section 2.6.

The considered spherical ferroelectric particles (Fig. 4.2) are characterized by fixing the origin at a certain pseudo spin in the center of the particle. All the rest of them within the particle are ordered in shells, which are numbered by $n = 0, 1, ..., N$. Here $n = 0$ denotes the central pseudo-spin and $n = N$ represents the surface of the system with the modified parameters J_s and Ω_s.
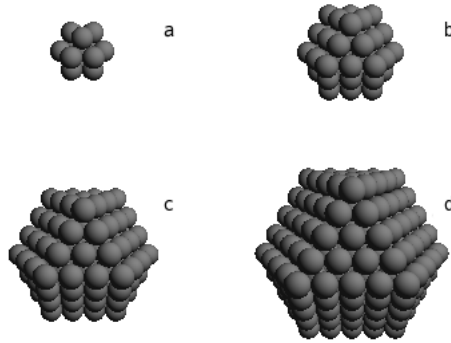

Fig. 4.2.: Ferroelectric nanoparticles of different size, composed of shells. Each sphere represents a pseudo-spin situated in the center, where (a) consists of one central spin plus $N = 1$ shell, (b) $N = 2$, (c) $N = 3$, (d) $N = 4$

4.2. Green's function approach to ferroelectric thin films

The Green's function is defined following Section 2.4 with $\hbar = 1$:

$$G_{ij}(t) = \ll b_i(t); b_j^\dagger(0) \gg \equiv i\Theta(t - t')\langle [b_i(t)b_j^\dagger(0) - b_j^\dagger(0)b_i(t)] \rangle. \tag{4.2}$$

where b and $b^\dagger$ are the Pauli operators in the rotated system. On introducing the two-dimensional Fourier transform $G_{n_i n_j}(\mathbf{k}_\parallel, \omega)$, one has the following form:

$$\ll b_i; b_j^\dagger \gg_\omega = \frac{\langle \sigma \rangle}{N'} \sum_{\mathbf{k}_\parallel} \exp(i\mathbf{k}_\parallel (\mathbf{r}_i - \mathbf{r}_j)) G_{n_i n_j}(\mathbf{k}_\parallel, \omega), \tag{4.3}$$

where N' is the number of sites in any of the lattice planes, $\mathbf{r}_i$ and n_i represent the position vectors of site i and the layer index, respectively, $\mathbf{k}_\parallel = (k_x, k_y)$ is a two-dimensional wave vector parallel to the surface. The summation is taken over the first Brillouin zone.

As a result the equation of motion for the Green's function Eq. (4.3) of the ferroelectric thin film for $T \leq T_c$ has the following matrix form:

$$\mathbf{H}(\omega)\mathbf{G}(\mathbf{k}_\parallel, \omega) = \mathbf{R}, \tag{4.4}$$

where $\mathbf{H}$ can be expressed as:

$$\mathbf{H} = \begin{pmatrix} \omega - V_1 + i\gamma_1 & k_1 & 0 & 0 & 0 & 0 & \dots \\ k_2 & \omega - V_2 + i\gamma_2 & k_2 & 0 & 0 & 0 & \dots \\ 0 & k_3 & \omega - V_3 + i\gamma_3 & k_3 & 0 & 0 & \dots \\ \vdots & \vdots & \vdots & \vdots & \vdots & \vdots & \ddots \\ 0 & 0 & 0 & 0 & 0 & k_N & \omega - V_N + i\gamma_N \end{pmatrix}$$

In order to obtain the solutions of the matrix Eq. (4.4), the two-dimensional column matrices, $\mathbf{G}_m$ and $\mathbf{R}_m$ is introduced, where the elements are given by $(\mathbf{G}_n)_m = G_{mn}$ and $(\mathbf{R}_n)_m = \langle \sigma \rangle_n \delta_{mn}$, so that Eq. (4.4) yields

$$\mathbf{H}(\omega)\mathbf{G}_n = \mathbf{R}_n. \tag{4.5}$$

From Eq. (4.5), $G_{nn}(\omega)$ is obtained as:

$$G_{nn}(\omega) = \frac{|H_{nn}(\omega)|}{|H(\omega)|}. \tag{4.6}$$

The quantity $|H_{nn}(\omega)|$ is the determinant made by replacing the n-th column of the

determinant $|H(\omega)|$ by R_n. The poles ω_n of the Green's function $G_{nn}(\omega)$ can be calculated by solving $|H(\omega)| = 0$. The rotation angle θ is determined as in the bulk case Section 2.6.

The relative polarization of the n-th layer given by

$$\langle \sigma_n \rangle = \left(\frac{\langle \sigma_n \rangle J_n}{2N} \sum_{\mathbf{k}_{\parallel}} \frac{1 - 0.5 \sin^2 \theta_n \gamma(\mathbf{k}_{\parallel})}{\omega_n} \coth \frac{\omega_n}{2T} \right)^{-1}. \tag{4.7}$$

has to be solved numerically. Due to the assumption of symmetrical surfaces, there are $\frac{1}{2}N$ layer polarizations, which have to be solved self-consistently. The dependence of the Curie temperature T_c on the film thickness N, was obtained by solving Eq. (4.7) as well.

The damping of the ferroelectric excitations reads

$$\begin{aligned}
\gamma_n =& \frac{\pi}{2N^2} \sum_{\mathbf{p}_{\parallel}, \mathbf{q}_{\parallel}} \Big[(\bar{V}_n(\mathbf{q}_{\parallel}, \mathbf{k}_{\parallel} - \mathbf{q}_{\parallel}) + \bar{V}_n(\mathbf{k}_{\parallel} - \mathbf{p}_{\parallel} - \mathbf{q}_{\parallel}, \mathbf{p}_{\parallel} + \mathbf{q}_{\parallel}))^2 \\
&* [\bar{n}_n(\mathbf{p}_{\parallel})(\langle \sigma_n \rangle + \bar{n}_n(\mathbf{p}_{\parallel} + \mathbf{q}_{\parallel}) + \bar{n}_n(\mathbf{k}_{\parallel} - \mathbf{q}_{\parallel})) \\
&- \bar{n}_n(\mathbf{p}_{\parallel} + \mathbf{q}_{\parallel})\bar{n}_n(\mathbf{k}_{\parallel} - \mathbf{q}_{\parallel})] \\
&* \delta(\varepsilon_n(\mathbf{k}_{\parallel} - \mathbf{q}_{\parallel}) + \varepsilon_n(\mathbf{p}_{\parallel} + \mathbf{q}_{\parallel}) - \varepsilon_n(\mathbf{p}_{\parallel}) - \varepsilon_n(\mathbf{k}_{\parallel})) \\
&+ [(J_{n-1}\gamma(\mathbf{q}_{\parallel}) \cos^2 \theta_{n-1})^2 + (J_{n-1}\gamma(\mathbf{k}_{\parallel} - \mathbf{p}_{\parallel} - \mathbf{q}_{\parallel}) \cos^2 \theta_{n-1})^2] \\
&* [\bar{n}_{n-1}(\mathbf{p}_{\parallel})(\sigma_{n-1} + \bar{n}_{n-1}(\mathbf{p}_{\parallel} + \mathbf{q}_{\parallel}) + \bar{n}_{n-1}(\mathbf{k}_{\parallel} - \mathbf{q}_{\parallel})) \\
&- \bar{n}_{n-1}(\mathbf{p}_{\parallel} + \mathbf{q}_{\parallel})\bar{n}_{n-1}(\mathbf{k}_{\parallel} - \mathbf{q}_{\parallel})] \\
&* \delta(\varepsilon_{n-1}(\mathbf{k}_{\parallel} - \mathbf{q}_{\parallel}) + \varepsilon_{n-1}(\mathbf{p}_{\parallel} + \mathbf{q}_{\parallel}) - \varepsilon_{n-1}(\mathbf{p}_{\parallel}) - \varepsilon_{n-1}(\mathbf{k}_{\parallel})) \\
&+ [(J_{n+1}\gamma(\mathbf{q}_{\parallel}) \cos^2 \theta_{n+1})^2 + (J_{n+1}\gamma(\mathbf{k}_{\parallel} - \mathbf{p}_{\parallel} - \mathbf{q}_{\parallel}) \cos^2 \theta_{n+1})^2] \\
&* [\bar{n}_{n+1}(\mathbf{p}_{\parallel})(\sigma_{n+1} + \bar{n}_{n+1}(\mathbf{p}_{\parallel} + \mathbf{q}_{\parallel}) + \bar{n}_{n+1}(\mathbf{k}_{\parallel} - \mathbf{q}_{\parallel})) \\
&- \bar{n}_{n+1}(\mathbf{p}_{\parallel} + \mathbf{q}_{\parallel})\bar{n}_{n+1}(\mathbf{k}_{\parallel} - \mathbf{q}_{\parallel})] \\
&* \delta(\varepsilon_{n+1}(\mathbf{k}_{\parallel} - \mathbf{q}_{\parallel}) + \varepsilon_{n+1}(\mathbf{p}_{\parallel} + \mathbf{q}_{\parallel}) - \varepsilon_{n+1}(\mathbf{p}_{\parallel}) - \varepsilon_{n+1}(\mathbf{k}_{\parallel})) \Big],
\end{aligned}$$

The detailed expressions V_n and k_n for $n = 1, \ldots, N$ can be found in Section A.

4.3. Green's function approach to ferroelectric nanoparticles

The Green's function $\ll b_l(t); b_m^\dagger(0) \gg$ contains all the information about the system. Due to the lack of translational invariance the subsequent calculation has to be performed in the real space. The average is defined in the conventional way, (Section 2.4)

$$\langle \sigma_l \rangle = \frac{Tr(\sigma_l \exp(-\beta H))}{Tr \exp(-\beta H)} \, . \tag{4.8}$$

The operators $b_l, b_m^\dagger$ are the Pauli operators in the rotated system. The rotation of the coordinate system is carried out following the transformation presented in Section 2.6.

$$S_l^x = \frac{1}{2} \left\{ \left(1 - 2b_l^\dagger b_l \right) \sin \theta_l + \left(b_l^\dagger + b_l \right) \cos \theta_l \right\} \tag{4.9a}$$

$$S_l^y = \frac{i}{2} \left(b_l^\dagger - b_l \right) \tag{4.9b}$$

$$S_l^z = \frac{1}{2} \left\{ \left(1 - 2b_l^\dagger b_l \right) \cos \theta_l - \left(b_l^\dagger + b_l \right) \sin \theta_l \right\} \tag{4.9c}$$

In case of ferroelectric nanoparticles the rotation angle θ_l is site dependent due to the loss of translational invariance.

$$
\begin{aligned}
H = {} & - 2\Omega \sum_i \left\{ \sigma_i \sin \theta_i + \frac{1}{2} \left(b_i + b_i^\dagger \right) \cos \theta_i \right\} - 2\mu E \sum_i \left\{ \sigma_i \cos \theta_i - \frac{1}{2} \left(b_i + b_i^\dagger \right) \sin \theta_i \right\} \\
& - \frac{1}{2} \sum_{i,j} J_{ij} \left\{ \cos \theta_i \cos \theta_j \sigma_i \sigma_j - \cos \theta_i \sin \theta_j \left(\sigma_i b_j^\dagger + \sigma_i b_j \right) \right. \\
& \left. + \frac{1}{4} \sin \theta_i \sin \theta_j \left(b_i^\dagger + b_i \right) \left(b_j^\dagger + b_j \right) \right\}
\end{aligned}
\tag{4.10}
$$

The Hamiltonian in the rotated coordinate system (4.10) is likewise the starting point to include further degrees of freedom as impurities and doping. Using the method firstly introduced in [113] and modifying it for calculations in real space the excitation energy, occasionally denoted as pseudo-spin-wave energy is obtained. The dynamics of the operator is given as:

$$
\begin{aligned}
\left[b_l, H \right]_- = {} & - 2\Omega \left\{ -b_l \sin \theta_l + \sigma_l \cos \theta_l \right\} + 2\mu E \left\{ b_l \cos \theta_l + \sigma_l \sin \theta_l \right\} \\
& - \frac{1}{2} \sum_i J_{li} \left\{ -2 \cos \theta_i \cos \theta_l b_l \sigma_i + \cos \theta_l \sin \theta_i \left(b_l b_i^\dagger + b_l b_i \right) \right. \\
& \left. - 2 \cos \theta_i \sin \theta_l \sigma_l \sigma_i + \sin \theta_l \sin \theta_i \left(b_i^\dagger \sigma_l + b_i \sigma_l \right) \right\}
\end{aligned}
$$

The full equation of motion reads:

$$\omega \langle\langle b_l; b_n^\dagger \rangle\rangle_\omega = \left\langle \left[b_l, b_n^\dagger \right]_\eta \right\rangle + \langle\langle [b_l, H]_-; b_n^\dagger \rangle\rangle_\omega$$

$$= \left\langle \left[b_l, b_n^\dagger \right]_\eta \right\rangle + (2\Omega \sin\theta_l + 2\mu E \cos\theta_l) \langle\langle b_l; b_n^\dagger \rangle\rangle_\omega - (2\Omega \cos\theta_l - 2\mu E \sin\theta_l) \langle\langle \sigma_l; b_n^\dagger \rangle\rangle_\omega$$

$$- \frac{1}{2} \sum_i J_{il} \Big\{ -2\cos\theta_i \cos\theta_l \langle\langle b_l \sigma_i; b_n^\dagger \rangle\rangle_\omega + \cos\theta_l \sin\theta_i \left(\langle\langle b_l b_i^\dagger; b_n^\dagger \rangle\rangle_\omega + \langle\langle b_l b_i; b_n^\dagger \rangle\rangle_\omega \right)$$

$$- 2\cos\theta_i \sin\theta_l \langle\langle \sigma_l \sigma_i; b_n^\dagger \rangle\rangle_\omega + \sin\theta_l \sin\theta_i \left(\langle\langle b_i^\dagger \sigma_l; b_n^\dagger \rangle\rangle_\omega + \langle\langle b_i \sigma_l; b_n^\dagger \rangle\rangle_\omega \right) \Big\}$$

$$(4.11)$$

The rotation of the coordinate system under the condition $\langle b_l \rangle = \langle b_l^\dagger \rangle = 0$ enables the decoupling of the equation of motion of the Green's function in generalized Hartree-Fock approximation.

$$\omega G_{lm} = 2\langle \sigma_l \rangle \delta_{lm} + \left[2\Omega_l \sin\theta_l + 2\mu E \cos\theta_l + \sum_j J_{lj} \cos\theta_l \cos\theta_j \langle \sigma_j \rangle \right.$$

$$\left. + \frac{1}{2} \sum_j J_{lj} \sin\theta_l \sin\theta_j \langle b_l b_j^\dagger \rangle \right] G_{lm} \qquad (4.12)$$

$$- \frac{1}{2} \sum_j J_{lj} \left[\sin\theta_l \sin\theta_j \langle \sigma_l \rangle + 2\cos\theta_j \cos\theta_l \langle b_l b_j^\dagger \rangle \right] G_{jm}$$

and in RPA

$$\sum_i \left\{ (\omega - 2\Omega \sin\theta_l - 2\mu E \cos\theta_l - \cos\theta_l \sum_j J_{jl} \cos\theta_j \langle \sigma_j \rangle) \delta_{li} + \frac{1}{4} \sin\theta_l J_{il} \sin\theta_i \right\} \langle\langle b_i; b_n^\dagger \rangle\rangle_\omega$$

$$= 2 \langle \sigma_l \rangle \delta_{l,n} .$$

$$(4.13)$$

Abnormal Green's functions of the form $\langle\langle b_i^\dagger; b_n^\dagger \rangle\rangle_\omega$ are are not taken into account. The coefficient matrix is symmetric with respect to the commutation of the lattice sites (l, i) by the replacement of $\langle \sigma_l \rangle = \frac{1}{2}$ in the non-diagonal terms. This system of equations has to be solved numerically and will be treated in matrix representation.

The given system of equations (Eq. (4.13)) can be written in compact matrix notation, similar to [132],

$$(\omega E - A)G = C , \qquad (4.14)$$

where the Green's function matrix G has to be calculated. The matrix A contains the coefficients obtained by the decoupling. The unity matrix is denoted as E. Hence, only

the diagonal elements depends on ω. The matrix C on the right hand site is contains the associated inhomogeneities and is diagonal $c_{ij} = c_i \delta_{ij}$. An orthogonal transformation across the matrix $U^T U = 1$ transforms the system into diagonal form and the formal solution looks like:

$$\underbrace{U^T(\omega E - A)U}_{\bar{A}} U^T G U = U^T C U \quad \leftrightarrow \quad \bar{G} = \bar{A}^{-1} U^T C U . \tag{4.15}$$

The transformation matrix is defined as $U = (u_1, u_2, \ldots, u_n)$ and $U^T = (\tilde{u}_1, \tilde{u}_2, \ldots, \tilde{u}_n)$ with the eigenvectors u_i of the matrix A as column vectors. The element u_{lk} is the lth component of the kth eigenvector. The matrix $\bar{A}$ is diagonal $\bar{a}_{ij} = \bar{a}_i \delta_{ij}$. In component notation the formal solution looks like

$$\bar{g}_{ij} = \bar{a}_i^{-1} \sum_l c_l \tilde{u}_{il} u_{lj} = \frac{1}{\lambda_i} \sum_l c_l \tilde{u}_{il} u_{lj} \quad \text{with} \quad \lambda_i = \omega - \varepsilon_i \tag{4.16}$$

The elements of the desired matrix G contain the eigenvalues λ_i of matrix A. They are identical to the diagonal elements of $\bar{A}$. Furthermore, the inhomogeneity C and the transformation matrix U are included. The poles ε_i of the Green's function determine the energy of the excitations.

The Green's function matrix $\langle\langle b_l ; b_n^\dagger \rangle\rangle_\omega$ and the correlation function $\langle b_n^\dagger b_l \rangle$ are connected by the spectral theorem. The corresponding spectral function $I_{lk}(\omega)$ is determined by the shift of the arguments of the Green's function into the complex plane.

$$\bar{I}_{b_i^\dagger b_j}(\omega) = \lim_{\delta \to 0^+} \frac{i}{e^{\beta\omega} - 1} \left[\bar{g}_{ij}(\omega + i\delta) - \bar{g}_{ij}(\omega - i\delta) \right] \tag{4.17}$$

The special form of the eigenvalues λ_i enables the application of the Dirac formula. A subsequent unitary transformation yields

$$I_{b_l^\dagger b_k} = \frac{2\pi c_k}{e^{\beta\omega} - 1} \sum_i u_{li} \tilde{u}_{ik} \delta(\omega - \varepsilon_i) . \tag{4.18}$$

The correlation function $\langle b_l^\dagger b_k \rangle$ is connected to the spectral density function by the spectral theorem (Section 2.4).

$$\left\langle b_l^\dagger b_k \right\rangle = \int \frac{d\omega}{2\pi} I_{b_l^\dagger b_k}(\omega) e^{i\omega(t-t')} \tag{4.19}$$

for equal times $(t = t')$ and sites $(l = k)$ yields the polarization

$$\langle \sigma_l \rangle = \frac{1}{2} \left(1 + 2 \sum_i \frac{u_{li} \tilde{u}_{il}}{e^{\beta \varepsilon_i} - 1} \right)^{-1} \tag{4.20}$$

The relation $\langle \sigma_l \rangle = \frac{1}{2} - \langle b_l^\dagger b_l \rangle$ yields the desired polarization in the rotated coordinate system. Appropriate numerical methods has to be applied to solve Eq. (4.20). A lattice with N sites requires the same number of eigenvectors $u_l = (u_1, u_2, \ldots, u_N)_l$. The eigenvalues $\varepsilon_i (\langle \sigma_1 \rangle, \langle \sigma_2 \rangle, \ldots, \langle \sigma_N \rangle)$ depend in general on the polarization of the other lattice sites with $c_l = 2 \langle \sigma_l \rangle$. The summation in Eq. (4.20) is carried out over the lth component of all eigenvectors u_i.

The rotation angle θ_l is given by

$$\langle [b_l, H]_- \rangle = \langle \sigma_l \rangle \left(2\Omega \cos \theta_l - 2\mu E \sin \theta_l - \sin \theta_l \sum_i J_{il} \cos \theta_i \langle \sigma_i \rangle \right) = 0 , \tag{4.21}$$

which ensures the minimization of the free energy and leads to

$$\tan \theta_l = \frac{2\Omega_l}{\sum_i \tilde{J}_{il} \cos \theta_i \langle \sigma_i \rangle + 2\mu E} . \tag{4.22}$$

This relation is valid both above $(\theta = \pi/2)$ and below the phase transition temperature T_c. Whereas in bulk material the energy can be represented in a closed form after Fourier transformation, in spherical nanoparticles one has to solve the coupled set of Eq. (4.13). For the calculation of the averaged polarization in the unrotated coordinate system the substitution $\langle \sigma_l \rangle \to \langle \sigma_l \rangle \cos \theta_l$ has to be made.

The poles of the Green's function give the transverse excitation energies. Within the applied RPA the leading part of the transverse spin-wave energy ε_n, the soft-mode energy of the n-th shell, is obtained from

$$\varepsilon_n = 2\Omega_n \sin \theta_n + \sum_j \tilde{J}_{nj} \cos \theta_n \cos \theta_j \langle \sigma_j \rangle + 2\mu E \cos \theta_n , \tag{4.23}$$

where average of the number of sites in any of the shells N_n is included in $\tilde{J}$ and all quantities are defined in the rotated frame. The shell-resolved relative polarization $\langle \sigma_n \rangle$ for the n-th shell in the rotated frame the polarization, taking only the diagonal term of (4.13) into account, reads:

$$\sigma_n = \frac{1}{2} \tanh \frac{\varepsilon_n}{2T}. \tag{4.24}$$

Here ε_n is the transverse excitation energy, i. e. the soft-mode energy of the n-th shell. The interaction energy $\tilde{J}_{ni}$ is determined by the interaction within each shell and the averaged number of nearest neighbors.

Using the same decoupling scheme as for bulk materials (Section 2.6.1) the damping of the pseudo-spin wave is calculated as

$$\gamma_n = \frac{\pi}{4} \sum_j \tilde{J}_{nj}^2 (\cos\theta_n \cos\theta_j - 0.5\sin\theta_n \sin\theta_j)^2 \bar{n}_j (1 - \bar{n}_j) \delta(\omega_n - \omega_j + \omega_j - \omega_n), \quad (4.25)$$

where $\bar{n}_n = \langle b_n^\dagger b_n \rangle$ is the correlation function. It is calculated via the spectral theorem and using the excitation energy in the RPA by Eq. (4.13).

4.4. Numerical results and discussion

4.4.1. Size and doping effects on the damping in ferroelectric thin films

The influence of defects within ferroelectric thin films is investigated by numerical calculations based on the theoretical results of Section 4.2 and is published in [130]. The following model parameters: $J_b = 495\,\text{K}$, $\Omega_b = 20\,\text{K}$ are taken into account. The temperature dependence of the damping $\gamma = \frac{1}{N}\sum_n \gamma_n$ is calculated for a simple cubic thin film ($\mathbf{k}_\parallel = \mathbf{0}$). Different values of the exchange interaction constants are considered. The numerical results expose some interesting and novel characteristics in the damping values in comparison to the case of FE thin films without defects.
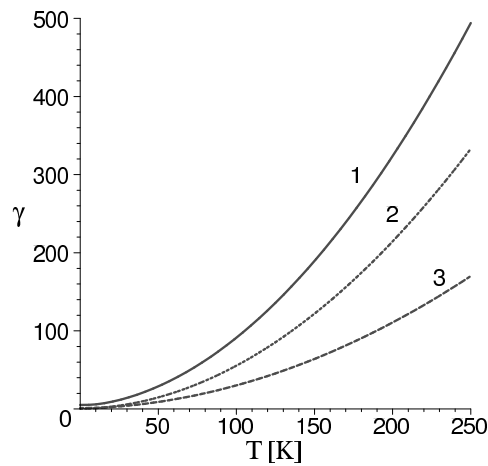

Fig. 4.3.: Temperature dependence of the damping γ in cm^{-1} for a FE thin film with seven layers and $J_b = 495\,\text{K}$, $\Omega_b = 20\,\text{K}$, $J_s = 900\,\text{K}$ $\Omega_s = \Omega_b$ in presence of one defect layer. Three different coupling strengths J_d are plotted. (1) $J_d = 300\,\text{K}$; (2) $1000\,\text{K}$; (3) $495\,\text{K}$

The temperature dependence of the damping of a seven layer thick ferroelectric film is shown in Fig. 4.3. The film has a defect layer in the middle, as in Fig. 4.1. The influence of this defect layer is compared to a defect free film (dashed line). Among the perfect thin film two opposite cases are possible. The first case (solid line) regards a weakening of the interaction energy in the defect layer compared to the bulk. The second kind of thin films possesses the opposite interaction strength J_d. The modification of the interaction strength J within the layers is originated by defects. Vacancies or impurities have different radius and distances compared to the constituent ions. Thus the interaction, denoted as J_d, changes to another value than the bulk interaction constant J_b. In all cases the damping increases with rising temperature in presence of any kind of defect. Experimentally an increase of the damping is observed in presence of defects. The results could help to explain the observed experimental results of Raman scattering from

Tab. 4.1.: Critical temperature for different defects

J_d [K]	bulk	300	1000
T_c [K]	219.5	213.8	228.5

ferroelectric thin films. The line shapes of the film become broad as the temperatures approaches T_c [133–135]. This is equivalent to a larger damping of the excitation within the material shown in Fig. 4.3.

Another important quantity is the critical temperature of thin films. Different kinds of defects have a remarkable influence on the phase transition temperature (Tab. 4.1). The Curie temperatures are obtained from Eq. (4.7) by solving $\sigma(T_c) = 0$. The critical temperature decreases in case of smaller J_d due to the smaller interaction between the constituent ions in comparison to the bulk value without defects. The decrease in the phase transition temperature by the substitution of impurities was found experimentally. Strontium (Sr)-doping of $Ba_{0.77}Ca_{0.23}TiO_3$ ceramics [136] causes a drastic decrease of the Curie temperature, just such as Sr-doping of pure BTO ceramics, demonstrating a cell volume effect. La-modified PTO obeys a significant lowering of T_c with an increase of La content [137]. The transition temperature of undoped lead zirconate titanate (PZT) film was found to be reduced with Nd-doping of sol-gel derived $Pb_{1.05}(Zr_{0.53}Ti_{0.47})O_3$ thin films [138]. The decrease of the critical temperature in thin ferroelectric films can be associated with the substitution of La in bismuth layer-structured ferroelectrics (BLSF) [139]. The La atoms substitute for Bi atoms in a perovskite-type unit only, and the substitution causes less distortion of the structure, resulting in smaller spontaneous polarization and lower ferroelectric Curie temperature. Electronic-structure calculations revealed that covalent interaction, which originates from the strong hybridization between Ti $3d$ and O $2p$ orbitals, plays an important role in the structural distortion and ferroelectricity of the materials. Barium strontium titanate (BST) ceramics doped with low Mg concentrations [140] exhibit a shift of Curie point to lower temperatures. Mg mainly acts as an acceptor dopant to replace Ti at the B site of ABO_3 perovskite structures. In $Ba_{1-x}Ca_xTiO_3$ thin films [141] a lower transition temperature was found with an increase in the values of Ca. The anomalous phase transition decrease was ascribed to the occupancy of the Ca^{2+} in the Ti^{4+} site.

The opposite behavior of T_c is found in films with enhanced J_d. Here the phase transition occurs at larger values. Investigations for Sr-deficient and Bi-excess strontium bismuth tantalate (SBT) [142, 143] show that excess-Bi is substituted at the perovskite A site (Sr site) as trivalent ions. Here, ferroelectricity is attributed to the rotation and tilting of TaO_6 octahedra as well as the displacement of Ta ions in the octahedra. Hence

the A-site ions located at the cavities between two TaO_6 octahedra play a crucial role in the ferroelectric properties. The charge neutrality in the crystal is satisfied through the introduction of cation vacancies at the A-site. The substitution of Bi with the A-site vacancies led to a marked increase in Curie temperature. The structure refinement revealed that the rotation of TaO_6 octahedra in the a-b plane accompanied with the whole shift of the octahedra along the a-axis is largely enhanced by the Bi substitution with A-site vacancies, which is responsible for the higher T_c. In a series of Bi-layered compounds [144] the lattice mismatch between TaO_2 and AO planes in the perovskite-type unit of ATa_2O_7 increases and the structural distortion becomes more pronounced, as the size of the A-site cation decreases from Ba^{2+} to Ca^{2+}. This distortion leads to the higher Curie temperature. The dielectric and ferroelectric properties of barium strontium titanate (BST) $Ba_{1-x}Sr_xTiO_3$ and Ca-doped barium strontium titanate (BSCT) $Ba_{1-2x}Sr_xCa_xTiO_3$ ceramics have been investigated [145]. Introducing Ca^{2+} ions into BST ceramics decreases obviously the dielectric constant maximum. The T_m of BST ceramics shifts to higher temperature when Sr^{2+} ions are substituted with Ca^{2+} ions in BST ceramics. The effects of Ca doping on the Curie temperature of $Ba_{0.4}Sr_{0.6-x}Ca_xTiO_3$ has been studied [146]. Powder x-ray diffraction revealed a small amount of Ca ions substituted for Ti ions. Correlated with the evolution of the lattice constant with x, T_c increases linearly with increasing calcium concentrations. These variations have been interpreted in terms of Ca-doping-induced A-site cation size variance, a substitution of a small amount of Ca ions for Ti ions, and structural phase separation. Hence, the critical temperatures of the FE phase transition are increased or decreased due to different interactions in the defect layers.
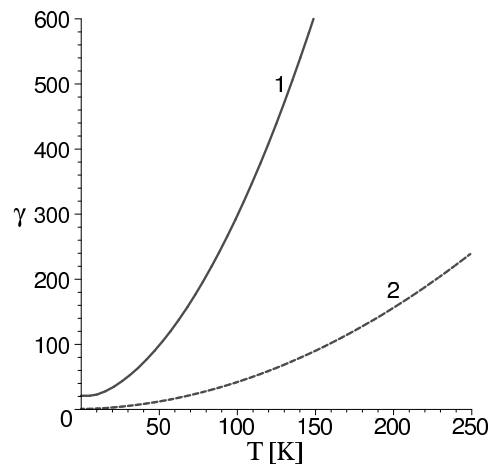

Fig. 4.4.: Temperature dependence of the damping γ in cm^{-1} for $J_b = 495\,K$, $\Omega_b = 20\,K$, $J_s = 300\,K$, $\Omega_s = \Omega_b$, $N = 7$ in presence of a varying number of defect layers. (1) $J_3 = J_4 = J_5 = J_d = 600\,K$; (2) $J_4 = J_d = 600\,K$

The damping is influenced by the number of inner defect layers. The variation of the inverse life-time with the number of defect layers is depicted in Fig. 4.4. A thin film of seven layers with three defect layers (solid line) ($J_3 = J_4 = J_5 = J_d = 600$ K) exhibits a larger damping than a film with only one defect layer (dashed line) ($J_4 = J_d = 600$ K). The line broadening in scattering experiments should be enlarged over the whole temperature range. This is in agreement with the experimental data [147], where structural defects can produce excessive line broadening.
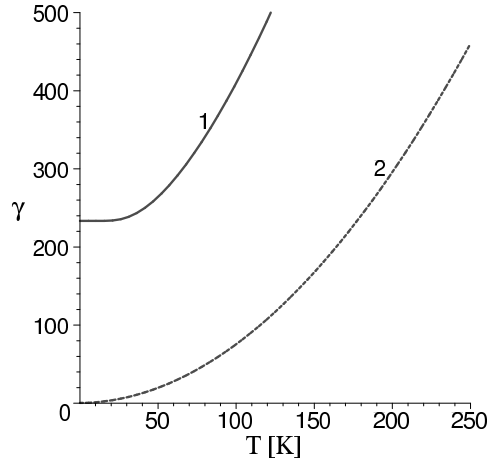

Fig. 4.5.: Temperature dependence of the damping γ in cm^{-1} for $J_b = 495$ K, $\Omega_b = 20$ K, $J_s = 300$ K, $\Omega_s = \Omega_b$ and different film thickness. (1) $N = 7$; (2) $N = 9$

The size dependence of the ferroelectric thin film is given in Fig. 4.5. Two different film sizes are compared. The middle layer is defect ($J_d = 1000$ K). The damping increases for higher temperatures in both cases, films with seven (solid line) and nine layers (dashed line). The thinner film shows a higher damping for all temperatures. Hence the damping increases with decreasing film thickness. The thinner the films the larger is the damping. The enlarged damping of the excitation for thinner films is in agreement with previous calculations without defects [123] and with the experimental data [133–135].

4.4.2. Surface and size effects in spherical ferroelectric nanoparticles

4.4.2.1. Macroscopic properties without external electric fields

The existence of a surface in non-bulk systems, such as small particles, changes all physical quantities. The number of nearest neighbors at the surface differs from the inner part. Hence, the appearing strain in the surface of ferroelectric nanoparticles results in a change of the interaction constant J at the surface in the framework of the Ising model in a transverse field given in Chapter 4.1. These surface effects, represented by a deviation of the interaction $J_s \neq J_b$, compared to the inner shells, influence all relevant quantities based on the theoretical description of ferroelectric nanoparticles. The analytical expressions in form of coupled equations (Eq. (4.13) and Eq. (4.20)) were numerically solved for different sets of parameters, adequate for the modeled particles. In particular, the behavior of spherical ferroelectric (FE) particles, whose cross section is depicted in Fig. 4.6, is analyzed. It should be noted that the relevant parameter is the ratio Ω/J, which is in general a small quantity. The results presented in this part of the thesis are published in [148, 149]. Moreover the phase transition temperature is strongly
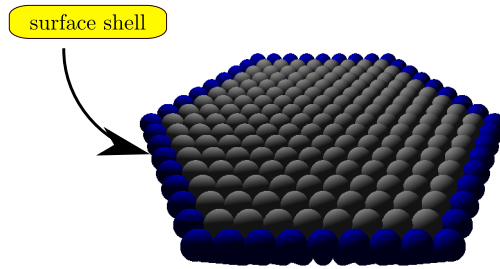

Fig. 4.6.: Schematic cross section of a ferroelectric nanoparticle with eight shells. The blue color indicates the surface shell.

influenced by a variation of J. Thus different interaction strengths are considered while the transverse field remains fixed. The required interaction parameter for the non-surface and non-doped case were chosen due to former calculations for BTO systems [4]. The interaction strength reads $J_b = 150\,\mathrm{K}$, the tunneling integral is $\Omega_b = 10\,\mathrm{K}$.

The size dependence of the polarization and the critical temperature of ferroelectric nanoparticles are investigated. The size of the nanoparticles, composed of shells, is controlled by the number of shells N. In the outermost shell – the surface shell – the interaction strength is smaller compared to the inner shells. This seems to be appropriate for BTO ferroelectric particles. The temperature dependence of the polarization of

ferroelectric particles of different size is shown in Fig. 4.7(a). The polarization decreases with increasing temperature for all particle sizes and vanishes continuously at a size dependent critical temperature. The polarization at a certain temperature is enhanced with increasing particle size. A doubling of the particle size for the smallest particles shows the largest change in the polarization. For larger particles, after doubling the particle size, a minor change is observed. The corresponding dependence of the critical temperature on the particle size is shown in Fig. 4.7(b). The ferroelectric particles exhibit a fast increase of the critical temperature T_c with an ascending number of shells. In the limit of very large numbers N the critical temperature approaches a constant value.
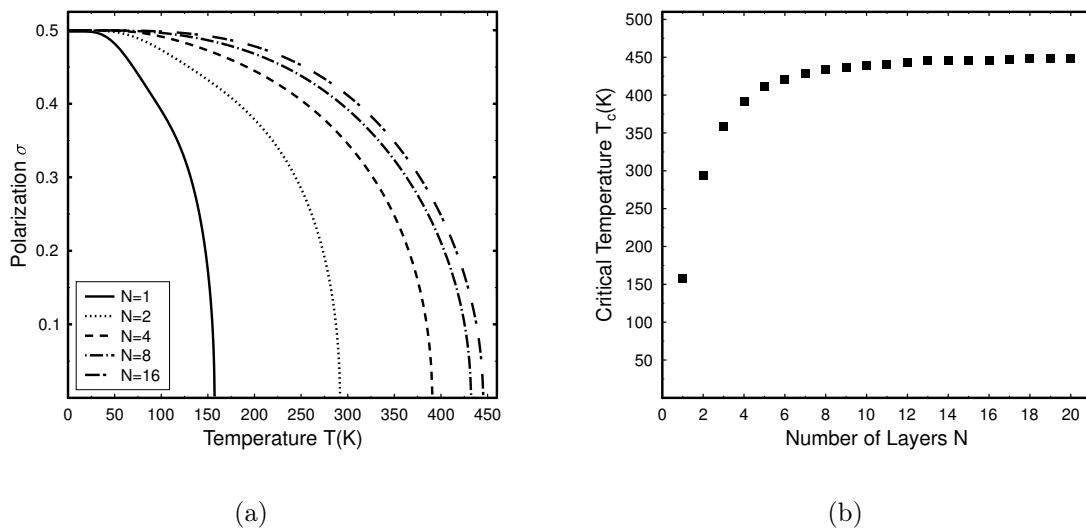

(a)   (b)

Fig. 4.7.: Temperature dependence of the polarization (a) and the critical temperature (b) depending on the number of shells N. The interaction strengths are fixed to $J_b = 150\,\mathrm{K}$ and $J_s = 50\,\mathrm{K}$.

The influence of the surface is dominant for small particles. The changed configuration of the surface shows the largest effect for small particles. With increasing particle size, the influence of the surface is reduced. Hence the polarization shows only small deviations from the bulk value for larger particles. The increase of the critical temperature is in qualitative agreement with the X-ray diffraction (XRD) analysis of small particles composed of BTO [150] showing a smaller transition temperature with a decrease in the particle size. Specific heat measurements and differential scanning calorimetry (DSC) on PTO nanoparticles reveal, that the transition temperature decreases gradually with a decrease of the particle size [151, 152].

The associated critical size effect is controversially discussed in the literature [153, 154]. The question arises, how physical properties such as the polarization or the critical temperature are affected by the size of the system, especially in the nanometer scale and

if there is a maximal size of a crystal at which ferroelectricity is impossible. The chosen set of parameters does not lead to an indication for a pronounced critical size effect.

Tensile or compressive strain results in a reduced or enhanced interaction at the surface. The effect of the surface interaction on the temperature dependent mean polarization is shown in Fig. 4.8. Three particles with different surface configurations are considered. The particles have the same size, i.e. the same number of shells N. The particle is build up of four shells as in Fig. 4.2(d). Due to the different numbers of nearest neighbors or by the resulting strain of small particles at the surface the interaction constant at the surface J_s is generally different compared to J_b in the bulk.
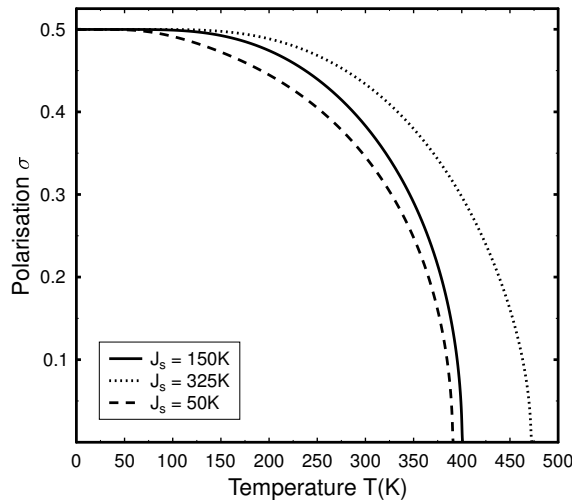

Fig. 4.8.: Temperature dependence of the averaged polarization σ with $J_b = 150\,\text{K}$, $N = 4$ for different surface couplings: $J_s = J_b$ (solid curve); $J_s = 325\,\text{K}$ (dotted curve); $J_s = 50\,\text{K}$ (dashed curve).

The polarization for a higher (dotted line) as well as a lower (dashed line) interaction in the surface shell is investigated. The variation of the coupling at the surface changes the polarization. A lowered surface interaction strength ($J_s < J_b$) leads to a reduced polarization, which vanishes continuously at a lower critical temperature T_c. The opposite case ($J_s > J_b$) yields a larger dipole moment and consequently an enhanced phase transition temperature T_c. The phase transition is a pronounced second-order one. The observation reflects that both the bulk and the surface coupling contribute to the ordering of the pseudo-spins. A reduced surface interaction could explain the decrease of the polarization and the phase transition temperature in small particles of BTO [150, 155] and PTO [151, 152]. The enhanced surface interaction is responsible for the increase of the polarization and critical temperature in small KDP particles [156] and KNO$_3$ thin films [157].

The effect of the surface interaction on the polarization is investigated in more detail by the shell-resolved polarization σ_n with a reduced surface interaction in Fig. 4.9(a). The particle, see Fig. 4.6, is composed of eight shells ($N = 8$). The index n denotes the considered shell of the particle, e.g. $n = 8$ represents the surface shell. The opposite case, an enhanced interaction, is regarded in Fig. 4.9(b). A reduction or enhancement of the
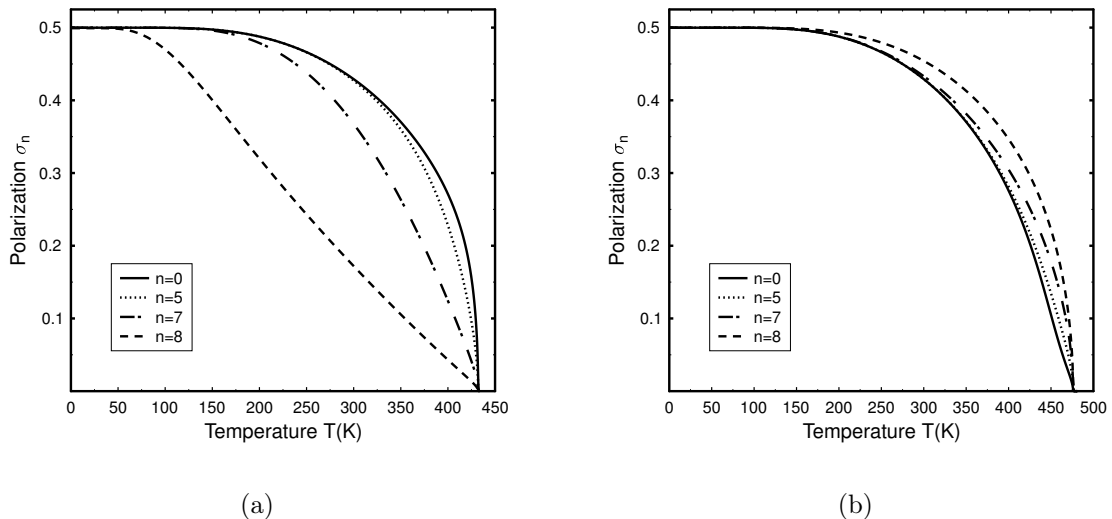

(a)   (b)

Fig. 4.9.: Temperature dependence of the shell resolved polarization σ_n for a particle with eight shells. The surface energy is $J_s = 50\,\text{K}$ (a) and $J_s = 325\,\text{K}$ (b). The non-surface interaction $J_b = 150\,\text{K}$ is fixed.

local polarization σ_n depending on the shell within the particle is clearly visible. The behavior is contrary for weaker or stronger surface couplings. The polarization is almost not affected at very low temperatures. With increasing temperature the polarization differs depending on the shell. Shells closer to the surface shell are more affected than inner shells. This reflects the importance of the inclusion of surface effects.

4.4.2.2. Hysteresis effects

The inclusion of an electric field and the theoretical observation of the influence of the surface configuration on the associated hysteresis loop is shown in Fig. 4.10. Three different surface configurations ($J_s < J_b$, $J_s > J_b$ and $J_s = J_b$) are considered for a particle with eight shells ($N = 8$) at room temperature ($T = 300\,\text{K}$). A reference curve (solid line) is drawn for a particle without a change in the surface. The coercive field E_c and the remanent polarization σ_r are sensitive to variations of the interaction parameter at the surface. In case that a surface coupling is smaller than in the inner shells (dashed line), both quantities are reduced. In the opposite case (dotted line) both, the coercive

field and the remanent polarization increase. The lowering of the coercive field is related to the reduction of the critical temperature (Fig. 4.8) caused by the changed surface configuration. This was observed in small BTO- [155] and PTO particles [152]. The opposite case agrees with observations made in small KDP- particles [156], where the polarization and the critical temperature increase compared to the bulk material. The hysteresis loops obtained with the microscopic model are in agreement with the results based on a thermodynamic approach [158]. Here, surface effects are described by an inhomogeneous Landau-Devonshire theory.
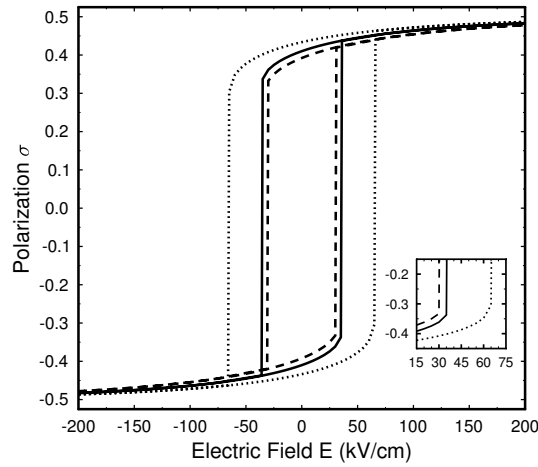

Fig. 4.10.: Influence of the surface coupling strength J_s on the hysteresis of a particle with eight shells at fixed temperature $T = 300\,\mathrm{K}$ for $J_s = 150\,\mathrm{K}$ (solid curve), $J_s = 350\,\mathrm{K}$ (dotted curve), $J_s = 50\,\mathrm{K}$ (dashed curve); the insert offers the low field behavior. The interaction of the inner shells reads $J_b = 150\,\mathrm{K}$.

The temperature dependence of the hysteresis loop for a particle with eight shells is shown in Fig. 4.11. At very low temperatures (solid line), the remanent polarization σ_r is at its maximum value. The coercive field E_c is large compared to higher temperatures. The hysteresis loop narrows with rising temperature (dotted line). Hence, the coercive field E_c and the remanent polarization decrease with increasing temperature. At temperatures above the phase transition temperature (dashed line) the particle shows no hysteresis. Due to the increasing influence of temperature effects, e.g. fluctuations, the coercive field and the remanent polarization are reduced. In the paraelectric phase the hysteresis loop vanishes (dashed line), due to the loss of spontaneous ordering of the order parameter.

Fig. 4.12 reflects the size dependence of the remanent polarization (filled circles) and the coercive field (filled squares) at room temperature. Both, the field E_c and the polarization σ_r, increase with increasing size of the nanoparticles. The influence of
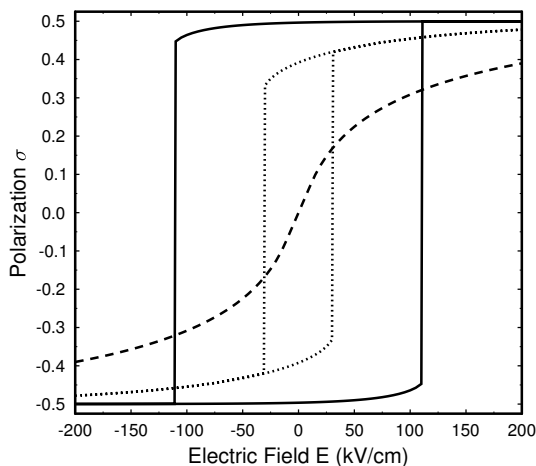
Fig. 4.11.: Temperature dependence of the hysteresis with $J_s = 50\,\text{K}$: $T = 100\,\text{K}$ (solid curve), $T = 300\,\text{K}$ (dotted curve), $T = 500\,\text{K}$ (dashed curve). The particle consists of eight shells ($N = 8$) and a non-surface interaction of $J_b = 150\,\text{K}$.

the surface diminishes for larger particles. Theoretical findings by a continuum phase field model [159] and the experimental data from ultrathin ferroelectric films of BTO [160] agree with the obtained results. Within this approach no rising coercive field with decreasing particle size is observed, as reported in [161–163].

4.4.2.3. Microscopic properties

Apart from macroscopic quantities the Green's function method yields microscopic properties of the nanoparticles as the energy of the elementary excitations, compare Eq. (4.13), Eq. (4.23), and its damping, see Eq. (4.25).

The dependence of the excitation energy on the temperature for ferroelectric nanoparticles of different sizes is shown in Fig. 4.13(a) for a reduced surface interaction ($J_s < J_b$). For all particle sizes the excitation energy lowers with increasing temperatures and vanishes at the critical temperature. Larger particles have larger energies over the complete temperature range. The gain of energy for particles upon the doubling of size is smaller, if the particles become larger. The nanoparticle shows a typical soft-mode behavior as already observed in the bulk material [103]. The excitation energy is shifted to smaller values in comparison to the bulk material, when the number of shells decreases. Due to higher order interactions between the constituents, the scattering at defects or by the inclusion of phonon degrees of freedom, the elementary excitation can be damped. Such a damping (Eq. (4.25)) results in a finite life-time of the excitations. The temperature
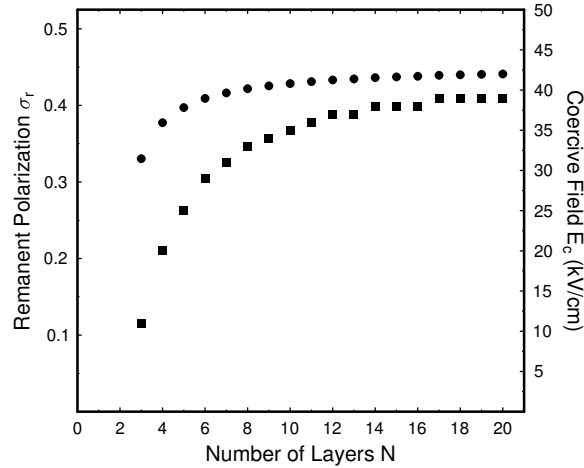
Fig. 4.12.: Remanent polarization σ_r (circles) and coercive field E_c (squares) for different size N at temperature $T = 300$ K and couplings $J_b = 150$ K, $J_s = 50$ K.

dependence of the damping of the pseudo-spin excitations for particles of different size is given in Fig. 4.13(b). The damping increases for higher temperatures for all particles. At low temperatures the damping is extremely small, thus the excitations are underdamped. In approaching the critical temperature the damping increases strongly but remains finite. Smaller particles exhibit larger damping of the excitations. The change in damping is the largest for the smallest particles. The insert shows the overall development of the damping. Very close to the critical point a sudden decrease was observed, which is plotted in the insert only for the sake of completeness. Fluctuation effects, predominantly occurring in the vicinity of the phase transition, are slightly suppressed through the selected approximation. Hence, results near the critical temperature should be considered as an extrapolation. A lower excitation energy for smaller particles implies a lowering of the force constant, which was observed for PTO particles [135, 151, 164]. Consequently this leads to the decrease of the phase transition temperature between the tetragonal and the cubic phase.

The finite damping at the phase transition point is in contrast to the behavior of bulk material, e.g. PTO [165], where the linewidth of the soft mode diverges at the ferroelectric-to-paraelectric transition. The soft mode becomes overdamped close to the phase transition. Such a behavior is in agreement with experimental data for PTO [135, 164], BTO [166] and SBT [167] particles. The enhanced damping in small nanoparticles offers an explanation of the broadened peak, observed in the dielectric constant of PTO particles [152] and (Ba,Sr)TiO$_3$ thin films [168, 169]. A broadened dielectric anomaly
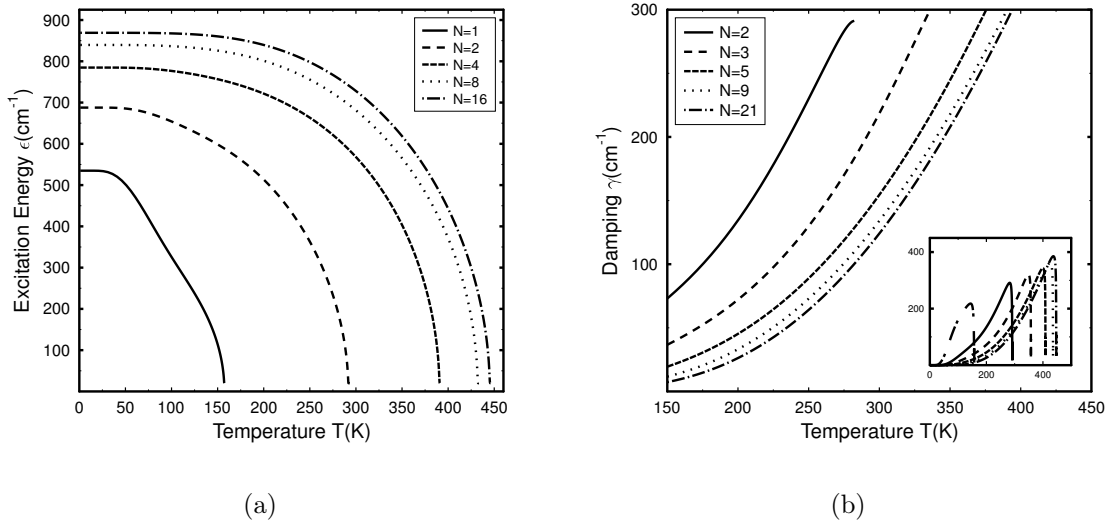
(a)   (b)

Fig. 4.13.: Temperature dependence of the excitation energy (a) and the related damping (b) for for particles of different size N with $J_b = 150\,\mathrm{K}$, $J_s = 50\,\mathrm{K}$.

leads also to a smearing out of the critical regime.

4.4.3. Doping effects in spherical ferroelectric nanoparticles

4.4.3.1. Macroscopic properties without external electric fields

Experiments show a clear influence of impurities or defects on physical properties. Such defects can be originated by localized vacancies or impurities, doping ions with smaller radii and larger distances in-between in comparison to the host material, see also [159]. The variation of the coupling parameter can also originate from the appearance of local strain. The simplest way to incorporate defect configurations into the model is to assume a variation of the interaction strength J. Microscopically, the substitution of defects into the material leads to a change of the coupling parameter. The defect coupling between neighbors is altered $J = J_d$ and in general different from the surface value J_s as well as the bulk one J_b. Furthermore, the defect can be situated at one or more shells within the nanoparticle (Fig. 4.14). The corresponding transverse field in a defect shell Ω_d should also change. The investigations are focused on the quantity Ω_d/J_d. Hence the quantity Ω_d is kept fixed and only the interaction within the defect layer is varied. The polarization, excitation energy as well as its damping should depend on the defect concentration. The presented results are published in [148, 170].
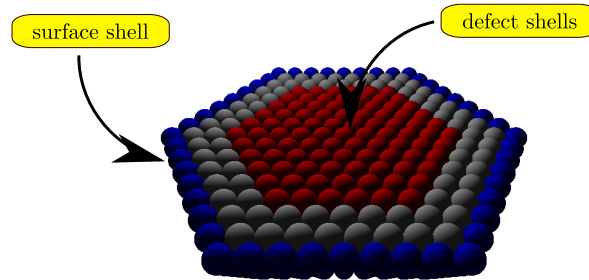

Fig. 4.14.: Schematic cross section of a defect ferroelectric nanoparticle with eight shells. The blue color indicates the surface shell and the red color the five shells being defect.

The temperature dependence of the polarization of ferroelectric nanoparticles with defects is shown in Fig. 4.15. The particle consists of eight shells with the first two shells being defect. The polarization of the nanoparticle decreases with increasing temperature and vanishes at T_c. Apparently the Curie temperature changes due to the presence of defects. The temperature dependence deviates from the defect free case. The weakening of the interaction parameter ($J_d < J_b$) by defects (dashed curve) reduces the spontaneous polarization and the critical temperature compared to particles without defects (solid curve) over almost the whole temperature range. Only at very low temperatures the
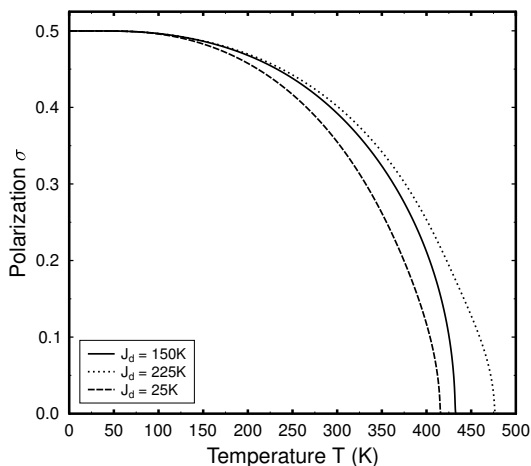
Fig. 4.15.: Temperature dependence of the averaged polarization σ for a ferroelectric nanoparticle with $J_b = 150\,\text{K}$, $J_s = 50\,\text{K}$. From the total number of $N = 8$ shells the first two shells are defect shells: $J_d = J_b$ (solid curve); $J_d = 225\,\text{K}$ (dotted curve); $J_d = 25\,\text{K}$ (dashed curve)

polarization is not affected. In case of a higher interaction ($J_d > J_b$) the polarization (dotted curve) as well as the critical temperature are enlarged.

For a more detailed investigation of the influence of defects on the polarization and the critical temperature, the concentration of defects of different type within the nanoparticle is altered. The concentration of defects is included by the number of shells with a modified interaction J_d. The dependence of the averaged polarization σ of spherical nanoparticles on the number of defect shells n_d at a fixed temperature ($T = 300\,\text{K}$) is shown in Fig. 4.16(a). The particle consists of eight shells. Two different types of defects within the nanoparticle are considered. A defect coupling smaller than the bulk and surface couplings (squares) leads to a reduction of the polarization. Higher defect strengths (diamonds) enlarge the polarization. A secondary effect can be observed by considering the sequence of the defect shells. The full symbols correspond to the case, when the defect configuration starts at the center and subsequently the next shells are assumed to be defect configurations. The procedure is performed until the surface shell is reached and becomes itself defect, too. The opposite realization is drawn as open symbols. Here, firstly the configuration of the surface shell is a defect configuration and then subsequently the other shells become defect until the center is reached. The two different realizations are denoted as up- and down-process, respectively. The up-process represents a filling procedure starting from the center of the nanoparticle and down-process for the opposite direction. The interaction with the pseudo-spin in the center of the particle
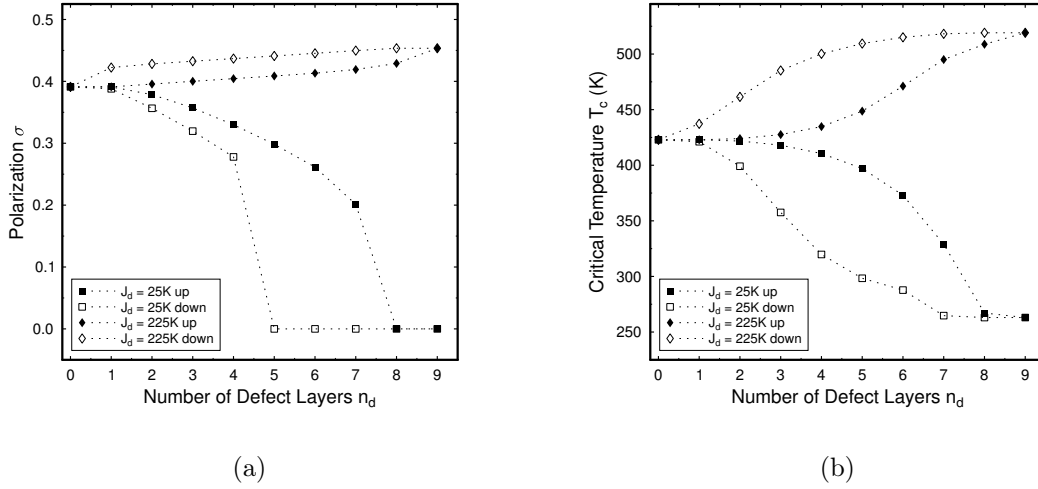
69

(a)   (b)

Fig. 4.16.: Dependence of the averaged polarization and the critical temperature on the number of defect shells $n = n_d$ for a particle size $N = 8$. The interaction strength reads $J_b = 150\,\mathrm{K}$, $J_s = 50\,\mathrm{K}$ and two different J_d-values: $J_d = 25\,\mathrm{K}$ (squares) and $J_d = 225\,\mathrm{K}$ (diamonds) were chosen. The full symbols denote the up process, the open symbols - the down process, see the text.

is indicated by $n_d = 1$ in the up-process. In the down-process the first shell becoming defect is the surface shell. Here, a larger influence on the polarization is observable. Both processes have in common the increase or decrease of polarization with the growing number of defect shells for the particular interaction strength. The slope is stronger for the down-process than for the up-process. In case of a reduced interaction strength within the defect shell, the polarization of the particle vanishes. This corresponds to a decrease of the critical temperature, see also Fig. 4.16(b). Above a certain defect concentration, corresponding to the number of defect shells, the particle becomes paraelectric at the fixed temperature.

The influence of defects on the Curie temperature is shown in Fig. 4.16(b). A defect coupling smaller than bulk and surface couplings (squares) decreases the critical temperature, whereas higher defect strengths (diamonds) enlarge the phase transition temperature. The critical temperature is also influenced, by the up- or down process, which was particularly described for the dependence of the polarization on the kind of defect in the nanoparticle. The full squares and diamonds correspond to the case, where the sequence of defects starts at the center. Both defect growth directions show a increase or decrease of T_c with the increasing number of defect shells for the particular interaction strength. For the down-process the slope is stronger than for the up-process.

Both responses to the doping ($J_d < J_b$, $J_d > J_b$) were experimentally observed. For

Sr-deficient and Bi-excess SBT the Bi substitution with A-site vacancies is responsible for the enhanced polarization and Curie temperature [142, 171], governed by the bonding characteristics with oxide ions. The influence of the orbital hybridization on T_c is very large, and Bi substitution results in a higher transition temperature. A decrease in the polarization and the Curie temperature was found in lanthanum-doped lead zirconate titanate (PLZT) for the increase of Ba [172] and La concentrations [173]. This effect in ABO_3 structures is addressed to induced A-site vacancies, which weaken the coupling between neighboring BO_6 octahedral [137]. The Curie point shifts to lower temperatures in barium zirconium titanate (BZT) nanoparticles [150].

4.4.3.2. Hysteresis effects

Several indications for a significant influence of doping effects on the hysteresis loop of ferroelectric nanostructures are observed in experiments. The behavior of the remanent polarization as well as the coercive field are influenced by the presence of defects.

This influence of defects on the hysteresis loop represented by two different coupling strengths J_d is shown in Fig. 4.17. The first five inner shells of the nanoparticle consist of defects. Here the number of ferroelectric constituents is large enough to give a significant contribution to the polarization and consequently, also to the hysteresis loop. The area of the hysteresis loop changes due to the presence of defects. In case of a reduced
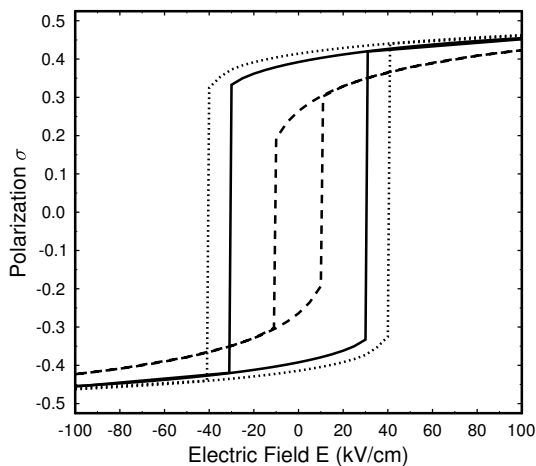

Fig. 4.17.: Influence of defects on the hysteresis for $T = 300\,\text{K}$, $J_b = 150\,\text{K}$, $J_s = 50\,\text{K}$. The first five of totally eight shells ($N = 8$) are defect: $J_d = J_b$ (solid curve); $J_d = 225\,\text{K}$ (dotted curve); $J_d = 25\,\text{K}$ (dashed curve).

interaction strength in the defect shells (dashed curve) the coercive field and the remanent

polarization are reduced in comparison to the defect-free case ($J_d = J_b$). The reduction of the interaction strength ($J_d < J_b$) and the accompanied decrease of the coercive field and the remanent polarization in small ferroelectric particles by the substitution of doping ions could explain the experimental observations of substituting La in PTO thin films [174] and PZT [173, 175] nanopowders. The hysteresis loop for an enhanced coupling ($J_d > J_b$) (dotted curve) exhibits an enhanced coercive field and remanent polarization compared to the non-defect particles. A defect coupling stronger than the bulk coupling will be in general realized, when the impurities have a larger radius compared to the constituent ions. This can be originated by compressive stress. The corresponding quantities are enhanced in comparison to the bulk value, which is clearly originated by an enhanced J_d-coupling. The results are in accordance with the experimentally observed increase of E_c and P_r in case of substituting ions such as Bi in SBT [142], or by increasing the barium contents in PLZT ceramics [172].

The dependence of the coercive field on the defect concentration for two different kinds of defects is shown in Fig. 4.18. The particle has a size of eight shells. The temperature is fixed to room temperature ($T = 300$ K). The amount of defects within the particle is given by the number of shells n_d, which are defect. The position of defects in the nanoparticle is given by the growth direction of the defect, denoted as the up- and down-process described before. In case of defects leading to a reduced coupling in the
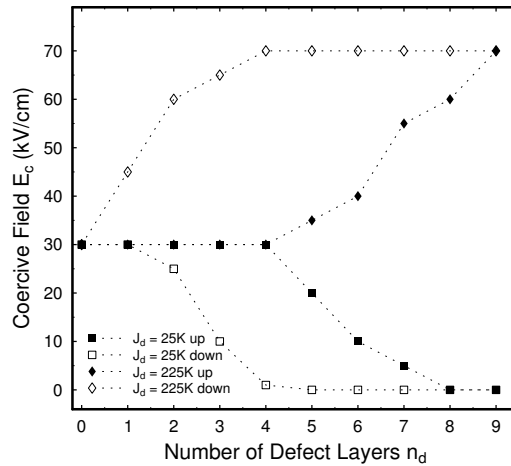

Fig. 4.18.: Dependence of the coercive field E_c on the number of defect shells n_d for $N = 8$, $J_b = 150$ K, $J_s = 50$ K and different J_d-values: $J_d = 25$ K (squares) and $J_d = 225$ K, (diamonds). The full symbols denote the up-process, the open symbols - the down-process.

defect shells (squares), the coercive field is reduced with increasing number of defect

shells. The position of the defects within the particle guides the slope of the reduction of the coercive field. Defects located in the outer shells lead to a stronger decrease of E_c. The coercive field equal to zero, if the number of defects in the particle becomes large enough to reduce the phase transition temperature below room temperature. The particle becomes paraelectric and the coercive field vanishes. The result is in reasonable accordance to the experimental data [173, 174, 176]. A similar result is also obtained for the remanent polarization P_r. An increase of the lanthanum content in PTO and PZT ceramics decreases the coercive field E_c.

Particles including defects with an enhanced coupling (diamonds) have larger coercive fields. With an increasing number of defect shells the coercive field E_c (respectively P_r) increases. The open squares and diamonds represent the filling of the particles with defect shells beginning from the surface shell (down-process), whereas the full symbols correspond to the up-process. One observes that the increase or decrease of E_c is more pronounced and stronger for the down-process. The enhanced coercive field is in a quite good agreement with the experimental data, by the doping of SBT with calcium (Ca) or neodymium (Nd), where oxide vacancies are produced by the substitution of Nd at the B-site. [171, 177].

4.4.3.3. Microscopic properties

The underlying microscopic properties of the nanoparticles, such as the energy of the elementary excitations (Eq. (4.23)) and its damping (Eq. (4.25)) are influenced by defects as well. The temperature regime of the energy of the elementary excitations ε for different numbers of defect shells n_d, is shown in Fig. 4.19(a). All up to the n_d-th shell are defect. This is equivalent to the up-process, if different filling procedures are taken into account. The bulk coupling is stronger than the defect and the surface coupling ($J_b > J_s > J_d$). Excitation energies depend on the number of defects n_d and the corresponding coupling J_d. An enhanced defect concentration reduces the energy of the excitations in the present choice of parameters for all temperatures up to the critical point. The corresponding behavior of the damping of excitations on the number of defect shells is shown in Fig. 4.19(b). The damping increases with rising temperature. When reaching the phase transition point the damping gets its maximum, but stays finite. The damping is enhanced in comparison to the non-defect case. The complete development of the damping is shown in the inset. The sudden drop of the damping at the critical point is suppressed in Fig. 4.19(b). The behavior in the vicinity of the phase transition is beyond the scope of the theory and has to be treated in the framework of a more refined theory (e.g. renormalization group theory). An experimental evidence of the lowering of the soft mode frequency for La-doped nanocrystalline PTO was given in [178]. Similar results are
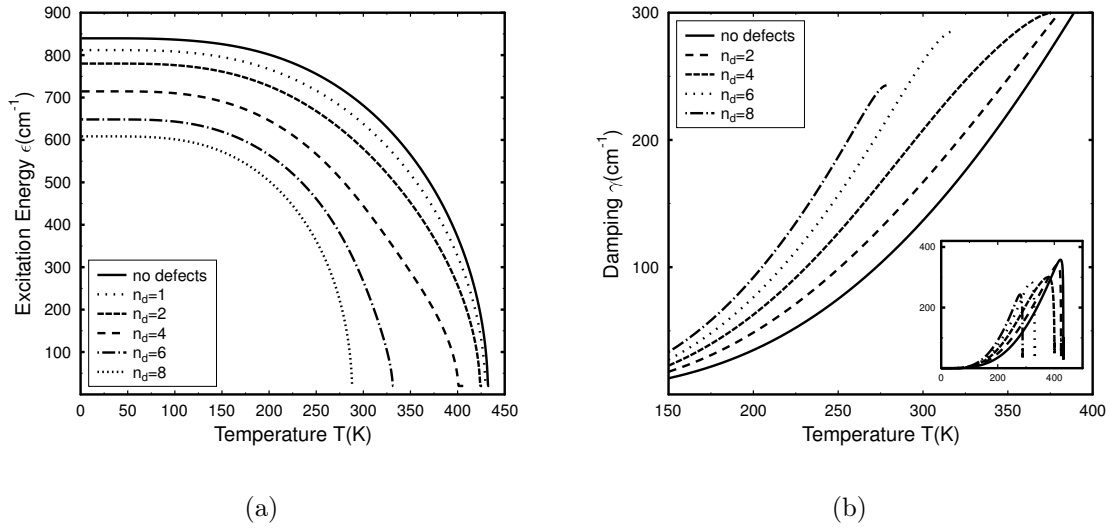
Fig. 4.19.: Temperature dependence of the (a) excitation energy and (b) damping for $J_b > J_s > J_d$ with different defect shells $J_b = 150\,\mathrm{K}$, $J_s = 50\,\mathrm{K}$, $J_d = 25\,\mathrm{K}$, $N = 8$.

found for Er-substituted PTO thin films [179]. The Raman peak width is broadened in comparison to undoped specimen. This is in accordance with a larger damping of the excited modes. The results reveal, that different mechanism such as surfaces, stress and defects contribute additively to the damping coefficient. In so far the damping is always enhanced in comparison to the bulk and to materials without defects.

5. Many-particle approach to non-collinear magnetic structures

5.1. The model and Green's function

In this section it is demonstrated, that a many-particle approach can be applied to non-collinear magnetic structures [180]. Therefore, an extended Heisenberg model is chosen to represent the underlying magnetic system. The isotropic Heisenberg model H_1 describes the coupling of the spins in the magnetic system and drives the parallel or anti-parallel alignment. The asymmetric DMI H_2 favors a canting of the spins in the plane perpendicular to the DM-vector $\mathbf{D}$. Because of the asymmetric superexchange interaction of the magnetic moments, the spins orient in a non-collinear fashion, which can be the origin of a spiral spin structure of several types. The Hamiltonian reads:

$$H = H_1 + H_2 + H_3 \tag{5.1}$$

where the three part are defined by:

$$H_1 = -\frac{1}{2} \sum_{ij} J_{ij} \mathbf{S}_i \mathbf{S}_j - g\mu_B \mathbf{H}^{\mathbf{A}} \sum_i \mathbf{S}_i \,, \tag{5.2a}$$

$$H_2 = -\frac{1}{2} \sum_{ij} \mathbf{D}_{ij} (\mathbf{S}_i \times \mathbf{S}_j) \tag{5.2b}$$

$$H_3 = -\frac{1}{2} \sum_{ij} J_{ij}^A S_i^\tau S_j^\tau \,. \tag{5.2c}$$

An anisotropy in a certain τ-direction is included by the third term H_3. In the upcoming calculations we will restricted ourself to $\tau = z$. In H_1 the summation is taken over all nearest neighbors and J_{ij} denotes the symmetric exchange interaction. The spin couples also to an anisotropy field $\mathbf{H}^{\mathbf{A}}$. The relativistic spin-orbit interaction reflected in the DMI H_2 is determined by the antisymmetric coupling $\mathbf{D}_{ij}$.

For the description of magnetic systems with a spiral structure, some special cases had been discussed in [181, 182], it is appropriate to transform the spin operators to the eigen representation of the quantization axis introduced in Section 2.2. Here, the quantization

axis, see Fig. 5.1, at site f of the lattice is given by the real unit vector

$$\boldsymbol{\gamma}_f = (\gamma_f^x, \gamma_f^y, \gamma_f^z) = (\rho \cos \mathbf{Q}\mathbf{r}_f, \rho \sin \mathbf{Q}\mathbf{r}_f, \gamma_f^z) \, . \tag{5.3}$$

The spin-$\frac{1}{2}$ operators are transformed in terms of Pauli operators $b^\dagger$ and b as described in Section 2.2.
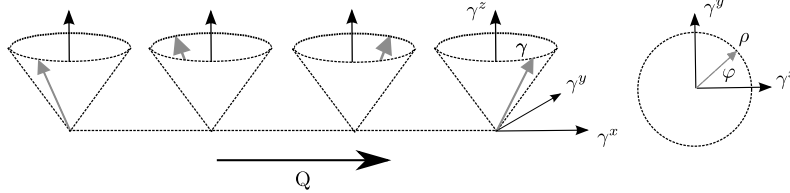

Fig. 5.1.: Quantization axis of transformed operators with $\rho = \sqrt{1 - (\gamma^\tau)^2}$.

This realization guaranties the commutator relation of the spin operators and the Hamiltonian is transformed into in the following compressed form, where only even terms in the annihilation and creation operators have to be taken into account

$$H = -\frac{1}{2}\sum_{ij}\{X_{ij}\sigma_i\sigma_j + 2S_{ij}b_ib_j^\dagger + R_{ij}b_ib_j + \tilde{R}_{ij}b_i^\dagger b_j^\dagger\} - g\mu_B\sum_i (H^A)^\alpha \gamma_i^\alpha \sigma_i \, . \tag{5.4}$$

The prefactors in the Hamiltonian represent the renormalized interaction between the spins including the Heisenberg interaction and the asymmetric DMI. The Fourier transformed prefactors are defined in the subsequent section. Notice that within this representation the asymmetry is reflected by the relation $S_{ij} \neq S_{ji}$.

The equation of motion of the Pauli operators (Section 2.2) on the basis of Eq. (5.4) reads:

$$
\begin{aligned}
\left[b_l, H\right]_- = \frac{1}{2}\sum_j &\Big\{(X_{lj} + X_{jl})\sigma_j b_l + 2Z_{lj}b_lb_j + 2\tilde{Z}_{lj}b_lb_j^\dagger - 4\tilde{Z}_{jl}\sigma_j\sigma_l - 4S_{jl}\sigma_l b_j \\
&- 2(\tilde{R}_{lj} + \tilde{R}_{jl})\sigma_l b_j^\dagger\Big\} + (H^A)^\alpha(b_l\gamma_l^\alpha - 2(A_l^*)^\alpha\sigma_l)
\end{aligned} \tag{5.5}
$$

The many-particle system described by Eq. (5.4) is investigated by the thermodynamic Green's function method as described in Section 2.4. The decoupling of the equations of motion is done by RPA. After some algebra the excitation energy of spin waves can be derived by the eigenvalues of the following matrix equation

$$\underbrace{\begin{pmatrix} \omega - \varepsilon_{\mathbf{q},\mathbf{Q}}^{11} & \varepsilon_{\mathbf{q},\mathbf{Q}}^{12} \\ -\varepsilon_{\mathbf{q},\mathbf{Q}}^{12} & \omega + \varepsilon_{-\mathbf{q},\mathbf{Q}}^{11} \end{pmatrix}}_{\Lambda} \begin{pmatrix} \langle\langle b; b^\dagger\rangle\rangle_{\mathbf{q}} & \langle\langle b; b\rangle\rangle_{\mathbf{q}} \\ \langle\langle b^\dagger; b^\dagger\rangle\rangle_{\mathbf{q}} & \langle\langle b^\dagger; b\rangle\rangle_{\mathbf{q}} \end{pmatrix} = \begin{pmatrix} 2\langle\sigma\rangle & 0 \\ 0 & -2\langle\sigma\rangle \end{pmatrix} , \tag{5.6}$$

where the coefficients obtained from the decoupling reads:

$$\varepsilon_{\mathbf{q},\mathbf{Q}}^{11} = \langle\sigma\rangle\left(X_{0,\mathbf{Q}} - 2S_{\mathbf{q},\mathbf{Q}}\right) + g\mu_B(H^A)^\alpha\gamma^\alpha \tag{5.7a}$$

$$\varepsilon_{\mathbf{q},\mathbf{Q}}^{12} = 2\langle\sigma\rangle R_{\mathbf{q},\mathbf{Q}} = \langle\sigma\rangle\frac{\rho^2}{2}\left(J_{\mathbf{q}} + J_{\mathbf{q}}^A - \frac{1}{2}P_{\mathbf{q},\mathbf{Q}}\right) \tag{5.7b}$$

with

$$X_{\mathbf{q},\mathbf{Q}} = \left(J_{\mathbf{q}} + J_{\mathbf{q}}^A\right)(\gamma^z)^2 + \frac{\rho^2}{2}P_{\mathbf{q},\mathbf{Q}} \tag{5.7c}$$

$$S_{\mathbf{q},\mathbf{Q}} = \frac{1}{4}\left(J_{\mathbf{q}} + J_{\mathbf{q}}^A\right)\rho^2 - \frac{1}{8}\left((\gamma^z)^2 + 1\right)P_{\mathbf{q},\mathbf{Q}} + \frac{1}{4}\gamma^z V_{\mathbf{q},\mathbf{Q}}\,. \tag{5.7d}$$

The magnetization points in direction of the magnetic anisotropy. Spin waves of wave vector $\mathbf{q}$ and the direction of the propagation of the incommensurate spin spiral with wave vector $\mathbf{Q}$ are defined by the quantization axis $\boldsymbol{\gamma}$. In case of $\tau = z$, the spiral orientations vary around the z direction. The deviation from the collinear state is characterized by $\gamma^\tau < 1$. In the parallel aligned state the condition reads $\gamma^\tau = 1$. The cycloidal or screw state corresponds to $\gamma^\tau = 0$. The wave vector of the spin spiral is determined by minimizing the free energy. The spin-wave dispersion relation of the low-lying states, given by the poles of the Green's function, reads

$$\begin{aligned}\varepsilon_{\mathbf{q},\mathbf{Q}}^{(\pm)} &= u_{\mathbf{q},\mathbf{Q}} \pm v_{\mathbf{q},\mathbf{Q}} \\ &= \frac{\gamma^\tau\langle\sigma\rangle}{2}V_{\mathbf{q},\mathbf{Q}} \pm \sqrt{\frac{\frac{1}{2}[(\gamma^\tau\langle\sigma\rangle)^2(J_{\mathbf{q}} + J_{\mathbf{q}}^A - \frac{1}{2}P_{\mathbf{q},\mathbf{Q}}) - \langle\sigma\rangle^2(J_{\mathbf{q}} + J_{\mathbf{q}}^A - \frac{1}{2}P_{0,\mathbf{Q}})]*}{*[P_{0,\mathbf{Q}} - P_{\mathbf{q},\mathbf{Q}}]}}\end{aligned} \tag{5.8}$$

with

$$\gamma^\tau\langle\sigma\rangle = \frac{g\mu_B H^A}{\frac{1}{2}P_{0,\mathbf{Q}} - (J_0 + J_0^A)}\,. \tag{5.9}$$

The last equation determines the wave vector $\mathbf{Q}$, which is chosen in such a way as to minimize the free energy. The necessary condition of a minimum is

$$\begin{aligned}\left\langle\left[b_l, H\right]_-\right\rangle = 0 &= \langle\sigma\rangle\left\{\tilde{Z}_{0,\mathbf{Q}}\langle\sigma\rangle + g\mu_B H^A\frac{\rho}{2}\right\} \\ &= \langle\sigma\rangle\rho\left\{\gamma^z\langle\sigma\rangle\left[J_0 + J_0^A - \frac{1}{2}P_{0,Q}\right] + g\mu_B H^A\right\}\,.\end{aligned} \tag{5.10}$$

Generally speaking, the choice of $\mathbf{Q}$ must correspond to a minimum of the free energy (or the energy of the ground state as the temperature goes to zero $(T \to 0)$. As is shown in [114, 183], this choice coincides with the requirement that the non-diagonal mean values

vanish $\langle b \rangle = \langle b^\dagger \rangle = 0$ which, in its turn, leads to an exact implicit equation for the wave vector $\mathbf{Q}$.

The dispersion relation of the magnetic system obtained in Eq. (5.8) consists of two parts. The asymmetric first part, with the function

$$V_{\mathbf{q},\mathbf{Q}} = -V_{-\mathbf{q},\mathbf{Q}} = J_{\mathbf{q}+\mathbf{Q}} - J_{\mathbf{q}-\mathbf{Q}} + \mathrm{i}[D^\tau_{\mathbf{q}+\mathbf{Q}} + D^\tau_{\mathbf{q}-\mathbf{Q}}] , \tag{5.11}$$

only contributes in case of a spin alignment with an additional component in the direction of the DM-vector. This can be interpreted as a conical spin spiral. The second part is symmetric with a renormalized interaction

$$P_{\mathbf{q},\mathbf{Q}} = P_{-\mathbf{q},\mathbf{Q}} = J_{\mathbf{q}+\mathbf{Q}} + J_{\mathbf{q}-\mathbf{Q}} + \mathrm{i}(D^\tau_{\mathbf{q}-\mathbf{Q}} - D^\tau_{\mathbf{q}+\mathbf{Q}}) \tag{5.12}$$

and contributes also in case of a screw or cycloidal spin ordering. The positive branch of the spin-wave dispersion relation is chosen because a negative excitation energy indicates an instability of the system. In case of $\gamma^\tau \neq 0$ the dispersion relation becomes asymmetric with respect to the wave vector $\mathbf{q}$. The rotational sense (chirality) is defined by the interplay between the different interactions of the magnetic system. This interplay results in a wave vector $\mathbf{Q}$ which is related to a constant canting of spins between adjacent lattice sites. The rotational sense depends on the sign of the DMI, allowing only one type of chirality, which is in accordance with [8]. The asymmetry is characterized by

$$\Delta\varepsilon_{\mathbf{q},\mathbf{Q}} = \varepsilon_{\mathbf{q},\mathbf{Q}} - \varepsilon_{-\mathbf{q},\mathbf{Q}} = \gamma^\tau \langle \sigma \rangle V_{\mathbf{q},\mathbf{Q}} = \gamma^\tau \langle \sigma \rangle \{ J_{\mathbf{q}+\mathbf{Q}} - J_{\mathbf{q}-\mathbf{Q}} + \mathrm{i}[D^\tau_{\mathbf{q}+\mathbf{Q}} + D^\tau_{\mathbf{q}-\mathbf{Q}}]\} . \tag{5.13}$$

Here both, the symmetric J_{ij} and the antisymmetric interaction D^τ_{ij} contribute to the chirality-dependent asymmetry. In accordance with recent calculations [184] only the components of the DM-vector parallel to the ground state magnetization γ^τ influence the dispersion relation. In case of all moments are perpendicular to the anisotropy direction ($\gamma^\tau = 0$) the asymmetry vanishes.

Because the Green's function, defined in Eq. (5.6), includes the statistical average we find also the temperature dependence of the asymmetry via the temperature dependence of the magnetization $\langle \sigma \rangle$. The Green's function matrix calculated form Eq. (5.6) is given as:

$$G_{\mathbf{q}}(\omega) = 2 \langle \sigma \rangle \Lambda^{-1} \begin{pmatrix} 1 & 0 \\ 0 & -1 \end{pmatrix} = \frac{2 \langle \sigma \rangle}{(\omega - \varepsilon^{(+)}_{\mathbf{q},\mathbf{Q}})(\omega - \varepsilon^{(-)}_{\mathbf{q},\mathbf{Q}})} \begin{pmatrix} \omega + \varepsilon^{11}_{-\mathbf{q},\mathbf{Q}} & \varepsilon^{12}_{\mathbf{q},\mathbf{Q}} \\ \varepsilon^{12}_{\mathbf{q},\mathbf{Q}} & -(\omega - \varepsilon^{11}_{\mathbf{q},\mathbf{Q}}) \end{pmatrix} , \tag{5.14}$$

which leads to

$$G_{\mathbf{q}}^{11}(\omega) = \langle \sigma \rangle \left\{ \frac{\varepsilon_{\mathbf{q},\mathbf{Q}}^{11} + \varepsilon_{-\mathbf{q},\mathbf{Q}}^{11}}{2v_{\mathbf{q},\mathbf{Q}}} \Big[\frac{1}{\omega - \varepsilon_{\mathbf{q},\mathbf{Q}}^{(+)}} - \frac{1}{\omega - \varepsilon_{\mathbf{q},\mathbf{Q}}^{(-)}} \Big] + \Big[\frac{1}{\omega - \varepsilon_{\mathbf{q},\mathbf{Q}}^{(+)}} + \frac{1}{\omega - \varepsilon_{\mathbf{q},\mathbf{Q}}^{(-)}} \Big] \right\} \quad (5.15a)$$

$$G_{\mathbf{q}}^{22}(\omega) = \langle \sigma \rangle \left\{ \frac{\varepsilon_{\mathbf{q},\mathbf{Q}}^{11} + \varepsilon_{-\mathbf{q},\mathbf{Q}}^{11}}{2v_{\mathbf{q},\mathbf{Q}}} \Big[\frac{1}{\omega - \varepsilon_{\mathbf{q},\mathbf{Q}}^{(+)}} - \frac{1}{\omega - \varepsilon_{\mathbf{q},\mathbf{Q}}^{(-)}} \Big] - \Big[\frac{1}{\omega - \varepsilon_{\mathbf{q},\mathbf{Q}}^{(+)}} + \frac{1}{\omega - \varepsilon_{\mathbf{q},\mathbf{Q}}^{(-)}} \Big] \right\} \quad (5.15b)$$

$$G_{\mathbf{q}}^{12}(\omega) = G_{\mathbf{q}}^{21}(\omega) = \langle \sigma \rangle \frac{\varepsilon_{\mathbf{q},\mathbf{Q}}^{12}}{2v_{\mathbf{q},\mathbf{Q}}} \Big[\frac{1}{\omega - \varepsilon_{\mathbf{q},\mathbf{Q}}^{(+)}} - \frac{1}{\omega - \varepsilon_{\mathbf{q},\mathbf{Q}}^{(-)}} \Big] \quad (5.15c)$$

The correlation functions are connected to the Green's function by the spectral theorem (Section 2.4.2). Using this relation, the correlation functions are given as:

$$\langle b^\dagger b \rangle_{\mathbf{q},\mathbf{Q}} = \langle \sigma \rangle \left\{ \frac{1}{2\sinh(\frac{\beta}{2}\varepsilon_{\mathbf{q},\mathbf{Q}}^{(+)})\sinh(\frac{\beta}{2}\varepsilon_{\mathbf{q},\mathbf{Q}}^{(-)})} \Big[\sinh \beta u_{\mathbf{q},\mathbf{Q}} - \frac{\varepsilon_{\mathbf{q},\mathbf{Q}}^{11} + \varepsilon_{-\mathbf{q},\mathbf{Q}}^{11}}{2v_{\mathbf{q},\mathbf{Q}}} \sinh \beta v_{\mathbf{q},\mathbf{Q}} \Big] - 1 \right\}$$

$$(5.16)$$

$$\langle bb \rangle_{\mathbf{q},\mathbf{Q}} = \langle \sigma \rangle \frac{\varepsilon_{\mathbf{q},\mathbf{Q}}^{12} \sinh \beta v_{\mathbf{q},\mathbf{Q}}}{2v_{\mathbf{q},\mathbf{Q}} \sinh(\frac{\beta}{2}\varepsilon_{\mathbf{q},\mathbf{Q}}^{(+)})\sinh(\frac{\beta}{2}\varepsilon_{\mathbf{q},\mathbf{Q}}^{(-)})} \quad (5.17)$$

The averaged magnetization $\langle \sigma \rangle = \frac{1}{2} - \frac{1}{N}\sum_q \langle b^\dagger b \rangle_q$ is given by:

$$\langle \sigma \rangle = \frac{1}{2}\left(\frac{1}{N}\sum_q \frac{\sinh \beta u_{\mathbf{q},\mathbf{Q}} - \frac{\varepsilon_{\mathbf{q},\mathbf{Q}}^{11} + \varepsilon_{-\mathbf{q},\mathbf{Q}}^{11}}{2v_{\mathbf{q},\mathbf{Q}}} \sinh \beta v_{\mathbf{q},\mathbf{Q}}}{\sinh(\frac{\beta}{2}\varepsilon_{\mathbf{q},\mathbf{Q}}^{(+)})\sinh(\frac{\beta}{2}\varepsilon_{\mathbf{q},\mathbf{Q}}^{(-)})} \right)^{-1} \quad (5.18)$$

The analytical results obtained for the magnetization and the wave vector $\mathbf{Q}$ have to be calculated by adequate numerical methods.

5.2. Numerical results and discussion

The influence of the chirality on the calculated spin-wave spectrum along q_x is shown in Fig. 5.2 for three different temperatures. The asymmetry of the dispersion relation is magnified around $^a\pi/_2$. Here the breaking of the degeneracy of the excitation energy by the DM interaction is clearly visible in the lower two graphs. The excitation energy is reduced in the negative wave vector branch, whereas it is enhanced in the positive branch. The energy becomes soft at the Brillouin zone center. This is referred as the Nambu-Goldstone mode [185], which corresponds to a rigid rotation of the whole spin spiral [5, 186]. The excitation energy is shown for three different temperatures. At low temperatures (solid line) the excitation energy is at its maximum. With increasing temperature the energy reduces with a strong reduction close to the phase transition temperature (dashed line).
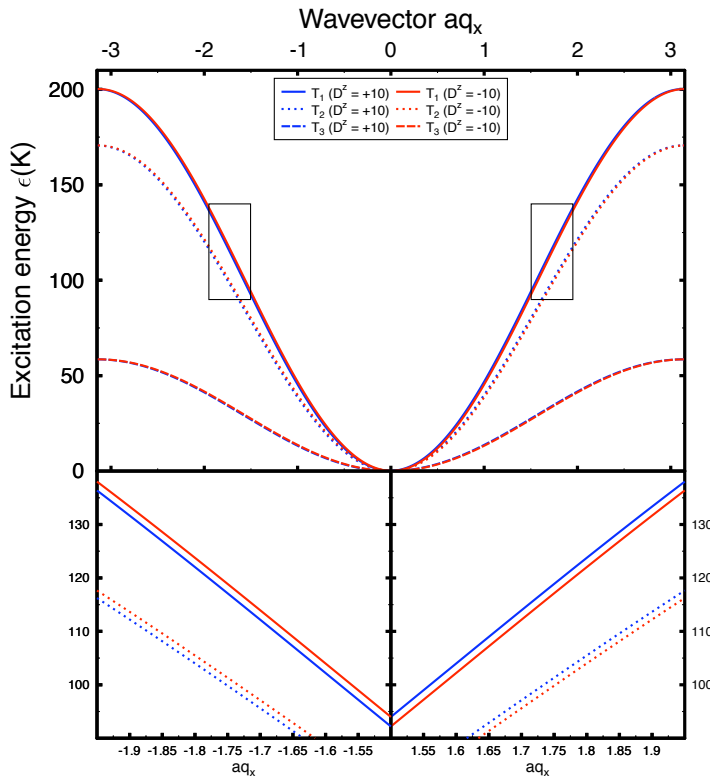

Fig. 5.2.: Asymmetric spin-wave dispersion relation for two different chirality (red/blue), at three different temperatures $T_1 = 1\,\text{K}$, $T_2 = 50\,\text{K}$ and $T_3 = 95\,\text{K}$. The lower graphs show the change in the excitation energy around $aq_x = \frac{\pi}{2}$, if the chirality is reversed. The phase transition temperature is about $T_c = 100\,\text{K}$. The parameters read $J = 100\,\text{K}$, $J^A = 0.1\,\text{K}$, $|D^z| = 10\,\text{K}$, $H^A = 0.0001\,\text{K}$ and $\gamma^z = 0.6$.

The asymmetry of the spin-wave dispersion relation is depicted in Fig. 5.3. It shows a distinct maximum at $aq_x = \pi/2$, with the lattice constant a. A switching of the magnetization is equivalent to a change of sign of γ^τ and changes the sign of the asymmetry, as well, which is in agreement with recent experimental results [9].
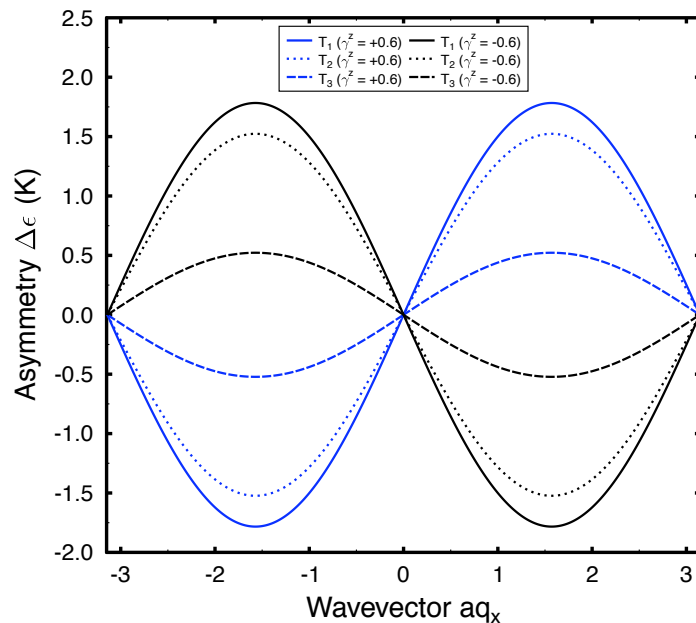

Fig. 5.3.: Asymmetry of energy as a function of wave vector for two different directions of magnetization at three different temperatures ($T_1 < T_2 < T_3$).

The deviations of the asymmetry in experiments to those of the model are assumed to be related to the restriction to nearest neighbor interaction and a different coordination number. With increasing temperature, the asymmetry is reduced as shown in Fig. 5.3.

6. Many-particle approach to multiferroic bulk systems

6.1. The model and Green's function

As demonstrated before, the Green's function technique allows a broad variety of applications. In this section a new approach for the description of multiferroics is shown. The model consists of two subsystems. The magnetic part is described by the Heisenberg model and the Dzyaloshinskii-Moriya interaction (DMI), where the DMI is needed to include spiral spin arrangements. Anisotropic relativistic interactions seems to be responsible for magnetic cycloidal spirals [187]. The magnetic system is characterized by spin operators $\mathbf{S}$ on a lattice. As mentioned in the introduction the ferroelectric behavior is stimulated by charge ordering processes. A typical model to describe such a situation is given by the Ising model in a transverse field (Section 2.5). Here we consider for simplicity two different charge ordering positions denoted by a pseudospin $P^z = \pm 1/2$. Since we are interested in multiferroics of type-I, the coupling between the ferroelectric and the magnetic subsystem is assumed to be weak. Due to [188], this type-I multiferroics allow a biquadratic coupling in spin $\mathbf{S}$ and pseudo-spin operators $\mathbf{P}$. The Hamiltonian reads:

$$H = H_m + H_f + H_c \tag{6.1}$$

The three parts describe the magnetic subsystem H_m, the ferroelectric one H_f and the symmetry allowed coupling H_c. They are defined by

$$H_m = -\frac{1}{2}\sum_{ij} J_{ij}\mathbf{S}_i\mathbf{S}_j - \frac{1}{2}\sum_{ij}\mathbf{D}_{ij}(\mathbf{S}_i \times \mathbf{S}_j) - \mathbf{H}\sum_i \mathbf{S}_i \tag{6.2}$$

$$H_f = -\frac{1}{2}\sum_{kl} K_{kl}P_k^z P_l^z - 2\sum_i \Omega_i^x P_i^x - 2\mu E^z \sum_i P_i^z \tag{6.3}$$

$$H_c = -\frac{1}{2}\sum_{ijkl} g_{ijkl}\mathbf{S}_i\mathbf{S}_j P_k^z P_l^z \,. \tag{6.4}$$

Here the magnetic system is characterized by the symmetric isotropic exchange coupling by J_{ij} and the relativistic DMI by the antisymmetric coupling vector $\mathbf{D}_{ij}$ between nearest

neighbors. $\mathbf{H}$ denotes the external magnetic field. The ferroelectric system is identified by the coupling K_{ij} between adjacent double well potentials situated at lattice points i and j, respectively. The parameter Ω stands for the tunnel frequency through the barrier and $\mathbf{E}$ denotes an external electric field, see [82]. The general form of a biqudratic coupling between both subsystems is introduced in Eq. (6.4). Since the investigated multiferroics of type-I have well separated transition temperatures, the mutual influence of fluctuation on the corresponding other subsystem can be assumed negligible. Hence the model can be simplified in a dynamical mean-field approach leading to the effective coupling strengths:

$$
\begin{aligned}
J_{ij} &\to \tilde{J}_{ij} = J_{ij} + \sum_{kl} g_{ijkl} \langle P_k^z P_l^z \rangle \\
K_{kl} &\to \tilde{K}_{kl} = K_{kl} + \sum_{ij} g_{ijkl} \langle \mathbf{S}_i \mathbf{S}_j \rangle
\end{aligned}
\tag{6.5}
$$

in the magnetic and ferroelectric subsystem. The renormalized interactions are temperature dependent by the thermal average.

For the description of magnetic systems allowing spiral structure, some special cases had been discussed in some former papers [181, 182]. More recently non-collinear arrangements has been discussed on a mesoscopic level [70] or within microscopic models [5, 189]. In the present approach, the spin operators of the magnetic system, as well as the pseudo-spin operators of the ferroelectric system are transformed into the eigen representation of the quantization axis, which was presented in Section 2.2. This real unit vector is denoted as $\boldsymbol{\gamma}_i^m = (\gamma_i^{m,x}, \gamma_i^{m,y}, \gamma_i^{m,z})$ for the magnetic system and $\boldsymbol{\gamma}_i^f = (\gamma_i^{f,x}, \gamma_i^{f,y}, \gamma_i^{f,z})$ for the ferroelectric system. The respective transformation of the spin-$\frac{1}{2}$ operators is defined in terms of Pauli operators $b^\dagger$, b and $a^\dagger$, a for the magnetic system and the ferroelectric system, respectively. Following [10] the most general form reads:

$$
S_i^\alpha = \gamma_i^{m,\alpha} \sigma_i^m + B_i^\alpha b_i + (B_i^*)^\alpha b_i^\dagger \,, \tag{6.6}
$$
$$
P_i^\alpha = \gamma_i^{f,\alpha} \sigma_i^f + A_i^\alpha a_i + (A_i^*)^\alpha a_i^\dagger \,. \tag{6.7}
$$

The coefficients in Eqn. (6.6), (6.7) are chosen in such a manner, that the commutation relations of spin operators are guaranteed. Using this realization [10] and considering the symmetry of the magnetic and ferroelectric system the transformation reads:

$$
\boldsymbol{\gamma}_i^m = (\cos \mathbf{Q}\mathbf{r}_i, \sin \mathbf{Q}\mathbf{r}_i, 0) \quad \text{with} \quad \mathbf{B}_i = \frac{1}{2}(-\mathrm{i}\sin \mathbf{Q}\mathbf{r}_i, \mathrm{i}\cos \mathbf{Q}\mathbf{r}_i, 1) \tag{6.8}
$$

$$
\boldsymbol{\gamma}_i^f = \left(\sin \vartheta, 0, \cos \vartheta \right) \quad \text{with} \quad \mathbf{A}_i = \frac{1}{2}\left(\cos \vartheta, -\mathrm{i}, -\sin \vartheta \right). \tag{6.9}
$$

Here, the quantization axis of the magnetic system varies periodically in the $x - y$ plane

in spin space, by a site dependent angle $\mathbf{Q}\mathbf{r}_i$, whereas in the ferroelectric system the quantization axis is rotated by a site independent angle ϑ in the $x - z$ plane in the pseudo-spin space.

The Hamiltonian is transformed into in the following compressed form by using the realization in Eqn. (6.8), (6.9). Here only even terms in the annihilation and creation operators have to be taken into account. The magnetic part of the Hamiltonian is expressed by

$$H_m = -\frac{1}{2} \sum_{ij} \{ X_{ij}^m \sigma_i^m \sigma_j^m + 2S_{ij}^m b_i b_j^\dagger + R_{ij}^m b_i b_j + \tilde{R}_{ij}^m b_i^\dagger b_j^\dagger \} . \tag{6.10a}$$

Using the same procedure the ferroelectric part reads:

$$H_f = -\frac{1}{2} \sum_{ij} \{ X_{ij}^f \sigma_i^p \sigma_j^p + 2S_{ij}^f a_i a_j^\dagger + R_{ij}^f a_i a_j + \tilde{R}_{ij}^f a_i^\dagger a_j^\dagger \} - 2 \sum_i \{ C_i^\alpha \gamma_i^{f,\alpha} \sigma_i^p \} \tag{6.10b}$$

with

$$\mathbf{C}_i = (\Omega_i^x, 0, \mu E^z) . \tag{6.10c}$$

In the subsequent section the Hamiltonian with the transformed operators and the renormalized interaction due to the ME-coupling $H = H_f + H_m$ is studied in terms of Green's functions which enable us to find out the excitation spectrum of the coupled model. It has to be noted, that although the form of both parts of the Hamiltonian looks similar, the coefficients X, S and R are quite different for the magnetic and the ferroelectric subsystem.

The interacting many-particle systems described by Eqn. (6.10) are investigated by the thermodynamic Green's function method, which yields the dispersion relation of the elementary excitations of the coupled model. The spectrum again determines the thermodynamic behavior of the system, in particular, the polarization and the transverse magnetization. In the present model, the Green's functions are grouped as 2×2 matrices for the magnetic system $G_{\mathbf{q}}^{(m)}(\omega)$ and for the ferroelectric system $G_{\mathbf{q}}^{(f)}(\omega)$ as:

$$G_{\mathbf{q}}^{(m)}(\omega) = \begin{pmatrix} \langle\langle b; b^\dagger \rangle\rangle_{\mathbf{q}} & \langle\langle b; b \rangle\rangle_{\mathbf{q}} \\ \langle\langle b^\dagger; b^\dagger \rangle\rangle_{\mathbf{q}} & \langle\langle b^\dagger; b \rangle\rangle_{\mathbf{q}} \end{pmatrix} , \quad G_{\mathbf{q}}^{(f)}(\omega) = \begin{pmatrix} \langle\langle a; a^\dagger \rangle\rangle_{\mathbf{q}} & \langle\langle a; a \rangle\rangle_{\mathbf{q}} \\ \langle\langle a^\dagger; a^\dagger \rangle\rangle_{\mathbf{q}} & \langle\langle a^\dagger; a \rangle\rangle_{\mathbf{q}} \end{pmatrix} . \tag{6.11}$$

The Green's function approach leads to a whole hierarchy of equations, which will be decoupled in random phase approximation (RPA). After some algebra the Green's

functions obey the following equation

$$
\underbrace{\begin{pmatrix} \omega - \varepsilon_{\mathbf{q},\mathbf{Q}}^{(\alpha),11} & \varepsilon_{\mathbf{q},\mathbf{Q}}^{(\alpha),12} \\ -\varepsilon_{\mathbf{q},\mathbf{Q}}^{(\alpha),12} & \omega + \varepsilon_{\mathbf{q},\mathbf{Q}}^{(\alpha),11} \end{pmatrix}}_{\Lambda^{(\alpha)}} G_{\mathbf{q}}^{(\alpha)}(\omega) = \begin{pmatrix} 2\left\langle \sigma^{(\alpha)} \right\rangle & 0 \\ 0 & -2\left\langle \sigma^{(\alpha)} \right\rangle \end{pmatrix}.
\tag{6.12}
$$

The index $(\alpha) = \{(m), (f)\}$ denotes the the magnetic and the ferroelectric subsystem, respectively. Even though the structure of the system of Green's functions of Eq. (6.12) looks equal, the corresponding excitation energies given by the eigenvalues of $\Lambda^{(\alpha)}$ and the resulting polarization $\left\langle \sigma^f \right\rangle$ and the magnetization $\left\langle \sigma^m \right\rangle$ are quite different. The magnetic subsystem is determined by:

$$
\varepsilon_{\mathbf{q},\mathbf{Q}}^{(m),11} = \left\langle \sigma^m \right\rangle \left(X_{0,\mathbf{Q}}^m - 2S_{\mathbf{q},\mathbf{Q}}^m \right) = -\left\langle \sigma^m \right\rangle \frac{1}{2}\left(P_{0,\mathbf{Q}} + \tilde{J}_{\mathbf{q}} - \frac{1}{2} P_{\mathbf{q},\mathbf{Q}} \right)
\tag{6.13a}
$$

$$
\varepsilon_{\mathbf{q},\mathbf{Q}}^{(m),12} = 2\left\langle \sigma^m \right\rangle R_{\mathbf{q},\mathbf{Q}}^m = \left\langle \sigma^m \right\rangle \frac{1}{2}\left(\tilde{J}_{\mathbf{q}} - \frac{1}{2} P_{\mathbf{q},\mathbf{Q}} \right)
\tag{6.13b}
$$

with a renormalized interaction

$$
P_{\mathbf{q},\mathbf{Q}} = P_{-\mathbf{q},\mathbf{Q}} = \tilde{J}_{\mathbf{q}+\mathbf{Q}} + \tilde{J}_{\mathbf{q}-\mathbf{Q}} + \mathrm{i}\left(D_{\mathbf{q}-\mathbf{Q}}^z - D_{\mathbf{q}+\mathbf{Q}}^z \right).
\tag{6.13c}
$$

The ferroelectric subsystem obeys:

$$
\begin{aligned}
\varepsilon_{\mathbf{q}}^{(f),11} &= \left\langle \sigma^f \right\rangle \left[X_0^f - 2S_q^f \right] + 2C^\alpha \gamma^{f,\alpha} = \left\langle \sigma^f \right\rangle \left(\tilde{K}_0 \cos^2 \vartheta - \frac{1}{2} \tilde{K}_{\mathbf{q}} \sin^2 \vartheta \right) + 2C^\alpha \gamma^{f,\alpha}, \\
\varepsilon_{\mathbf{q}}^{(f),12} &= 2\left\langle \sigma^f \right\rangle R_{\mathbf{q}}^f = \frac{1}{2}\left\langle \sigma^f \right\rangle \tilde{K}_{\mathbf{q}} \sin^2 \vartheta
\end{aligned}
\tag{6.14}
$$

with

$$
X_0^f = \tilde{K}_0 \cos^2 \vartheta, \quad S_{\mathbf{q}}^f = \frac{1}{4} \tilde{K}_{\mathbf{q}} \sin^2 \vartheta, \quad Z_{\mathbf{q}}^f = \frac{1}{2} \tilde{K}_{\mathbf{q}} \cos \vartheta \sin \vartheta.
\tag{6.15}
$$

The magnetization points in a direction in the $x - y$ plane. Spin waves of wave vector $\mathbf{q}$ and the direction of the propagation of the incommensurate spin spiral with wave vector $\mathbf{Q}$ are defined by the quantization axis $\boldsymbol{\gamma}^m$. In the present case the spiral orientation varies around the z direction with a cycloidal or screw state $(\gamma^z = 0)$. Both, the wave vector of the spin spiral and the rotation angle in the ferroelectric system are determined by minimizing the free energy. The spin-wave dispersion relation $\varepsilon_{\mathbf{q},\mathbf{Q}}^{(m)}$ and the pseudo-spin-wave dispersion relation $\varepsilon_{\mathbf{q}}^{(f)}$ of the low-lying states, both symmetric with respect to

the wave vector $\mathbf{q}$, are given by the poles of the Green's functions as

$$\varepsilon_{\mathbf{q},\mathbf{Q}}^{(m)} = \pm\sqrt{\frac{1}{2}\left\langle\sigma^m\right\rangle^2 [\frac{1}{2}P_{0,\mathbf{Q}} - (\tilde{J}_{\mathbf{q}})][P_{0,\mathbf{Q}} - P_{\mathbf{q},\mathbf{Q}}]}\,, \tag{6.16}$$

$$\varepsilon_{\mathbf{q}}^{(f)} = \pm\sqrt{\left[\left\langle\sigma^f\right\rangle \tilde{K}_0\cos^2\vartheta + 2C^\alpha\gamma^{f,\alpha}\right]\left[\left\langle\sigma^f\right\rangle \tilde{K}_0\cos^2\vartheta + 2C^\alpha\gamma^{f,\alpha} - \left\langle\sigma^f\right\rangle \tilde{K}_{\mathbf{q}}\sin^2\vartheta\right]}\,, \tag{6.17}$$

with the renormalized interaction strengths of the ferroelectric $\tilde{K}_{\mathbf{q}}$ and the magnetic system $\tilde{J}_{\mathbf{q}}$:

$$\begin{aligned}
\tilde{J}_{\mathbf{q}} &= \left(J_0 + g_{0,0}\cos^2\vartheta\left\langle\sigma^f\right\rangle^2\right)\frac{J_{\mathbf{q}}}{J_0}\,, \\
\tilde{K}_{\mathbf{q}} &= \left(K_0 + g_{\mathbf{Q},0}\left\langle\sigma^m\right\rangle^2\right)\frac{K_{\mathbf{q}}}{K_0}\,.
\end{aligned} \tag{6.18}$$

Both quantities are temperature dependent by $\left\langle\sigma^f\right\rangle$ and $\left\langle\sigma^m\right\rangle$ and the form of the renormalized interaction is due to the chosen decoupling of the biquadratic ME-coupling term.

The wave-vector independent angle ϑ of the rotation in the $x-z$ plane in pseudo-spin space and the wave vector $\mathbf{Q}$ representing the pitch of the spin spiral structure are determined by the minimization of the free energy by

$$\left\langle\left[b_l, H\right]_-\right\rangle = 0 \quad\text{and}\quad \left\langle\left[a_l, H\right]_-\right\rangle = 0\,. \tag{6.19}$$

In the field-free case the following conditions within the RPA are found:

$$\tan(\mathbf{a}\mathbf{Q}) = -\frac{D^z}{\tilde{J}} \quad\text{and}\quad \tan\vartheta = \frac{2\Omega^x}{\tilde{K}_0\left\langle\sigma^f\right\rangle\cos\vartheta}\,. \tag{6.20}$$

The rotational sense (chirality) is defined by the interplay between the different interactions of the magnetic system, allowing only one type of chirality, which is in accordance with [8]. This results in a wave vector $\mathbf{Q}$ related to a constant canting of spins between adjacent lattice sites. The associated pitch of the magnetic spiral becomes temperature dependent due to the renormalized interaction strength $\tilde{J}$ given in Eq. (6.18). Originated by the ME-coupling the rotation angle is influenced by the pitch of the spiral wave vector. Here the mutual influence of the magnetic and the ferroelectric subsystems becomes evident.

The temperature dependence of the polarization and the transverse magnetization is found because the Green's functions, defined in Eq. (6.12), include the statistical average. The particular Green's function matrix for the magnetic system ($\alpha = m$) and for the

ferroelectric system ($\alpha = f$) are given as:

$$G_{\mathbf{q}}^{(\alpha)}(\omega) = 2\left\langle\sigma^{(\alpha)}\right\rangle(\Lambda^{(\alpha)})^{-1}\begin{pmatrix}1 & 0 \\ 0 & -1\end{pmatrix} = \frac{2\left\langle\sigma^{(\alpha)}\right\rangle}{(\omega-\varepsilon_{\mathbf{q},\mathbf{Q}}^{(\alpha)})(\omega+\varepsilon_{\mathbf{q},\mathbf{Q}}^{(\alpha)})}\begin{pmatrix}\omega+\varepsilon_{\mathbf{q},\mathbf{Q}}^{(\alpha),11} & \varepsilon_{\mathbf{q},\mathbf{Q}}^{(\alpha),12} \\ \varepsilon_{\mathbf{q},\mathbf{Q}}^{(\alpha),12} & -(\omega-\varepsilon_{\mathbf{q},\mathbf{Q}}^{(\alpha),11})\end{pmatrix}$$

$$(6.21)$$

which leads to

$$G_{\mathbf{q}}^{(\alpha),11}(\omega) = \left\langle\sigma^{(\alpha)}\right\rangle\left\{\frac{\varepsilon_{\mathbf{q},\mathbf{Q}}^{(\alpha),11}}{\varepsilon_{\mathbf{q},\mathbf{Q}}^{(\alpha)}}\left[\frac{1}{\omega-\varepsilon_{\mathbf{q},\mathbf{Q}}^{(\alpha)}} - \frac{1}{\omega+\varepsilon_{\mathbf{q},\mathbf{Q}}^{(\alpha)}}\right] + \left[\frac{1}{\omega-\varepsilon_{\mathbf{q},\mathbf{Q}}^{(\alpha)}} + \frac{1}{\omega+\varepsilon_{\mathbf{q},\mathbf{Q}}^{(\alpha)}}\right]\right\}, \quad (6.22a)$$

$$G_{\mathbf{q}}^{(\alpha),22}(\omega) = \left\langle\sigma^{(\alpha)}\right\rangle\left\{\frac{\varepsilon_{\mathbf{q},\mathbf{Q}}^{(\alpha),11}}{\varepsilon_{\mathbf{q},\mathbf{Q}}^{(\alpha)}}\left[\frac{1}{\omega-\varepsilon_{\mathbf{q},\mathbf{Q}}^{(\alpha)}} - \frac{1}{\omega+\varepsilon_{\mathbf{q},\mathbf{Q}}^{(\alpha)}}\right] - \left[\frac{1}{\omega-\varepsilon_{\mathbf{q},\mathbf{Q}}^{(\alpha)}} + \frac{1}{\omega+\varepsilon_{\mathbf{q},\mathbf{Q}}^{(\alpha)}}\right]\right\}, \quad (6.22b)$$

$$G_{\mathbf{q}}^{(\alpha),12}(\omega) = G_{\mathbf{q}}^{(\alpha),21}(\omega) = \left\langle\sigma^{(\alpha)}\right\rangle\frac{\varepsilon_{\mathbf{q},\mathbf{Q}}^{(\alpha),12}}{2\varepsilon_{\mathbf{q},\mathbf{Q}}^{(\alpha)}}\left[\frac{1}{\omega-\varepsilon_{\mathbf{q},\mathbf{Q}}^{(\alpha)}} - \frac{1}{\omega+\varepsilon_{\mathbf{q},\mathbf{Q}}^{(\alpha)}}\right]. \quad (6.22c)$$

Using the spectral theorem, the correlation functions $n^{(m)} = \left\langle b^\dagger b\right\rangle$ and $n^{(f)} = \left\langle a^\dagger a\right\rangle$ are determined as

$$n_{\mathbf{q},\mathbf{Q}}^{(\alpha)} = \left\langle\sigma^{(\alpha)}\right\rangle\left\{\frac{\varepsilon_{\mathbf{q},\mathbf{Q}}^{(\alpha),11}}{\varepsilon_{\mathbf{q},\mathbf{Q}}^{(\alpha)}}\coth(\frac{\beta}{2}\varepsilon_{\mathbf{q},\mathbf{Q}}^{(\alpha)}) - 1\right\} \quad (6.23)$$

The anormal averaged values are given by:

$$m_{\mathbf{q},\mathbf{Q}}^{(\alpha)} = \left\langle\sigma^{(\alpha)}\right\rangle\frac{\varepsilon_{\mathbf{q},\mathbf{Q}}^{(\alpha),12}}{\varepsilon_{\mathbf{q},\mathbf{Q}}^{(\alpha)}}\coth(\frac{\beta}{2}\varepsilon_{\mathbf{q},\mathbf{Q}}^{(\alpha)}). \quad (6.24)$$

The correlation function is connected to the averaged magnetization and averaged polarization by $\left\langle\sigma^{(\alpha)}\right\rangle = \frac{1}{2} - \frac{1}{N}\sum_q n_{\mathbf{q},\mathbf{Q}}^{(\alpha)}$.

$$\left\langle\sigma^{(\alpha)}\right\rangle = \frac{1}{2}\left(\frac{1}{N}\sum_q\left\langle\sigma^{(\alpha)}\right\rangle\left\{\frac{\varepsilon_{\mathbf{q},\mathbf{Q}}^{(\alpha),11}}{\varepsilon_{\mathbf{q},\mathbf{Q}}^{(\alpha)}}\coth(\frac{\beta}{2}\varepsilon_{\mathbf{q},\mathbf{Q}}^{(\alpha)})\right\}\right)^{-1} \quad (6.25)$$

The analytical results obtained in Eq. (6.25) are coupled equations which have to be solved iteratively by adequate numerical methods.

6.2. Numerical results and discussion

The analytical results obtained in the previous section are numerically solved for a certain set of parameters. The interaction energy of the spins in the magnetic subsystem is chosen as $J = 100\,\mathrm{K}$. The parameters of the ferroelectric subsystem are the interaction strength: $K = 100\,\mathrm{K}$ and the transverse field $\Omega = 10\,\mathrm{K}$. Due to the set of parameters the system have distinct phase transition points. In the following the temperature dependence of the magnetic and ferroelectric excitation energy, the polarization and the transverse magnetization is studied for several sets of the ME-coupling strength g and the strength of the DMI $|D^z|$.
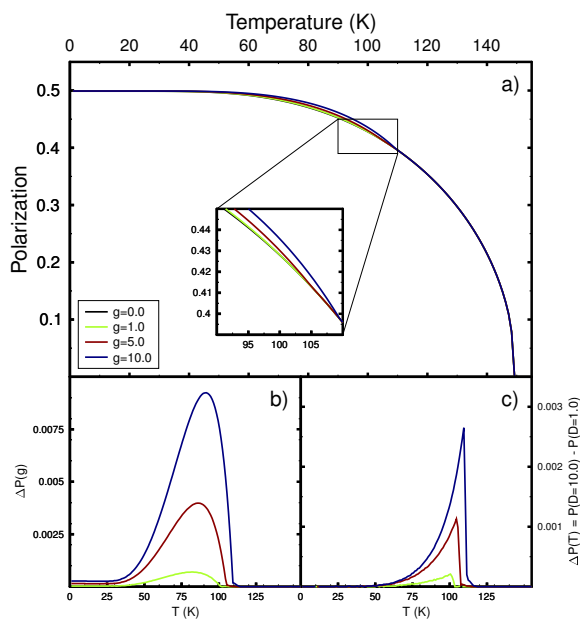
Fig. 6.1.: Temperature dependence of the polarization for different strength of the magneto-electric coupling. The lower left graph (b) shows the increase of polarization for different strengths of ME-coupling. The lower right graph (c) shows the additional effect on the polarization for increase DMI. In graph (a) and (b) $D^z = 1\,\mathrm{K}$.

The temperature dependence of the polarization for different ME-coupling strengths is shown in Fig. 6.1. The strength of the DMI is fixed at $D^z = 1\,\mathrm{K}$. The investigated system is ferroelectric up to $T_c = 145\,\mathrm{K}$ and magnetic up to $T_N = 100\,\mathrm{K}$ due to the set of parameters. Hence, the magnetic transition occurs at a lower temperature than the ferroelectric one. The polarization decreases with increasing temperature and vanishes continuously at the ferroelectric phase transition temperature. In the multiferroic phase, where the system is magnetic and ferroelectric, the polarization is enhanced. An increased ME-coupling strength leads to an enhanced polarization with a more pronounced kink around the magnetic phase transition. The inset shows a magnification of the temperature

dependence of the polarization around the magnetic phase transition. Changes in the polarization for three different ME-coupling strengths with respect to the non-coupled case $g = 0$ in the multiferroic regime are shown in the lower left graph (b). This is in accordance with the theoretical findings in [190]. The enhancement of the polarization $\Delta P(g) = P(g) - P(g = 0)$ is the largest one near to the magnetic phase transition. Here, the interplay between the magnetic and ferroelectric system is visible. The ferroelectric as well as the magnetic order (Fig. 6.6) are stabilized through the ME-coupling against temperature effects. The change of the polarization for two different DMI-strengths ($D^z = 1\,\mathrm{K}$ and $D^z = 10\,\mathrm{K}$) is shown in the lower right graph (b). The enhanced strength of the DMI leads to a further enhancement of the polarization, most pronounced in the vicinity of the magnetic phase transition. Here the different effects of the DMI and the ME-coupling can be seen. Whereas the ME-coupling leads to enhanced ferroelectric properties in the whole multiferroic phase, the effect of the spiral structure driven by the DMI is large only by approaching the magnetic phase transition temperature.
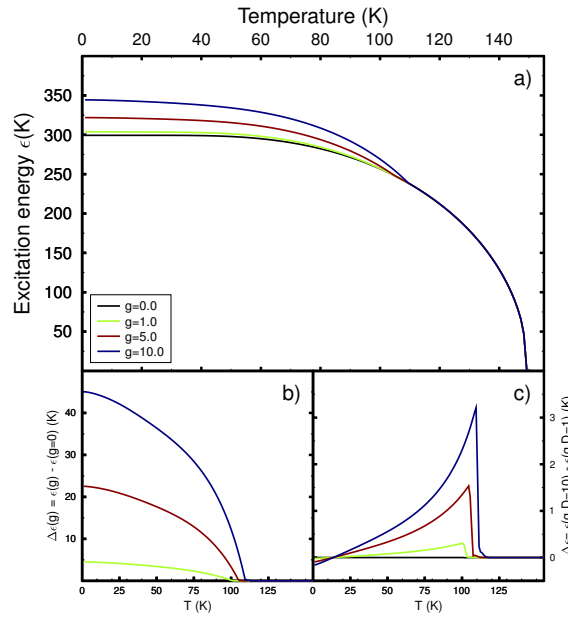

Fig. 6.2.: Temperature dependence of the excitation energy ($q = 0$) for different strength of magneto-electric coupling g. The lower left graph (b) shows the change of the excitation energy compared to the non-coupled case $g = 0$. The lower right graph (c) shows the additional effect on the energy for two different strengths of DM-interaction D^z. In graph (a) and (b) the DMI strength is constant at $D^z = 1\,\mathrm{K}$.

The influence of the ME-coupling, the DMI and competing temperature effects is more dominant in the energy of the elementary excitations of the ferroelectric subsystem shown in Fig. 6.2. Here, the excitation energy for zero wave vector is plotted for three different ME-coupling strengths and the non-coupled case, as a reference curve. The strength

of the DMI is fixed. The excitation energy decreases with increasing temperature and vanishes continuously at the ferroelectric phase transition temperature. The coupling of the ferroelectric modes to the spin order is discussed in [191]. A disconnection of the mode from the magnetic sublattice was observed, if the cycloidal disappears at T_N. In the multiferroic phase, where the system is magnetic and ferroelectric, the excitation energy is enhanced and the largest effect is observed for the largest ME-coupling strength. At the magnetic transition a kink in the excitation energy is observed. This is in accordance with experiments [192] and theoretical approaches [193].

Above T_N the material is paramagnetic and ferroelectric. Here no influence of the magnetic system can be observed. The largest gain in the energy of the excitations, with respect to the non-coupled case ($g = 0$), occurs at the lowest temperatures shown in the lower left graph (b) of Fig. 6.2. With increasing temperature the graphs narrow and coincide at the magnetic phase transition. The comparison of the excitation energy for two different strengths of the DMI by $\Delta\varepsilon = \varepsilon(g, D^z = 10\,\mathrm{K}) - \varepsilon(g, D^z = 1\,\mathrm{K})$ is shown in the lower right graph (c) of Fig. 6.2. In case of no effect of the DMI on the ferroelectric excitation spectrum $\Delta\varepsilon$ would be zero. The DMI supports the enhanced ME-coupling and yields a further enhancement of the excitation energy for almost the whole temperature regime. The reduction of the excitation energy at low temperatures is discussed in the next graph.

The effect of the strength of the DMI on the ferroelectric excitations is shown in Fig. 6.3. The ME-coupling strength is fixed to $g = 10\,\mathrm{K}$. The excitation energy reduces with increasing temperature and vanishes continuously at the ferroelectric phase transition. The influence of the DMI-strength close to the magnetic phase transition is magnified in the inset. Here with increasing DMI-strength also the excitation energy is enhanced. The opposite effect is observed at very low temperatures shown in the lower right graph (c) of Fig. 6.3. The reduced excitation energies at low temperatures is magnified. This can be understood by a weakening of the ME-coupling strength $g(\mathbf{Q})$, which is maximum for $|\mathbf{Q}| = 0$. The enhanced DMI results in a larger pitch $\mathbf{Q}$ of the spin spiral. On one hand, this additional ordering of the magnetic spins in a spiral structure, stabilizes the magnetic ordering against temperature effects, see also Fig. 6.6, on the other hand, the ME-coupling is reduced, if the spiral structure is more pronounced. This corresponds to a larger value of $|\mathbf{Q}|$.

With increasing temperature the stabilization of the magnetic phase, which corresponds to a shift of the transition temperature to higher values, is more dominant than the reduction of the ME-coupling by a larger pitch of the spiral. In that sense, the renormalization of the ferroelectric interaction $\tilde{K}_q$ by the temperature dependent transverse magnetization becomes more and more pronounced in comparison to the reduction of the ME-coupling
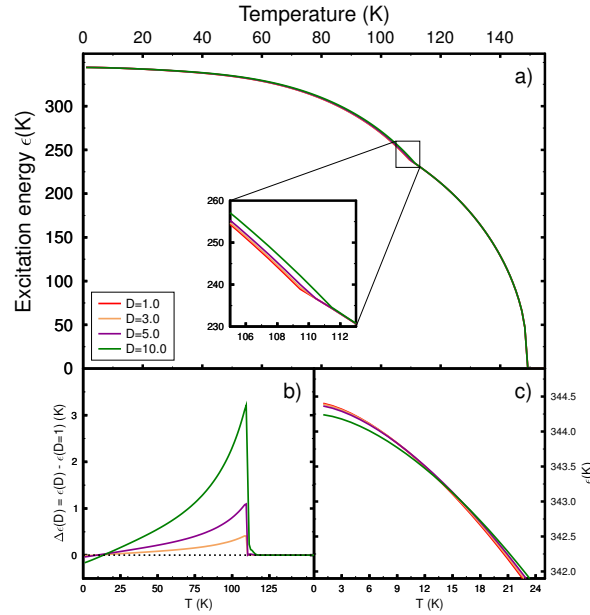
Fig. 6.3.: Temperature dependence of the excitation energy for different strengths of DMI. The inset shows the change in the excitation energy around the magnetic phase transition. The lower left graph (b) shows the change in energy with increasing strength of DMI. The lower right graph (c) shows the low temperature behavior of the energy. The ME-coupling reads $g = 10\,\mathrm{K}$.

strength itself. Thus the largest enhancement of the excitation energy with respect to the strength of the DMI is found in the vicinity of the magnetic transition, shown in Fig. 6.6. As the macroscopic properties, such as the polarization are determined by their microscopic excitations an equivalent behavior on a varied DMI-strength is observed for the polarization.

The spin-wave dispersion relation of small wave vectors of the magnetic subsystem for different strengths of the DMI is depicted in Fig. 6.4 for low temperatures ($T = 1\,\mathrm{K}$). The ME-coupling is set to $g = 10\,\mathrm{K}$ and the dispersion relation in the complete Brillouin zone is plotted in the inset. The excitation energy increases with increasing strength of the DMI. The effect is more pronounced at small wave vectors, as shown in the lower left graph (b) of Fig. 6.4. The difference in the spin-wave spectra for two different ME-coupling strengths is shown in the lower right graph (c). Here, the largest change is observed for the the smallest DMI-strengths. This implies a reduction of the effect of the ME-coupling on the spin-wave spectrum, if the DMI increases, and is supported by the ME-coupling dependent dispersion relation in Fig. 6.5.

With increasing ME-coupling strength the excitation energy is enhanced most pronounced at the Brillouin zone boundary. The change in energy around the zone center is plotted in the graph (b) and (c) of Fig. 6.4 for two different DMI strengths, respectively.
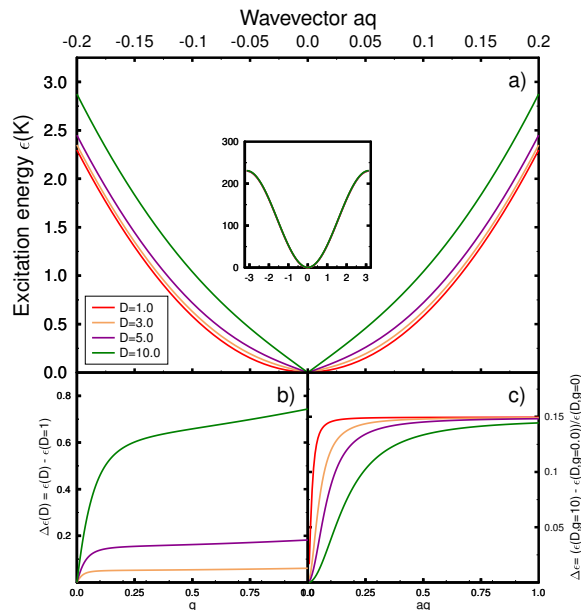
Fig. 6.4.: Magnetic dispersion relation around $q = 0$ for different strength of DMI. The lower left graph (b) shows the deviations in energy for different DMI. The lower right graph (c) shows the change in energy for an enlarged ME-coupling. In graph (a) and (b) $g = 10\,\mathrm{K}$.

The mutual effect of the DMI and the ME-coupling is also visible in the spin-wave dispersion relation. For small wave vectors, the excitation energy increases and the graphs for different ME-coupling narrow, if the DMI strength is enhanced. This reflects the reduction of the influence of the ME-coupling on the magnetic system, if the DMI enhances. An experimental study on the magnon spectrum in hexagonal multiferroic YMnO$_3$ is carried out in [194].

The temperature dependence of the transverse magnetization is shown in Fig. 6.6. The magnetization decreases with increasing temperature and vanishes continuously at the magnetic phase transition. The effect of the ME-coupling is shown in graph (a). Here the magnetization is enhanced and the phase transition temperature shifts to higher values. A further stabilization of the magnetic phase is observed by the DMI in graph (b). The magnetization increases with an enhanced DMI-coupling strength. The temperature dependence of the pitch of the spiral for different ME-coupling strengths and one DMI is shown in graph (c) and (d), respectively. The pitch of the spiral is determined by the interaction within the investigated system and varies only in a small range, which was reported by experiments [65]. The largest change in the pitch is observed in approaching the magnetic phase transition. Here the polarization of the system reduces and varies the spiral. An agreement with the temperature dependence of the sublattice magnetization for BiFeO$_3$ is found in [195].
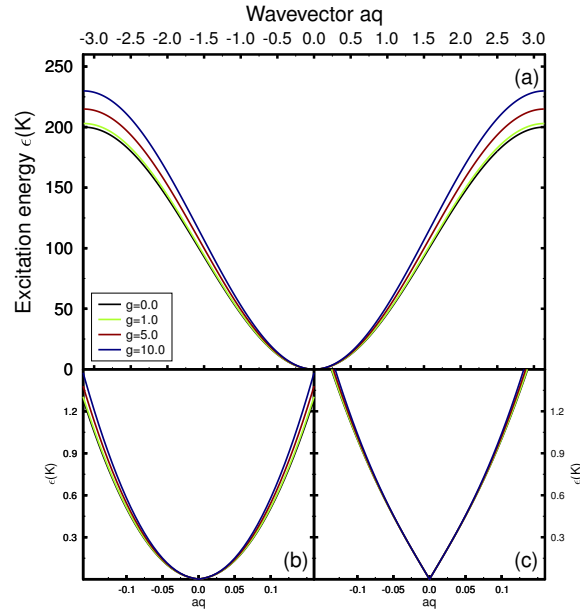
Fig. 6.5.: Magnetic dispersion relation for different strength of magneto-electric coupling. The lower left graph (b) shows the dispersion relation at the Brillouin zone center. In graph (a) and (b) the DMI reads $D^z = 1\,\text{K}$, whereas in graph (c) the dispersion relation for $D^z = 10\,\text{K}$ is plotted.
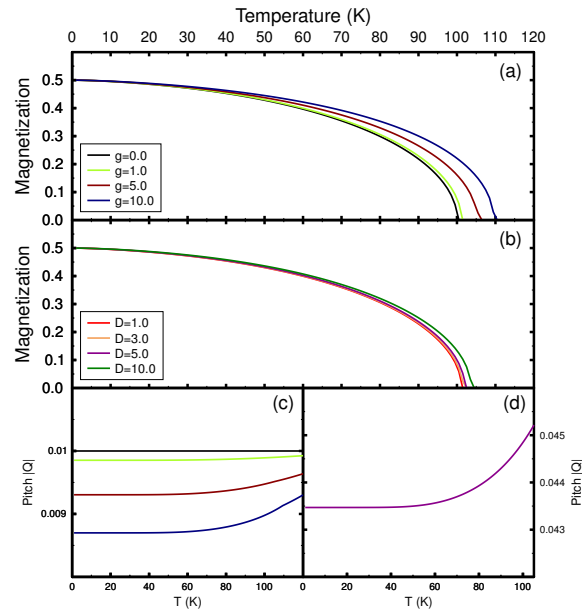

Fig. 6.6.: Temperature dependence of the magnetization pointing along the in-plane quantization axis for different (a) ME-coupling strengths and (b) DMI strengths. The lower left graph (c) shows the temperature dependent pitch for different ME-coupling strengths. The lower right graph (d) shows the pitch for the DMI strength $D^z = 5\,\text{K}$.

7. Summary and Outlook

The work comprises a many-body approach of magnetic, ferroelectric and multiferroic materials. Whereas the main part of the work concerns quantum models, a classical version of the Ising model in a transverse field has been studied, which offers several applications especially the description of order-disorder ferroelectrics. The excitation energy could be calculated above and below the phase transition temperature. Due to the coupling of the system to a bath, the excitations exhibit a finite life-time. The corresponding damping part of the evolution equation has been found under quite general conditions, such as the behavior under time reversal and the structure constants of the underlying Lie group of the spin vectors. The additional part is similar to the so called Gilbert damping in ferromagnets. However, different to the isotropic ferromagnetic case the model is anisotropic resulting in a totally different dynamics. As the consequence the dispersion relation becomes a massive one. Under these conditions also the damping offers another behavior as in magnets. In terms of a multiscale approach, the relevant incoming static quantities such as the polarization are calculated using the microscopic model on a mean-field level.

Ferroelectrics are widely used in many applications, which require sizes down to the nanometer range. At a nanoscale ferroelectricity has emerged as a fertile ground for new physical phenomena. Beside the challenge of the fabrication of structures in the nano region there is an increasing interest in modeling ferroelectric nanostructures. The broad variety of experimental facts about the characterization of ferroelectric nanostructures has to be supplemented by theoretical studies. Because the behavior is obviously determined by the microscopic interaction between the constituents, it seems natural to consider models on that scale.

A microscopic model for the analytical investigation of such thin films and nanoparticles was suggested. The model is an extension of the well established Ising model in a transverse field, which describes quite generic the ordering of functional groups giving rise to ferroelectricity. For this purpose, the Ising model in a transverse field was modified to include effects of surfaces and defects. These properties are manifested within the model by introducing different microscopic coupling parameters for the constituents of the ferroelectric material.

Based on the modified transverse Ising model and a Green's function technique, the damping and the phase transition temperature for ferroelectric thin films with structural defects were calculated for the first time. The dependence on temperature, film thickness and interaction constants was discussed. As a result defect layers in ferroelectric thin films can induce strong changes of the critical temperature of the ferroelectric phase transition due to different interactions in the defect layers. The damping in thin films with defects is always larger in comparison to the corresponding bulk values or to films without defects. Hence, defects are important for the explanation of the large line broadening effects observed experimentally in thin films.

Spherical ferroelectric nanoparticles composed of different shells were analyzed. This number directly corresponds to the particle size. The small size of the materials requires the inclusion of both, bulk and surface interaction. Furthermore, in case of the appearance of defects, an additional coupling strength occurs. Due to the broken translational invariance the Green's function technique was formulated in real space. Taking into account the microscopic parameters (direct coupling and transverse field), the equation of motion method for the Green's function yields the polarization of ferroelectric nanoparticles in dependence of the temperature, the external electric field, possible inherent defect configurations and the particle size. In addition, the temperature and size dependence of the excitation energy and its damping were obtained. The dependence on the particle size is also discussed. The results strongly indicate, that microscopic details of the interaction within the ferroelectric nanoparticles are essential for the macroscopic behavior of quantities such as the hysteresis loop.

In particular, it has been demonstrated that the coercive field is very sensitive to the interaction parameter between functional groups at the surface and between defect shells. Furthermore, the remanent polarization and the Curie temperature change in comparison to the defect-free case. This theoretical result is in accordance with the experimental data offering an variation of the critical temperature, the coercive field and the remanent polarization by the substitution with doping ions. Moreover, two different filling procedures, namely beginning from the surface shell or starting from the central group or/and the first shell were discussed. This asymmetry demonstrates the importance of defect engineering in such materials. The excitation energy decreases and the damping increases strongly with lowering the particle size. Furthermore, the damping of the quasi-soft mode in nanoparticles is significantly larger than that in bulk crystals. The results obtained are in agreement with the experimental data for BTO and PTO small particles.

Magnetic systems of spin-$\frac{1}{2}$ with non-collinear spin structures were investigated in the framework of the temperature dependent two-time retarded Green's function technique.

The inclusion of the asymmetric Dzyaloshinskii-Moriya interaction led to an asymmetric spin-wave dispersion relation in case of conical spirals. The induced asymmetry in the energy is governed by the symmetric Heisenberg exchange coupling, the anisotropy and the antisymmetric DMI. The chirality is represented by the incommensurate wave vector of the spin spiral. From a microscopic point of view the quantum DMI modifies the spectrum of the excitation energy. Recent first principle calculations [184] yield no prediction for the concrete realization of the spiral states favored by the DMI and furthermore, the results are obtained for fixed temperatures.

It was therefore the aim to elucidate the relation between the spin-wave excitation energy and the magnetic alignment of the spins. The progress has been reached by applying a representation of the underlying spin operators with an arbitrary quantization axis. This approach enables the inclusion of a broad class of spin spiral structures. The Hamiltonian includes the isotropic Heisenberg coupling, an anisotropic interaction and the DMI. The spin-wave energy was found by calculating the temperature dependent retarded Green's function matrix. Minimizing the ground state energy yields the direction of the quantization axis. The method enables the inclusion of temperature effects. Here, a reduction of the asymmetry has been observed for increasing temperature. A cycloidal or screw alignment of spins would not lead to an asymmetric dispersion relation. Referring to recent experimental results ruling out longitudinal conical spin spirals the magnetic ordering in these systems has to be of transverse conical type. The asymmetry is calculated for a cubic lattice with nearest neighbor interaction.

Since multiferroic systems are in the focus of recent attention, a systematic microscopic theory of the magneto-electric effect at finite temperatures is presented. The ferroelectric subsystem is described by an Ising model in a transverse field, the magnetic one is characterized by the Heisenberg model with Dzyaloshinskii-Moriya interaction (DMI). The symmetry allowed quartic coupling between both subsystems and the application of a Green's function technique in a dynamical mean field approximation exhibit the calculation of the elementary excitations, which are mutually influenced by the respective other subsystem. A kink in the temperature dependence of different static and dynamic properties has been observed in the vicinity of the magnetic phase transition temperature. The magnetic excitation is a Goldstone mode, while the ferroelectric dispersion relation shows a soft mode-like behavior. The macroscopic polarization and the magnetization were calculated in a broad temperature interval up to the corresponding, well separated, phase transition temperatures (type-I multiferroics). Due to the DMI, the system offers a spiral structure, which was incorporated into the model by using a transformation of the underlying spin operators into a representation without fixed quantization axis. The polarization increases at the magnetic phase transition temperature and is also enhanced

by increasing the ME coupling strength as well as the DMI. Likewise the variation of the spin-wave dispersion relation with the ME coupling strength and the DMI was demonstrated. As a consequence, the macroscopic magnetization oriented in the $x - y$ plane is enhanced with increasing coupling.

Future aspects are the inclusion of other degrees of freedom, such as phonons, to the presented models. Furthermore, the many-particle approach to multiferroics could be extended to multiferroic spinel oxides with conical magnetic structure. Here the magnetization has both, a rotating and a uniform ferromagnetic part. In addition, the magnetic part of the presented approach could be modified to an isotropic Heisenberg model with magneto-strictive coupling of spins due to the competition between nearest and next-nearest neighbor interaction. In this case no antisymmetric terms due to relativistic effects are required.

8. Bibliography

[1]   Hans Schmid. "Multi-ferroic magnetoelectrics" *Ferroelectrics*, 162, pp. 317–338 (1994).

[2]   T Kimura et al. "Magnetic control of ferroelectric polarization" *Nature*, 426, pp. 55–58 (2003).

[3]   I Junger et al. "Green-function theory of the Heisenberg ferromagnet in a magnetic field" *Phys. Rev. B*, 70, p. 104419 (2004).

[4]   Julia M Wesselinowa. "On the theory of thin ferroelectric films" *phys. stat. sol. (b)*, 223, pp. 737–743 (2001).

[5]   Hosho Katsura, Alexander V Balatsky, and Naoto Nagaosa. "Dynamical magneto-electric coupling in helical magnets" *Phys. Rev. Lett.* 98, p. 027203 (2007).

[6]   J Valasek. "Piezo-electric and allied phenomena in Rochelle salt" *Phys. Rev.* 17, p. 475 (1921).

[7]   W Cochran. "Crystal Stability and the Theory of Ferroelectricity" *Phys. Rev. Lett.* 3, pp. 412–414 (1959).

[8]   M Bode et al. "Chiral magnetic order at surfaces driven by inversion asymmetry" *Nature*, 447, pp. 190–193 (2007).

[9]   Kh Zakeri et al. "Asymmetric Spin-Wave Dispersion on Fe(110): Direct Evidence of the Dzyaloshinskii-Moriya Interaction" *Phys. Rev. Lett.* 104, p. 137203 (2010).

[10] SW Tjablikow. *Quantentheoretische Methoden des Magnetismus*. Teubner, Leipzig, 1968.

[11] Manfred Fiebig. "Revival of the magnetoelectric effect" *J. Phys. D: Appl. Phys.* 38, R123–R152 (2005).

[12] Jeroen Van Den Brink and Daniel I Khomskii. "Multiferroicity due to charge ordering" *J. Phys. Condens. Matter*, 20, p. 434217 (2008).

[13] Sang-Wook Cheong and Maxim Mostovoy. "Multiferroics: a magnetic twist for ferroelectricity" *Nat. Mater.* 6, pp. 13–20 (2007).

[14] Daniel Khomskii. "Classifying multiferroics: Mechanisms and effects" *Physics*, 2, pp. 1–8 (2009).

[15] BA Strukov and AP Levanyuk. *Ferroelectric Phenomena in Crystals*. Springer-Verlag, Berlin Heidelberg, 1998.

[16] Karin M Rabe, Charles H Ahn, and Jean-Marc Triscone. *Physics of Ferroelectrics*. Vol. 105. Topics in Applied Physics, 2007, p. 390.

[17] M E Lines and A Glass. *Principles and Applications of Ferroelectrics and Related Materials*. Clarendon Press, Oxford, 2004.

[18] JC Burfoot and G W Taylor. *Polar dielectrics and their applications*. The Macmillian press LTD, 1979.

[19] R Blinc and B Žekš. *Soft Modes in Ferroelectrics and Antiferroelectrics*. North-Holland, Amsterdam, 1974.

[20] WJ Merz. "The Electric and Optical Behavior of $BaTiO_3$ Single-Domain Crystals" *Phys. Rev.* 76, pp. 1221–1225 (1949).

[21] P W Anderson. "Proceedings of the Conference on The Physics of Dielectrics" *Academy of Science, USSR, Moscow*, p. 290 (1958).

[22] M Lezaic. *Spintronics - From GMR to Quantum Information*. 40th IFF Spring School, 2009.

[23] M T Dove. "Theory of displacive phase transitions in minerals" *American Mineralogist*, 82, p. 213 (1997).

[24] PS Halasyamani and KR Poeppelmeier. "Noncentrosymmetric oxides" *Chem Mater*, 10, pp. 2753–2769 (1998).

[25] IB Bersuker. "Modern aspects of the Jahn-Teller effect theory and applications to molecular problems" *Chem Rev*, 101, pp. 1067–1114 (2001).

[26] J Slater. "Theory of the Transition in KH_2PO_4" *J. Chem. Phys.* 9, pp. 16–33 (1941).

[27] Qing Zhang et al. "Ab initio study of the electronic and structural properties of the ferroelectric transition in KH_2PO_4" *Phys. Rev. B*, 65, p. 024108 (2001).

[28] S Koval et al. "Ferroelectricity and isotope effects in hydrogen-bonded KDP crystals" *Phys. Rev. Lett.* 89, p. 187602 (2002).

[29] GE Bacon and RS Pease. "A neutron-diffraction study of the ferroelectric transition of potassium dihydrogen phosphate" *Proc R Soc Lon Ser-A*, 230, pp. 359–381 (1955).

[30] H Sugimoto and S Ikeda. "Isotope Effects in Hydrogen-Bonded Crystal KH_2PO_4" *Phys. Rev. Lett.* 67, pp. 1306–1309 (1991).

[31] A Bussmann-Holder and KH Michel. "Bond geometry and phase transition mechanism of H-bonded ferroelectrics" *Phys. Rev. Lett.* 80, pp. 2173–2176 (1998).

[32] R Blinc. "On the isotopic effects in the ferroelectric behaviour of crystals with short hydrogen bonds" *J Phys Chem Solids*, 13, pp. 204–211 (1960).

[33] W Heisenberg. "Zur Theorie des Ferromagnetismus" *Zeitschrift für Physik A Hadrons and Nuclei*, 49, pp. 619–636 (1928).

[34] F Bloch. "Bemerkung zur Elektronentheorie des Ferromagnetismus und der elektrischen Leitfähigkeit" *Zeitschrift für Physik A Hadrons and Nuclei*, 57, pp. 545–555 (1929).

[35] W Nolting and A Ramakanth. *Quantum Theory of Magnetism.* Springer-Verlag, Berlin Heidelberg, 2009.

[36] Noberto Majlis. *The Quantum Theory of Magnetism (2nd Edition).* World Scientific Publishing Co. Pte. Ltd., 2007.

[37] Ralph Skomski. *Simple Models of Magnetism.* Oxford University Press, 2008.

[38] K H Fischer and J A Hertz. *Spin Glasses (Cambridge Studies in Magnetism).* Cambridge University Press, 1993.

[39] I. E Dzyaloshinskii. "A thermodynamic theory of "weak" ferromagnetism of antiferromagnetics" *J Phys Chem Solids*, 4, pp. 241–255 (1958).

[40] T Moriya. "New Mechanism of Anisotropic Superexchange Interaction" *Phys. Rev. Lett.* 4, pp. 228–230 (1960).

[41] N Konstantinidis and D Coffey. "Magnetic anisotropy in the molecular complex V_{15}" *Phys. Rev. B*, 66, p. 174426 (2002).

[42] A Zheludev et al. "Experimental evidence for Kaplan-Shekhtman-Entin-Wohlman-Aharony interactions in $Ba_2CuGe_2O_7$" *Phys. Rev. Lett.* 81, pp. 5410–5413 (1998).

[43] M Uchida et al. "Real-space observation of helical spin order" *Science*, 311, pp. 359–361 (2006).

[44] J Villain. "La structure des substances magnetiques" *J Phys Chem Solids*, 11, pp. 303–309 (1959).

[45] T Kaplan. "Classical Theory of Spin Configurations in the Cubic Spinel" *Phys. Rev.* 119, p. 1460 (1960).

[46] T Nagamiya. "Modification of Spin Screw Structure due to Anisotropy Energy and Applied Magnetic Field" *J. Appl. Phys.* 33, p. 1029 (1962).

[47] D Lyons et al. "Classical Theory of the Ground Spin-State in Cubic Spinels" *Phys. Rev.* 126, p. 540 (1962).

[48] B Cooper et al. "Theory of Magnetic Resonance in the Heavy Rare-Earth Metals" *Phys. Rev.* 127, p. 57 (1962).

[49] T Nagamiya. "Development of the Theory of Helical Spin Ordering" *J. Appl. Phys.* 39, pp. 373–379 (1968).

[50] I. E Dzyaloshinskii. "On the magneto-electrical effect in antiferromagnets" *Sov Phys Jetp-Ussr*, 10, pp. 628–629 (1960).

[51] DN Astrov. "The magnetoelectric effect in antiferromagnetics" *Sov Phys Jetp-Ussr*, 11, pp. 708–709 (1960).

[52] J Wang et al. "Epitaxial $BiFeO_3$ multiferroic thin film heterostructures" *Science*, 299, pp. 1719–1722 (2003).

[53] N Hur et al. "Electric polarization reversal and memory in a multiferroic material induced by magnetic fields" *Nature*, 429, pp. 392–395 (2004).

[54] Daniel I Khomskii. "Multiferroics: Different ways to combine magnetism and ferroelectricity" *J Magn Magn Mater*, 306, pp. 1–8 (2006).

[55] W Eerenstein, N. D Mathur, and James F Scott. "Multiferroic and magnetoelectric materials" *Nature*, 442, pp. 759–765 (2006).

[56] Silvia Picozzi and Claude Ederer. "First Principles Studies of Multiferroic Materials" *SCIENTIFIC HIGHLIGHT OF THE MONTH*, pp. 1–37 (2009).

[57] K. F Wang, J. M Liu, and Z. F Ren. "Multiferroicity: the coupling between magnetic and polarization orders" *Adv. Phys.* 58, pp. 321–448 (2009).

[58] T Zhao et al. "Electrical control of antiferromagnetic domains in multiferroic $BiFeO_3$ films at room temperature" *Nat. Mater.* 5, pp. 823–829 (2006).

[59] Claude Ederer and Nicola A Spaldin. "Weak ferromagnetism and magnetoelectric coupling in bismuth ferrite" *Phys. Rev. B*, 71, 060401R (2005).

[60] S V Kiselev, R P Ozerov, and G S Zhdanov. "Detection of magnetic order in ferroelectric $BiFeO_3$ by neutron diffraction" *Sov. Phys. Dokl.* 7, pp. 742–744 (1963).

[61] JR Teague, R Gerson, and WJ James. "Dielectric Hysteresis in Single Crystal $BiFeO_3$" *Solid State Commun.* 8, p. 1073 (1970).

[62] C Michel et al. "The Atomic Structure of $BiFeO_3$" *Solid State Commun.* 7, pp. 701–704 (1969).

[63] F Kubel and Hans Schmid. "Structure of a Ferroelectric and Ferroelastic Monodomain Crystal of the Perovskite $BiFeO_3$" *Acta Crystallogr B*, 46, pp. 698–702 (1990).

[64] JB Neaton et al. "First-principles study of spontaneous polarization in multiferroic $BiFeO_3$" *Phys. Rev. B*, 71, p. 014113 (2005).

[65] I Sosnowska, T Peterlin-Neumaier, and E Steichele. "Spiral magnetic ordering in bismuth ferrite" *J. Phys. C: Solid State Phys.* 15, pp. 4835–4846 (1982).

[66] I Sosnowska et al. "Crystal structure and spiral magnetic ordering of $BiFeO_3$ doped with manganese" *Applied Physics A: Materials Science & Processing*, 74, s1040–s1042 (2002).

[67] YF Popov et al. "Linear magnetoelectric effect and phase-transitions in bismuth ferrite, $BiFeO_3$" *Jetp Lett+*, 57, pp. 69–73 (1993).

[68] R Ramesh and Nicola A Spaldin. "Multiferroics: progress and prospects in thin films" *Nat. Mater.* 6, pp. 21–29 (2007).

[69] BB Van Aken et al. "The origin of ferroelectricity in magnetoelectric YMnO3" *Nat. Mater.* 3, pp. 164–170 (2004).

[70] Maxim Mostovoy. "Ferroelectricity in Spiral Magnets" *Phys. Rev. Lett.* 96, p. 067601 (2006).

[71] Y. J Choi et al. "Ferroelectricity in an Ising chain magnet" *Phys. Rev. Lett.* 100, p. 047601 (2008).

[72] L. C Chapon et al. "Ferroelectricity Induced by Acentric Spin-Density Waves in YMn_2O_5" *Phys. Rev. Lett.* 96, p. 097601 (2006).

[73] A. B Sushkov et al. "Electromagnons in multiferroic RMn_2O_5 compounds and their microscopic origin" *J. Phys. Condens. Matter*, 20, p. 434210 (2008).

[74] Wolfgang Nolting. *Quantentheorie des Magnetismus (Band 2)*. B B Teubner Stuttgart, 1986, p. 349.

[75] NN Bogolyubov and SV Tyablikov *Dokl. Akad. Nauk SSSR*, 126, p. 539 (1959).

[76] T Matsubara. "A new approach to quantum-statistical mechanics" *Prog Theor Phys*, 14, pp. 351–378 (1955).

[77] DN Zubarev. "Two-time Green Functions in Statistical Physics" *Usp Fiz Nauk+*, 71, pp. 71–116 (1960).

[78] W Gasser, E Heiner, and K Elk. *Greensche Funktionen in Festkörper- und Vielteilchenphysik*. WILEY-VCH, 2001.

[79]   E N Economou. *Green's Functions in Quantum Physics.* Springer Series in Solid-State Science, Spinger Berlin, 2006.

[80]   S Doniach and E.H.Sondheimer. "Green's functions for solid state physicists" *Imperial College Press*, (1998).

[81]   R Kubo. "Statistical-Mechanical Theory of Irreversible Processes 1. General Theory and Simple Applications to Magnetic and Conduction Problems" *J Phys Soc Jpn*, 12, pp. 570–586 (1957).

[82]   R Blinc and B Žekš. "Dynamics of order-disorder-type ferroelectrics and anti-ferroelectrics" *Adv. Phys.* 21, pp. 693–757 (1972).

[83]   PG de Gennes. "Collective motions of hydrogen bonds" *Solid State Commun.* 1, pp. 132–137 (1963).

[84]   R Pirc and R Blinc. "Off-center Ti model of barium titanate" *Phys. Rev. B*, 70, p. 134107 (2004).

[85]   HX Cao and ZY Li. "Thermodynamic properties of temperature graded ferroelectric film" *J. Phys. Condens. Matter*, 15, pp. 6301–6310 (2003).

[86]   M Lambert and R Comes. "Chain Structure and Phase Transition of $BaTiO_3$ and $KNbO_3$" *Solid State Commun.* 7, p. 305 (1969).

[87]   IB Bersuker. "On origin of ferroelectricity in perovskite-type crystals" *Physics Letters*, 20, p. 589 (1966).

[88]   YL Wang and BR Cooper. "Collective Excitations and Magnetic Ordering in Materials with Singlet Crystal-Field Ground State" *Phys. Rev.* 172, p. 539 (1968).

[89]   J Villain and S Stamenkovic. "Atomic Motion in Hydrogen-Bond Ferroelectrics" *Phys Status Solidi*, 15, p. 585 (1966).

[90]   P Ghosez and J Junquera. "First-Principles Modeling of Ferroelectric Oxides Nanostructures" *Handbook of Theoretical and Computational Nanotechnology*, 134, pp. 1–149 (2006).

[91]   Julia M Wesselinowa and MS Marinov. "On the Theory of 1st-Order Phase-Transition in Order-Disorder Ferroelectrics" *Int J Mod Phys B*, 6, pp. 1181–1192 (1992).

[92]   Julia M Wesselinowa. "Properties of ferroelectric thin films with a first-order phase transitions" *Solid State Commun.* 121, pp. 89–92 (2002).

[93]   DS Gaunt and C Domb. "Equation of state of Ising model near the critical point" *J. Phys. C: Solid State Phys.* 3, p. 1442 (1970).

[94] RJ Elliott and C Wood. "Ising model with a transverse field –I High temperature expansion" *J. Phys. C: Solid State Phys.* 4, p. 2359 (1971).

[95] P Pfeuty and RJ Elliott. "Ising Model with a Transverse Field .2. Ground State Properties" *J. Phys. C: Solid State Phys.* 4, p. 2370 (1971).

[96] P Pfeuty. "One-Dimensional Ising Model with a Transverse Field" *Ann Phys-New York*, 57, p. 79 (1970).

[97] S Katsura. "Statistical Mechanics of the Anisotropic Linear Heisenberg Model" *Phys. Rev.* 127, p. 1508 (1962).

[98] M Suzuki. "Equivalence Of Two-Dimensional Ising Model To Ground State Of Linear XY-Model" *Phys. Lett. A*, A 34, p. 94 (1971).

[99] R Brout, KA Muller, and H Thomas. "Tunnelling and Collective Excitations in a Microscopic Model of Ferroelectricity" *Solid State Commun.* 4, p. 507 (1966).

[100] ME Fisher. "Perpendicular Susceptibility of the Ising Model" *J Math Phys*, 4, p. 124 (1963).

[101] RB Stinchcombe. "Thermal and magnetic properties of the transverse Ising model" *J. Phys. C: Solid State Phys.* 6, pp. 2507–2524 (1973).

[102] RB Stinchcombe. "Ising model in a transverse field .2. Spectral functions and damping" *J. Phys. C: Solid State Phys.* 6, pp. 2484–2506 (1973).

[103] A Kuehnel, S Wendt, and Julia M Wesselinowa. "Dynamic Behaviour of the Ising model in a Transverse Field" *phys. stat. sol. (b)*, 84, pp. 653–664 (1977).

[104] Julia M Wesselinowa. "The Dielectric Function and Reflectivity in KDP-Type Ferroelectrics" *phys. stat. sol. (b)*, 160, pp. 697–704 (1990).

[105] Julia M Wesselinowa. "Phase-transitions of $PbHPO_4$- and $PbDPO_4$-type ferro-electrics investigated with a Green's-function technique" *Phys. Rev. B*, 49, pp. 3098–3103 (1994).

[106] Julia M Wesselinowa, AT Apostolov, and A Filipova. "Anharmonic effects in potassium-dihydrogen-phosphate-type ferroelectrics" *Phys. Rev. B*, 50, pp. 5899–5904 (1994).

[107] Julia M Wesselinowa and AT Apostolov. "On the origin of the central peak in hydrogen-bonded ferroelectrics" *Solid State Commun.* 101, pp. 343–346 (1997).

[108] Julia M Wesselinowa. "Damping of the Transverse and Longitudinal Excitations of the Ising-Model in a Transverse Field" *phys. stat. sol. (b)*, 121, pp. 317–327 (1984).

[109] HB Callen. "Green Function Theory of Ferromagnetism" *Phys. Rev.* 130, p. 890 (1963).

[110] V I Lymar and Yu G Rudoi. "Spectrum and correlation functions of an anisotropic heisenberg antiferromagnet. I. Antiferromagnetic phase in the generalized Hartree–Fock approximation" *Theor. Math. Phys.* 21, p. 86 (1974).

[111] Huai-Yu Wang et al. "Many-body Green's function theory of ferromagnetic Heisenberg systems with single-ion anisotropies in more than one direction" *Phys. Rev. B*, 70, p. 134424 (2004).

[112] F Bloch. "Zur Theorie des Ferromagnetismus" *Zeitschrift für Physik A Hadrons and Nuclei*, 61, pp. 206–219 (1930).

[113] Yu. A Tserkovnikov. "Decoupling of chains of equations for two-time Green's functions" *Theor. Math. Phys.* 7, pp. 250–261 (1971).

[114] Yu G Rudoi and Yu. A Tserkovnikov. "One-particle Green's function in the anisotropic Heisenberg model IV. Spectrum and phase transition in the presence of a transverse field" *Theor. Math. Phys.* 25, pp. 196–212 (1975).

[115] L D Landau, E M Lifshitz, and L P Pitaevski. *Statistical Physics, Part 2.* Pergamon, Oxford, 1980.

[116] Y Tserkovnyak et al. "Nonlocal magnetization dynamics in ferromagnetic heterostructures" *Rev. Mod. Phys.* 77, pp. 1375–1421 (2005).

[117] Steffen Trimper, Thomas Michael, and Julia M Wesselinowa. "Ferroelectric soft modes and Gilbert damping" *Phys. Rev. B*, 76, p. 094108 (2007).

[118] RB Stinchcombe. "Ising model in a transverse field .1. Basic theory" *J. Phys. C: Solid State Phys.* 6, pp. 2459–2483 (1973).

[119] Julia M Wesselinowa and St Kovachev. "Hardening and softening of soft phonon modes in ferroelectric thin films" *Phys. Rev. B*, 75, p. 045411 (2007).

[120] PC Hohenberg and BI Halperin. "Theory of Dynamic Critical Phenomena" *Rev. Mod. Phys.* 49, pp. 435–479 (1977).

[121] KD Usadel. "Temperature-dependent dynamical behavior of nanoparticles as probed by ferromagnetic resonance using Landau-Lifshitz-Gilbert dynamics in a classical spin model" *Phys. Rev. B*, 73, p. 212405 (2006).

[122] S. I Denisov, T. V Lyutyy, and P Hanggi. "Magnetization of nanoparticle systems in a rotating magnetic field" *Phys. Rev. Lett.* 97, p. 227202 (2006).

[123] Julia M Wesselinowa. "Dynamical properties of thin ferroelectric films described by the transverse Ising model" *phys. stat. sol. (b)*, 231, pp. 187–191 (2002).

[124] Julia M Wesselinowa and Steffen Trimper. "Layer polarizations and dielectric susceptibilities of antiferroelectric thin films" *Mod Phys Lett B*, 17, pp. 1343–1347 (2003).

[125] Julia M Wesselinowa and Steffen Trimper. "Central peak in the excitation spectra of thin ferroelectric films" *Phys. Rev. B*, 69, p. 024105 (2004).

[126] Julia M Wesselinowa and Steffen Trimper. "Thickness dependence of the dielectric function of ferroelectric thin films" *phys. stat. sol. (b)*, 241, pp. 1141–1148 (2004).

[127] Julia M Wesselinowa. "Effects of spin-phonon interaction on the dynamical properties of thin ferroelectric films" *J. Phys. Condens. Matter*, 17, pp. 3001–3014 (2005).

[128] Julia M Wesselinowa. "Dielectric function of antiferroelectric thin films" *phys. stat. sol. (b)*, 242, pp. 1528–1536 (2005).

[129] Julia M Wesselinowa, Steffen Trimper, and Knud Zabrocki. "Impact of layer defects in ferroelectric thin films" *J. Phys. Condens. Matter*, 17, pp. 4687–4699 (2005).

[130] Julia M Wesselinowa et al. "Influence of layer defects on the damping in ferroelectric thin films" *Phys. Lett. A*, 348, pp. 397–404 (2006).

[131] Julia M Wesselinowa and Al. B Dimitrov. "Influence of substrates on the statical and dynamical properties of ferroelectric thin films" *phys. stat. sol. (b)*, 244, pp. 2242–2253 (2007).

[132] P Fröbrich and P. J Kuntz. "The treatment of zero eigenvalues of the matrix governing the equations of motion in many-body Green function theory" *J. Phys. Condens. Matter*, 17, pp. 1167–1191 (2005).

[133] I Taguchi et al. "Raman-scattering from $PbTiO_3$ thin-films prepared on silicon substrates by radio-frequency sputtering and thermal-treatment" *J. Appl. Phys.* 73, pp. 394–399 (1993).

[134] DS Fu et al. "Phonon mode behaviours of $PbTiO_3$ thin films deposited on Pt/Si substrates" *J. Phys. Condens. Matter*, 12, pp. 399–414 (2000).

[135] Kenji Ishikawa, K Yoshikawa, and N Okada. "Size effect on the ferroelectric phase transition in $PbTiO_3$ particles" *Phys. Rev. B*, 37, pp. 5852–5855 (1988).

[136] Xiaorong Cheng and Mingrong Shen. "Enhanced spontaneous polarization in Sr and Ca co-doped $BaTiO_3$ ceramics" *Solid State Commun.* 141, pp. 587–590 (2007).

[137] TY Kim and HM Jang. "B-site vacancy as the origin of spontaneous normal-to-relaxor ferroelectric transitions in La-modified $PbTiO_3$" *Appl. Phys. Lett.* 77, pp. 3824–3826 (2000).

[138] SB Majumder et al. "Effect of rare earth doping on sol-gel derived PZT thin films" *Ferroelectrics Lett*, 28, pp. 85–92 (2001).

[139] Y Shimakawa et al. "Crystal and electronic structures of $Bi_{4-x}La_xTi_3O_{12}$ ferroelectric materials" *Appl. Phys. Lett.* 79, pp. 2791–2793 (2001).

[140] B Su and TW Button. "Microstructure and dielectric properties of Mg-doped barium strontium titanate ceramics" *J. Appl. Phys.* 95, pp. 1382–1385 (2004).

[141] P Victor, R Ranjith, and SB Krupanidhi. "Normal ferroelectric to relaxor behavior in laser ablated Ca-doped barium titanate thin films" *J. Appl. Phys.* 94, pp. 7702–7709 (2003).

[142] Yuji Noguchi, Masaru Miyayama, and Tetsuichi Kudo. "Direct evidence of A-site-deficient strontium bismuth tantalate and its enhanced ferroelectric properties" *Phys. Rev. B*, 63, p. 214102 (2001).

[143] Y Shimakawa et al. "Crystal structures and ferroelectric properties of $SrBi_2Ta_2O_9$ and $Sr_{0.8}Bi_{2.2}Ta_2O_9$" *Appl. Phys. Lett.* 74, pp. 1904–1906 (1999).

[144] Y Shimakawa et al. "Crystal structure and ferroelectric properties of $ABi_2Ta_2O_9$ (A = Ca, Sr, and Ba)" *Phys. Rev. B*, 61, pp. 6559–6564 (2000).

[145] Sining Yun et al. "Dielectric properties Ca-substituted barium strontium titanate ferroelectric ceramics" *Solid State Commun.* 143, pp. 461–465 (2007).

[146] RK Zheng et al. "Effects of Ca doping on the Curie temperature, structural, dielectric, and elastic properties of $Ba_{0.4}Sr_{0.6-x}Ca_xTiO_3$ ($0 <= x <= 0.3$) perovskites" *J. Appl. Phys.* 98, p. 084108 (2005).

[147] A Boulle et al. "A new method for the determination of strain profiles in epitaxic thin films using X-ray diffraction" *J Appl Crystallogr*, 36, pp. 1424–1431 (2003).

[148] Thomas Michael, Steffen Trimper, and Julia M Wesselinowa. "Size effects on static and dynamic properties of ferroelectric nanoparticles" *Phys. Rev. B*, 76, p. 094107 (2007).

[149] Thomas Michael, Steffen Trimper, and Julia M Wesselinowa. "Size and doping effects on the coercive field of ferroelectric nanoparticles: A microscopic model" *Phys. Rev. B*, 74, p. 214113 (2006).

[150] Tomoya Ohno et al. "Size Effect for $Ba(Zr_xTi_{1-x})O_3$ (x = 0.05) Nano-Particles" *Ferroelectrics*, 337, pp. 25–32 (2006).

[151] Wei-Lie Zhong et al. "Phase transition in $PbTiO_3$ ultrafine particles of different sizes" *J. Phys. Condens. Matter*, 5, pp. 2619–2624 (1993).

[152] S Chattopadhyay et al. "Size-induced diffuse phase-transition in the nanocrystalline ferroelectric $PbTiO_3$" *Phys. Rev. B*, 52, pp. 13177–13183 (1995).

[153] V Fridkin. "Mean-field theory about the critical size in ferroelectricity" *Crystallography Reports*, 54, pp. 917–919 (2009).

[154] Daniel McCauley, Robert E Newnham, and Clive A Randall. "Intrinsic Size Effects in a Barium Titanate Glass-Ceramic" *J. Am. Ceram. Soc.* 81, pp. 979–987 (1998).

[155] Stefan Schlag and Hans-Friedrich Eicke. "Size Driven Phase Transition in Nanocrystalline $BaTiO_3$" *Solid State Commun.* 91, pp. 883–887 (1994).

[156] EV Colla, AV Fokin, and YA Kumzerov. "Ferroelectrics properties of nanosize KDP particles" *Solid State Commun.* 103, pp. 127–130 (1997).

[157] James F Scott et al. "Raman-spectroscopy of submicron KNO_3 films" *Phys. Rev. B*, 35, pp. 4044–4051 (1987).

[158] L Baudry and J Tournier. "Lattice model for ferroelectric thin film materials including surface effects: Investigation on the "depolarizing" field properties" *J. Appl. Phys.* 90, pp. 1442–1454 (2001).

[159] J Wang and TY Zhang. "Size effects in epitaxial ferroelectric islands and thin films" *Phys. Rev. B*, 73, p. 144107 (2006).

[160] YS Kim et al. "Critical thickness of ultrathin ferroelectric $BaTiO_3$ films" *Appl. Phys. Lett.* 86, p. 102907 (2005).

[161] SB Ren et al. "Size-related ferroelectric-domain-structure transition in a polycrystalline $PbTiO_3$ thin film" *Phys. Rev. B*, 54, R14337–R14340 (1996).

[162] NA Pertsev et al. "Coercive field of ultrathin $Pb(Zr_{0.52}Ti_{0.48})O_3$ epitaxial films" *Appl. Phys. Lett.* 83, pp. 3356–3358 (2003).

[163] V Nagarajan et al. "Size effects in ultrathin epitaxial ferroelectric heterostructures" *Appl. Phys. Lett.* 84, p. 5225 (2004).

[164] DS Fu, Hisao Suzuki, and Kenji Ishikawa. "Size-induced phase transition in $PbTiO_3$ nanocrystals: Raman scattering study" *Phys. Rev. B*, 62, pp. 3125–3129 (2000).

[165] G Burns and BA Scott. "Raman Studies of Underdamped Soft Modes in $PbTiO_3$" *Phys. Rev. Lett.* 25, pp. 167–170 (1970).

[166] S Wada et al. "Dielectric Properties of nm-Sized Barium Titanate Fine Particles and Their Size Dependence" *Advances in Electronic Ceramic Materials*, 26, p. 89 (2005).

[167] T Yu et al. "Size effect on the ferroelectric phase transition in $SrBi_2Ta_2O_9$ nanoparticles" *J. Appl. Phys.* 94, pp. 618–620 (2003).

[168] CB Parker, JP Maria, and AI Kingon. "Temperature and thickness dependent permittivity of $(Ba,Sr)TiO_3$ thin films" *Appl. Phys. Lett.* 81, pp. 340–342 (2002).

[169] D. A Tenne et al. "Soft phonon modes in $Ba_{0.5}Sr_{0.5}TiO_3$ thin films studied by Raman spectroscopy" *Appl. Phys. Lett.* 79, pp. 3836–3838 (2001).

[170] Thomas Michael, Steffen Trimper, and Julia M Wesselinowa. "Impact of Defects on the Properties of Ferroelectric Nanoparticles" *Ferroelectrics*, 363, pp. 110–119 (2008).

[171] Yuji Noguchi et al. "Defect engineering for control of polarization properties in $SrBi_2Ta_2O_9$" *Jpn. J. Appl. Phys.* 41, pp. 7062–7075 (2002).

[172] K Ramam and V Miguel. "Microstructure, dielectric and ferroelectric characterization of Ba doped PLZT ceramics" *Eur. Phys. J. Appl. Phys.* 35, pp. 43–47 (2006).

[173] M Plonska, D Czekaj, and Z Surowiak. "Application of the sol-gel method to the synthesis of ferroelectric nanopowders $(Pb_{1-x}La_x)(Zr_{0.65}Ti_{0.35})_{1-0.25x}O_3$, $0.06 \leq x \leq 0.1$" *Mater. Science*, 21, pp. 431–437 (2003).

[174] K Iijima et al. "Epitaxial-growth and the crystallographic, dielectric, and pyroelectric properties of lanthanum-modified lead titanate thin-films" *J. Appl. Phys.* 60, pp. 2914–2919 (1986).

[175] M Tyunina et al. "Relaxor behavior of pulsed laser deposited ferroelectric $(Pb_{1-x}La_x)(Zr_{0.65}Ti_{0.35})O_3$ films" *J. Appl. Phys.* 84, pp. 6800–6810 (1998).

[176] T Sakai et al. "Effect of La substitution on electrical properties of highly oriented $Bi_4Ti_3O_{12}$ films prepared by metalorganic chemical vapor deposition" *Jpn. J. Appl. Phys.* 42, pp. 166–169 (2003).

[177] R. R Das et al. "Influence of Ca on structural and ferroelectric properties of laser ablated $SrBi_2Ta_2O_9$ thin films" *Jpn. J. Appl. Phys.* 42, pp. 162–165 (2003).

[178] JF Meng et al. "Investigations of the Phase Transition in Nanocrystalline $Pb_{1-x}La_xTiO_3$ System" *Solid State Commun.* 90, pp. 643–645 (1994).

[179] S Yakovlev et al. "Structural and dielectric properties of Er substituted sol-gel fabricated $PbTiO_3$ thin films" *Appl. Phys. A*, 82, pp. 727–731 (2006).

[180] T Michael and S Trimper. "Asymmetric Dispersion Relation in Spin Spiral Structures" *submitted to PRB*, (2010).

[181] T Kaplan. "Some Effects of Anisotropy on Spiral Spin-Configurations with Application to Rare-Earth Metals" *Phys. Rev.* 124, p. 329 (1961).

[182] B Cooper and R Elliott. "Spin-Wave Theory of Magnetic Resonance in Spiral Spin Structures: Effect of an Applied Field" *Phys. Rev.* 131, p. 1043 (1963).

[183] V I Lymar and Yu G Rudoi. "Spectrum and correlation-functions of an anisotropic Heisenberg anti-ferromagnet .IV. Model of easy plane type with allowance for Dzyaloshinskii interaction" *Theor. Math. Phys.* 34, pp. 137–147 (1978).

[184] L Udvardi and L Szunyogh. "Chiral Asymmetry of the Spin-Wave Spectra in Ultrathin Magnetic Films" *Phys. Rev. Lett.* 102, p. 207204 (2009).

[185] R Elliott and R Lange. "Theorem on Spin Waves in Helical Spin Structures Adapted from the Goldstone Theorem" *Phys. Rev.* 152, p. 235 (1966).

[186] Jun-Ichiro Kishine and A Ovchinnikov. "Theory of spin resonance in a chiral helimagnet" *Phys. Rev. B*, 79, p. 220405 (2009).

[187] I.M Sosnowska. "Neutron scattering studies of $BiFeO_3$ multiferroics: a review for microscopists" *Journal of Microscopy*, 236, pp. 109–114 (2009).

[188] T Kimura et al. "Magnetocapacitance effect in multiferroic $BiMnO_3$" *Phys. Rev. B*, 67, p. 180401 (2003).

[189] H Katsura, Naoto Nagaosa, and Alexander V Balatsky. "Spin current and magnetoelectric effect in noncollinear magnets" *Phys. Rev. Lett.* 95, p. 057205 (2005).

[190] C Zhong. "The coupling effect between ferroelectric and frustrated antiferromagnetic ordering in hexagonal ferroelectromagnet" *Solid State Commun.* 128, pp. 449–453 (2003).

[191] P Rovillain et al. "Polar phonons and spin excitations coupling in multiferroic $BiFeO_3$ crystals" *Phys. Rev. B*, 79, 180411(R) (2009).

[192] R Haumont et al. "Phonon anomalies and the ferroelectric phase transition in multiferroic $BiFeO_3$" *Phys. Rev. B*, 73, p. 132101 (2006).

[193] Julia M Wesselinowa and St Kovachev. "Static and dynamic properties of hexagonal multiferroic $RMnO_3$ compounds" *J. Appl. Phys.* 102, p. 043911 (2007).

[194] S Petit et al. "Spin phonon coupling in hexagonal multiferroic $YMnO_3$" *Phys. Rev. Lett.* 99, p. 266604 (2007).

[195] P Fischer et al. "Temperature dependence of the crystal and magnetic structures of $BiFeO_3$" *J. Phys. C: Solid State Phys.* 13, pp. 1931–1940 (1980).

List of publications

- J. Henk, P. Bose, T. Michael, P. Bruno. Spin motion of photoelectrons. Phys. Rev. B, **68**, 052403 (2003)

- J. Henk, T. Michael, P. Bose, P. Bruno. Photoemission approach to spin motion in electron transmission through magnetic films. Surface Science, **566-568**, 252-255 (2004)

- T. Michael, S. Trimper, M. Schulz. Glauber model in a quantum representation. Phys. Rev. E, **73**, 062101 (2006)

- J. M. Wesselinowa, T. Michael, S. Trimper, K. Zabrocki. Influence of layer defects on the damping in ferroelectric thin films. Phys. Lett. A, **348**, 397-404 (2006)

- T. Michael, S. Trimper, J. M. Wesselinowa. Size and doping effects on the coercive field of ferroelectric nanoparticles: A microscopic model. Phys. Rev. B, **74**, 214113 (2006)

- S. Trimper, T. Michael, J. M. Wesselinowa. Ferroelectric soft modes and Gilbert damping. Phys. Rev. B, **76**, 094108 (2007)

- T. Michael, S. Trimper, J. M. Wesselinowa. Size effects on static and dynamic properties of ferroelectric nanoparticles. Phys. Rev. B, **76**, 094107 (2007)

- T. Michael, S. Trimper, J. M. Wesselinowa. Impact of Defects on the Properties of Ferroelectric Nanoparticles. Ferroelectrics, **363**, 110-119 (2008)

- J. M. Wesselinowa, T. Michael, S. Trimper. Ferroelectric Nanoparticles. Handbook of Nanophysics (2010); accepted

- T. Michael and S. Trimper. Asymmetric Dispersion Relation in Spin Spiral Structures, submitted to Phys. Rev. B (R)

A. Appendix

Fourier transformation

$$b_{\mathbf{k}} = \frac{1}{\sqrt{N}} \sum_{\mathbf{f}} b_{\mathbf{f}} e^{-i\mathbf{k}\mathbf{f}}, \quad b_{\mathbf{k}}^{\dagger} = \frac{1}{\sqrt{N}} \sum_{\mathbf{f}} b_{\mathbf{f}}^{\dagger} e^{i\mathbf{k}\mathbf{f}}, \quad \delta_{\mathbf{k},0} = \frac{1}{N} \sum_{\mathbf{f}} e^{-i\mathbf{k}\mathbf{f}} \tag{A.1}$$

$$b_{\mathbf{f}} = \frac{1}{\sqrt{N}} \sum_{\mathbf{k}} b_{\mathbf{k}} e^{i\mathbf{k}\mathbf{f}}, \quad b_{\mathbf{f}}^{\dagger} = \frac{1}{\sqrt{N}} \sum_{\mathbf{k}} b_{k}^{\dagger} e^{-i\mathbf{k}\mathbf{f}}, \quad \delta_{\mathbf{f},0} = \frac{1}{N} \sum_{\mathbf{f}} e^{i\mathbf{k}\mathbf{f}} \tag{A.2}$$

$$\frac{1}{N} \sum_{\mathbf{k}} J_{\mathbf{k}} e^{i\mathbf{k}\mathbf{f}} = J_{\mathbf{f}}, \quad \sum_{\mathbf{f}} J_{\mathbf{f}} e^{-i\mathbf{f}\mathbf{k}} = J_{\mathbf{k}} \tag{A.3}$$

Corresponding expression for thin films calculations

$$k_n = J_b \langle \sigma_n \rangle \sin^2 \theta_n, \qquad n = 1, ..., N,$$

$$V_1 = 2\Omega_s \sin \theta_1 + \frac{1}{2} \langle \sigma_1 \rangle J_s \cos^2 \theta_1 - \frac{\langle \sigma_1 \rangle J_s}{4} \sin^2 \theta_1 \gamma(\mathbf{k}_{\parallel}) + J_b \langle \sigma_2 \rangle \cos^2 \theta_2,$$

$$V_2 = 2\Omega_b \sin \theta_2 + \frac{1}{2} \langle \sigma_2 \rangle J_b \cos^2 \theta_2 - \frac{\langle \sigma_2 \rangle J_b}{4} \sin^2 \theta_2 \gamma(\mathbf{k}_{\parallel}) + J_s \langle \sigma_1 \rangle \cos^2 \theta_1 + J_b \langle \sigma_3 \rangle \cos^2 \theta_3,$$

$$V_n = 2\Omega_n \sin \theta_n + \frac{1}{2} \langle \sigma_n \rangle J_b \cos^2 \theta_n - \frac{\langle \sigma_n \rangle J_n}{4} \sin^2 \theta_n \gamma(\mathbf{k}_{\parallel}) + J_{n-1}\sigma_{n-1} \cos^2 \theta_{n-1}$$
$$+ J_{n+1}\sigma_{n+1} \cos^2 \theta_{n+1},$$

$$V_N = 2\Omega_s \sin \theta_N + \frac{1}{2} \langle \sigma_N \rangle J_s \cos^2 \theta_N - \frac{\langle \sigma_N \rangle J_s}{4} \sin^2 \theta_N \gamma(\mathbf{k}_{\parallel}) + J_b\sigma_{N-1} \cos^2 \theta_{N-1},$$

$$\bar{V}(\mathbf{q}_{\parallel}, \mathbf{k}_{\parallel} - \mathbf{q}_{\parallel}) = J(\mathbf{q}_{\parallel}) \cos^2 \theta - \frac{1}{2} J(\mathbf{k}_{\parallel} - \mathbf{q}_{\parallel}) \sin^2 \theta,$$

$$\gamma(\mathbf{k}_{\parallel}) = \frac{1}{2}(\cos(k_x a) + \cos(k_y a)).$$

The notations $J_1 \equiv J_N = J_s$, $J_n = J_b$ and $\Omega_1 = \Omega_N = \Omega_s$, $\Omega_n = \Omega_b$ for $n = 2, 3, 4, ..., N - 1$), $J_0 = J_{N+1} = 0$. The quantity $\langle \sigma \rangle (T)$ is the relative polarization in the direction of the mean field.

Prefactors for non-collinear magnetic structures

This section refers to the calculation of the renormalized prefactors in case of spiral magnetic structures. Here the most general case is assumed. The quantization axis is set by γ_x, γ_y and γ_z. The corresponding transformation of the spin operators for spin-$\frac{1}{2}$ particles with $\sigma_f^a = \frac{1}{2} - a_f^\dagger a_f$ reads:

$$(S_f)^\alpha = \gamma_f^\alpha \sigma_f + A_f^\alpha b_f + (A_f^*)^\alpha b_f^\dagger \tag{A.4}$$

In case of another subsystem b the transformation reads:

$$(S_f)^\alpha = \gamma_f^\alpha \sigma_f + B_f^\alpha b_f + (B_f^*)^\alpha b_f^\dagger \tag{A.5}$$

The quantization axis is chosen is chosen as:

$$\gamma_l^z = \text{const.} \tag{A.6a}$$

$$\gamma_l^x = \rho \cos(\varphi_l + \delta) = \rho[\cos\delta \cos\varphi_l - \sin\delta \sin\varphi_l] \tag{A.6b}$$

$$\gamma_l^y = \rho \sin(\varphi_l + \delta) = \rho[\cos\delta \sin\varphi_l + \sin\delta \cos\varphi_l] \tag{A.6c}$$

$$\gamma_l'^z = \text{const.} \tag{A.6d}$$

$$\gamma_l'^x = \rho' \cos(\varphi_l) \tag{A.6e}$$

$$\gamma_l'^y = \rho' \sin(\varphi_l) \tag{A.6f}$$

The length of the quantization axis in the xy plane is defined as $\sqrt{1 - (\gamma^z)^2}$. The prefactors A_f^α and B_f^α (with $\delta = 0$) are defined as:

$$A_f^x = -\frac{1}{2}\{\cos\delta[\gamma^z \cos\varphi_f + \mathrm{i}\sin\varphi_f] - \sin\delta[\gamma^z \sin\varphi_f - \mathrm{i}\cos\varphi_f]\} \tag{A.7a}$$

$$A_f^y = -\frac{1}{2}\{\cos\delta[\gamma^z \sin\varphi_f - \mathrm{i}\cos\varphi_f] + \sin\delta[\gamma^z \cos\varphi_f + \mathrm{i}\sin\varphi_f]\} \tag{A.7b}$$

$$A_f^z = \frac{\rho}{2} \tag{A.7c}$$

$$B_f^x = -\frac{1}{2}\{\gamma'^z \cos\varphi_f + \mathrm{i}\sin\varphi_f\} \tag{A.7d}$$

$$B_f^y = -\frac{1}{2}\{\gamma'^z \sin\varphi_f - \mathrm{i}\cos\varphi_f]\} \tag{A.7e}$$

$$B_f^z = \frac{\rho'}{2} \tag{A.7f}$$

The phase shift between the two sublattices is δ. The scalar product of these $\boldsymbol{\gamma}$, $\mathbf{A}$ and

B factors at different sites is carried out in the next step.

$$(\gamma_l^\alpha \gamma_g^\alpha) = \gamma^z \gamma^z + \rho\rho'[\cos\delta\cos(\varphi_l - \varphi_g) - \sin\delta\sin(\varphi_l - \varphi_g)] \tag{A.8}$$

$$\begin{aligned}(A_l^\alpha B_g^\alpha) = \frac{1}{4}\{&(\gamma^z\gamma^z - 1)[\cos\delta\cos(\varphi_l - \varphi_g) - \sin\delta\sin(\varphi_l - \varphi_g)]\\ &- \mathrm{i}(\gamma^z - \gamma^z)[\sin\delta\cos(\varphi_l - \varphi_g) + \cos\delta\sin(\varphi_l - \varphi_g)] + \rho\rho'\}\end{aligned} \tag{A.9}$$

$$\begin{aligned}((A_l^*)^\alpha (B_g^*)^\alpha) = \frac{1}{4}\{&(\gamma^z\gamma^z - 1)[\cos\delta\cos(\varphi_l - \varphi_g) - \sin\delta\sin(\varphi_l - \varphi_g)]\\ &+ \mathrm{i}(\gamma^z - \gamma^z)[\sin\delta\cos(\varphi_l - \varphi_g) + \cos\delta\sin(\varphi_l - \varphi_g)] + \rho\rho'\}\end{aligned} \tag{A.10}$$

$$\begin{aligned}(A_l^\alpha (B_g^*)^\alpha) = \frac{1}{4}\{&(\gamma^z\gamma^z + 1)[\cos\delta\cos(\varphi_l - \varphi_g) - \sin\delta\sin(\varphi_l - \varphi_g)]\\ &+ \mathrm{i}(\gamma^z + \gamma^z)[\sin\delta\cos(\varphi_l - \varphi_g) + \cos\delta\sin(\varphi_l - \varphi_g)] + \rho\rho'\}\end{aligned} \tag{A.11}$$

$$\begin{aligned}(B_l^\alpha (A_g^*)^\alpha) = \frac{1}{4}\{&(\gamma^z\gamma^z + 1)[\cos\delta\cos(\varphi_l - \varphi_g) + \sin\delta\sin(\varphi_l - \varphi_g)]\\ &- \mathrm{i}(\gamma^z + \gamma^z)[\sin\delta\cos(\varphi_l - \varphi_g) - \cos\delta\sin(\varphi_l - \varphi_g)] + \rho\rho'\}\end{aligned} \tag{A.12}$$

$$\begin{aligned}\gamma_l^\alpha B_g^\alpha = -\frac{\rho}{2}\Big\{&\cos\delta[\gamma^z\cos(\varphi_l - \varphi_g) - \mathrm{i}\sin(\varphi_l - \varphi_g)]\\ &- \sin\delta[\gamma^z\sin(\varphi_l - \varphi_g) + \mathrm{i}\cos(\varphi_l - \varphi_g)]\Big\} + \gamma^z\frac{\rho'}{2}\end{aligned} \tag{A.13}$$

$$\begin{aligned}\gamma_l^\alpha (B_g^*)^\alpha = -\frac{\rho}{2}\Big\{&\cos\delta[\gamma^z\cos(\varphi_l - \varphi_g) + \mathrm{i}\sin(\varphi_l - \varphi_g)]\\ &- \sin\delta[\gamma^z\sin(\varphi_l - \varphi_g) - \mathrm{i}\cos(\varphi_l - \varphi_g)]\Big\} + \gamma^z\frac{\rho'}{2}\end{aligned} \tag{A.14}$$

$$\begin{aligned}\gamma_l^\alpha A_g^\alpha = -\frac{\rho'}{2}\Big\{&\cos\delta[\gamma^z\cos(\varphi_l - \varphi_g) - \mathrm{i}\sin(\varphi_l - \varphi_g)]\\ &+ \sin\delta[\gamma^z\sin(\varphi_l - \varphi_g) + \mathrm{i}\cos(\varphi_l - \varphi_g)]\Big\} + \gamma^z\frac{\rho}{2}\end{aligned} \tag{A.15}$$

$$\begin{aligned}\gamma_l^\alpha (A_g^*)^\alpha = -\frac{\rho'}{2}\Big\{&\cos\delta[\gamma^z\cos(\varphi_l - \varphi_g) + \mathrm{i}\sin(\varphi_l - \varphi_g)]\\ &+ \sin\delta[\gamma^z\sin(\varphi_l - \varphi_g) - \mathrm{i}\cos(\varphi_l - \varphi_g)]\Big\} + \gamma^z\frac{\rho}{2}\end{aligned} \tag{A.16}$$

The vector product $\varepsilon^{\alpha\mu\nu}\gamma_l^\mu\gamma_g^\nu$ reads:

z-component

$$\varepsilon^{z\mu\nu}\gamma_l^\mu\gamma_g^\nu = \varepsilon^{z\mu\nu}\gamma^\mu\gamma^\nu(l-g) \tag{A.17a}$$

$$= -\rho\rho'[\sin\delta\cos(\varphi_l - \varphi_g) + \cos\delta\sin(\varphi_l - \varphi_g)] \tag{A.17b}$$

x-component

$$\varepsilon^{x\mu\nu}\gamma_l^\mu\gamma_g^\nu = \rho\gamma^z[\cos\delta\sin\varphi_l + \sin\delta\cos\varphi_l] - \rho'\gamma^z\sin\varphi_g \tag{A.17c}$$

y-component

$$\varepsilon^{y\mu\nu}\gamma_l^\mu\gamma_g^\nu = -\rho\gamma^z[\cos\delta\cos\varphi_l - \sin\delta\sin\varphi_l] + \rho'\gamma^z\cos\varphi_g \tag{A.17d}$$

The vector product $\varepsilon^{\alpha\mu\nu}A_l^\mu B_g^\nu$ reads:

z-component
$$\varepsilon^{z\mu\nu}A_l^\mu B_g^\nu = \varepsilon^{z\mu\nu}A^\mu B^\nu(l-g)$$
$$= \frac{1}{4}\{(1-\gamma^z\gamma^z)[\sin\delta\cos(\varphi_l-\varphi_g)+\cos\delta\sin(\varphi_l-\varphi_g)]$$
$$- \mathrm{i}(\gamma^z-\gamma^z)[\cos\delta\cos(\varphi_l-\varphi_g)-\sin\delta\sin(\varphi_l-\varphi_g)]\}$$
$$\text{(A.18)}$$

x-component
$$\varepsilon^{x\mu\nu}A_l^\mu B_g^\nu = \frac{1}{4}\{-\gamma^z\rho[\cos\delta\sin\varphi_l+\sin\delta\cos\varphi_l]+\gamma^z\rho\sin\varphi_g$$
$$+ \mathrm{i}[\rho(\cos\delta\cos\varphi_l-\sin\delta\sin\varphi_l)-\rho\cos\varphi_g]\}$$
$$\text{(A.19)}$$

y-component
$$\varepsilon^{y\mu\nu}A_l^\mu B_g^\nu = \frac{1}{4}\{\gamma^z\rho[\cos\delta\cos\varphi_l-\sin\delta\sin\varphi_l]-\gamma^z\rho\cos\varphi_g$$
$$+ \mathrm{i}[\rho(\cos\delta\sin\varphi_l+\sin\delta\cos\varphi_l)-\rho\sin\varphi_g]\}$$
$$\text{(A.20)}$$

The vector product $\varepsilon^{\alpha\mu\nu}A_l^\mu(B_g^*)^\nu$ reads:

z-component
$$\varepsilon^{z\mu\nu}A_l^\mu(B_g^*)^\nu = \varepsilon^{z\mu\nu}A^\mu(B^*)^\nu(l-g) =$$
$$\frac{1}{4}\{-(1+\gamma^z\gamma^z)[\sin\delta\cos(\varphi_l-\varphi_g)+\cos\delta\sin(\varphi_l-\varphi_g)]$$
$$+ \mathrm{i}(\gamma^z+\gamma^z)[\cos\delta\cos(\varphi_l-\varphi_g)-\sin\delta\sin(\varphi_l-\varphi_g)]\}$$
$$\text{(A.21)}$$

x-component
$$\varepsilon^{x\mu\nu}A_l^\mu(B_g^*)^\nu = -\frac{\rho}{4}\{\gamma^z[\cos\delta\sin\varphi_l+\sin\delta\cos\varphi_l]-\mathrm{i}[\cos\delta\cos\varphi_l-\sin\delta\sin\varphi_l]$$
$$+ \frac{\rho}{4}(\gamma^z\sin\varphi_g+\mathrm{i}\cos\varphi_g)\}$$
$$\text{(A.22)}$$

y-component
$$\varepsilon^{y\mu\nu}A_l^\mu(B_g^*)^\nu = \frac{\rho}{4}\{\gamma^z[\cos\delta\cos\varphi_l-\sin\delta\sin\varphi_l]+\mathrm{i}[\cos\delta\sin\varphi_l+\sin\delta\cos\varphi_l]$$
$$- \frac{\rho}{4}(\gamma^z\cos\varphi_g-\mathrm{i}\sin\varphi_g)\}$$
$$\text{(A.23)}$$

The vector product $\varepsilon^{\alpha\mu\nu}B_l^\mu(A_g^*)^\nu$ reads:

z-component
$$\varepsilon^{z\mu\nu}B_l^\mu(A_g^*)^\nu = \varepsilon^{z\mu\nu}B^\mu(A^*)^\nu(l-g) =$$
$$\frac{1}{4}\{(1+\gamma^z\gamma^z)[\sin\delta\cos(\varphi_l-\varphi_g)-\cos\delta\sin(\varphi_l-\varphi_g)]$$
$$+ \mathrm{i}(\gamma^z+\gamma^z)[\cos\delta\cos(\varphi_l-\varphi_g)+\sin\delta\sin(\varphi_l-\varphi_g)]\}$$
$$\text{(A.24)}$$

The vector product $\varepsilon^{\alpha\mu\nu}\gamma_l^\mu B_g^\nu$ reads:

z-component

$$\varepsilon^{z\mu\nu}\gamma_l^\mu B_g^\nu = \frac{\rho}{2}\Big\{\cos\delta[\gamma^z\sin(\varphi_l - \varphi_g) + \mathrm{i}\cos(\varphi_l - \varphi_g)] \tag{A.25}$$
$$+ \sin\delta[\gamma^z\cos(\varphi_l - \varphi_g) - \mathrm{i}\sin(\varphi_l - \varphi_g)]\Big\}$$

The vector product $\varepsilon^{\alpha\mu\nu}\gamma_l^\mu (B_g^*)^\nu$ reads:

z-component

$$\varepsilon^{z\mu\nu}\gamma_l^\mu (B_g^*)^\nu = \frac{\rho}{2}\Big\{\cos\delta[\gamma^z\sin(\varphi_l - \varphi_g) - \mathrm{i}\cos(\varphi_l - \varphi_g)] \tag{A.26}$$
$$+ \sin\delta[\gamma^z\cos(\varphi_l - \varphi_g) + \mathrm{i}\sin(\varphi_l - \varphi_g)]\Big\}$$

The vector product $\varepsilon^{\alpha\mu\nu}\gamma_l^\mu A_g^\nu$ reads:

z-component

$$\varepsilon^{z\mu\nu}\gamma_l^\mu A_g^\nu = \frac{\rho}{2}\Big\{\cos\delta[\gamma^z\sin(\varphi_l - \varphi_g) + \mathrm{i}\cos(\varphi_l - \varphi_g)] \tag{A.27}$$
$$- \sin\delta[\gamma^z\cos(\varphi_l - \varphi_g) - \mathrm{i}\sin(\varphi_l - \varphi_g)]\Big\}$$

The vector product $\varepsilon^{\alpha\mu\nu}\gamma_l^\mu (A_g^*)^\nu$ reads:

z-component

$$\varepsilon^{z\mu\nu}\gamma_l^\mu (A_g^*)^\nu = \frac{\rho}{2}\Big\{\cos\delta[\gamma^z\sin(\varphi_l - \varphi_g) - \mathrm{i}\cos(\varphi_l - \varphi_g)] \tag{A.28}$$
$$- \sin\delta[\gamma^z\cos(\varphi_l - \varphi_g) + \mathrm{i}\sin(\varphi_l - \varphi_g)]\Big\}$$

With the help of the former expressions, the needed prefactors X_{lj}, S_{lj}, R_{lj} and Z_{lj} can be calculated. The corresponding Fourier transformation reads:

$$X^0(q, Q) = J_q\gamma^z\gamma^z + \frac{\rho\rho}{2}[e^{\mathrm{i}\delta}(J(q - Q) + \mathrm{i}D^z(q - Q)) + e^{-\mathrm{i}\delta}(J(q + Q) - \mathrm{i}D^z(q + Q))] \tag{A.29}$$

Repeating the same calculations as before one gets:

$$S^0(q,Q) = \frac{1}{4}J_q\rho\slashed{\rho} + \frac{1}{8}\{(\gamma^z - 1)(\slashed{\gamma}^z - 1)[J(q+Q) - iD^z(q+Q))]e^{-i\delta}$$
$$+ (\gamma^z + 1)(\slashed{\gamma}^z + 1)[J(q-Q) + iD^z(q-Q))]e^{i\delta}\} \tag{A.30}$$

$$T(q,Q) = \frac{1}{4}J_q\rho\slashed{\rho} + \frac{1}{8}\{(\gamma^z - 1)(\slashed{\gamma}^z - 1)[J(q+Q) - iD^z(q+Q))]e^{+i\delta}$$
$$+ (\gamma^z + 1)(\slashed{\gamma}^z + 1)[J(q-Q) + iD^z(q-Q))]e^{-i\delta}\} \tag{A.31}$$

$$R^0(q,Q) = \frac{1}{4}J_q\rho\slashed{\rho} + \frac{1}{8}\{(\gamma^z - 1)(\slashed{\gamma}^z + 1)[J(q+Q) - iD^z(q+Q))]e^{-i\delta}$$
$$+ (\gamma^z + 1)(\slashed{\gamma}^z - 1)[J(q-Q) + iD^z(q-Q))]e^{i\delta}\} \tag{A.32}$$

$$\tilde{R}^0(q,Q) = \frac{1}{4}J_q\rho\slashed{\rho} + \frac{1}{8}\{(\gamma^z - 1)(\slashed{\gamma}^z + 1)[J(q-Q) + iD^z(q-Q))]e^{+i\delta}$$
$$+ (\gamma^z + 1)(\slashed{\gamma}^z - 1)[J(q+Q) - iD^z(q+Q))]e^{-i\delta}\} \tag{A.33}$$

$$Z^0(q,Q) = \frac{\gamma^z\slashed{\rho}}{2}J_q - \frac{\rho}{4}\Big\{(\slashed{\gamma}^z - 1)e^{i\delta}[J(q-Q) + iD^z(q-Q)]$$
$$+ (\slashed{\gamma}^z + 1)e^{-i\delta}[J(q+Q) - iD^z(q+Q)]\Big\} \tag{A.34}$$

$$\tilde{Z}^0(q,Q) = \frac{\gamma^z\slashed{\rho}}{2}J_q - \frac{\rho}{4}\Big\{(\slashed{\gamma}^z + 1)e^{i\delta}[J(q-Q) + iD^z(q-Q)]$$
$$+ (\slashed{\gamma}^z - 1)e^{-i\delta}[J(q+Q) - iD^z(q+Q)]\Big\} \tag{A.35}$$

$$Y^0(q,Q) = \frac{\slashed{\gamma}^z\rho}{2}J_q - \frac{\slashed{\rho}}{4}\Big\{(\gamma^z - 1)e^{-i\delta}[J(q-Q) + iD^z(q-Q)]$$
$$+ (\gamma^z + 1)e^{+i\delta}[J(q+Q) - iD^z(q+Q)]\Big\} \tag{A.36}$$

$$\tilde{Y}^0(q,Q) = \frac{\slashed{\gamma}^z\rho}{2}J_q - \frac{\slashed{\rho}}{4}\Big\{(\gamma^z + 1)e^{-i\delta}[J(q-Q) + iD^z(q-Q)]$$
$$+ (\gamma^z - 1)e^{+i\delta}[J(q+Q) - iD^z(q+Q)]\Big\} \tag{A.37}$$

Danksagung

Abschließend möchte ich mich an dieser Stelle bei meinem Doktorvater *Herrn Prof. Dr. Steffen Trimper* und *Frau Prof. Dr. Julia M. Wesselinowa* für die wertvollen Hinweise und Gespräche während der Anfertigung dieser Dissertation und bei *Herrn Prof. Dr. Jamal Berekdar* für seine nützlichen und wichtigen Hinweise, bedanken. Weiterhin gilt mein Dank *Herrn Dipl.-Math. Marian Brandau* und *Herrn Dipl.-Phys. Thomas Bose* für die vielfach geführten Diskussionen in Bezug auf die Dissertation, für ein offenes Ohr in Hard- und Softwarefrage und und in Bezug auf T$_{\text{E}}$Xnische Belange. Nicht zu vergessen sind alle Freunde, die mich in dieser Zeit begleitet haben und immer ein offenes Ohr hatten. Desweiteren möchte ich mich natürlich bei meiner Frau *Julia* bedanken, die mir durch ihr Verständnis in allen Belangen und ihre konstruktiven Hinweise sehr geholfen hat.

Lebenslauf

———— Persönliche Daten

Name	Thomas Michael
Geburtsdatum	01.01.1980
Geburtsort	Merseburg
Nationalität	deutsch
Familienstand	verheiratet

———— Kontaktinformationen

Adresse	Weizenweg 10
	06132 Halle (Saale)
	Deutschland

———— Schulische und berufliche Ausbildung

1992–1998	**Gymnasium**, *Immanuel-Kant-Gymnasium*, Chemnitz, Deutschland.
1998–1999	**Zivildienst**, *DRK*, Chemnitz, Deutschland.
1999–2005	**Studium der Physik**, *Martin-Luther-Universität Halle-Wittenberg*, Halle (Saale), Deutschland.
2005	**Diplom in Physik**, Diplomarbeit: *Statistische Systeme mit Gedächtnis*.
2005-2010	**Doktorand**, *Martin-Luther-Universität Halle-Wittenberg*, Halle (Saale), Deutschland.
	Dissertationstitel: *Analytical description of ferroelectric nanostructures and bulk systems with non-collinear magnetic order*
2005-2010	**Mitglied der International Max-Planck Research School for Science and Technology of Nanostructures (IMPRS)**, Halle (Saale), Deutschland.

Halle, den 09. Juli 2010

Thomas Michael